

ΠΑΝΕΠΙΣΤΗΜΙΟ ΚΡΗΤΗΣ
ΣΧΟΛΗ ΘΕΤΙΚΩΝ ΚΑΙ ΤΕΧΝΟΛΟΓΙΚΩΝ ΕΠΙΣΤΗΜΩΝ
ΤΜΗΜΑ ΕΠΙΣΤΗΜΗΣ ΚΑΙ ΤΕΧΝΟΛΟΓΙΑΣ ΥΛΙΚΩΝ

Διδακτορική Διατριβή

ΥΔΡΟΓΟΝΟ ΣΕ ΝΑΝΟΔΟΜΗΜΕΝΑ ΥΛΙΚΑ ΜΕ ΒΑΣΗ ΤΟΝ
ΑΝΘΡΑΚΑ

ΥΠΟΛΟΓΙΣΤΙΚΗ ΚΑΙ ΘΕΩΡΗΤΙΚΗ ΜΕΛΕΤΗ

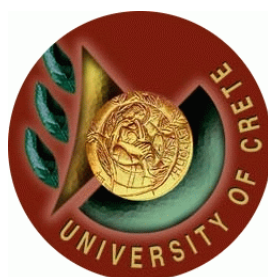
Μανιαδάκη Ε. Αριστέα

Ηράκλειο
2015

Aristea E. Maniadaki

Hydrogen in Carbon - based Nanostructured Materials
A Theoretical and Computational Study

A Doctoral Dissertation



Department of Materials Science and Technology,
University of Crete,
Heraklion, Greece
October 2015

Hydrogen in Carbon-based Nanostructured Materials

A Theoretical and Computational Study

Thesis author Aristeia E. Maniadaki

Thesis supervisor George Kopidakis

Thesis committee G. Kopidakis
 A. Andriotis
 I. Remediakis
 V. Harmandaris
 M. Kafesaki
 G. Kioseoglou
 N. Pelekanos



Co-financed by Greece and the European Union

Department of Materials Science and Technology,
University of Crete,
Heraklion, Greece

2015



ΠΑΝΕΠΙΣΤΗΜΙΟ ΚΡΗΤΗΣ
ΣΧΟΛΗ ΘΕΤΙΚΩΝ ΚΑΙ ΤΕΧΝΟΛΟΓΙΚΩΝ ΕΠΙΣΤΗΜΩΝ
ΤΜΗΜΑ ΕΠΙΣΤΗΜΗΣ ΚΑΙ ΤΕΧΝΟΛΟΓΙΑΣ ΥΛΙΚΩΝ

ΠΡΑΚΤΙΚΟ ΔΗΜΟΣΙΑΣ ΠΑΡΟΥΣΙΑΣΗΣ ΚΑΙ ΕΞΕΤΑΣΗΣ
ΤΗΣ ΔΙΔΑΚΤΟΡΙΚΗΣ ΔΙΑΤΡΙΒΗΣ ΤΗΣ
κας. Μανιαδάκη Αριστέας
ΥΠΟΨΗΦΙΑΣ ΔΙΔΑΚΤΟΡΟΣ ΤΟΥ ΤΜΗΜΑΤΟΣ ΕΠΙΣΤΗΜΗΣ ΚΑΙ
ΤΕΧΝΟΛΟΓΙΑΣ ΥΛΙΚΩΝ

Η Επταμελής Επιτροπή της Διδακτορικής Διατριβής της *κας. Μανιαδάκη Αριστέας* η οποία ορίστηκε στην 67η Γ.Σ.Ε.Σ. στις 25/09/2015, εκλήθη την Παρασκευή 30 Οκτωβρίου 2015 να εξετάσει την σύμφωνα με το Νόμο υποστήριξη της διατριβής της υποψηφίου με τίτλο:

«Υδρογόνο σε Νανοδομημένα Υλικά με Βάση τον Άνθρακα –
Θεωρητική και Υπολογιστική Μελέτη»

Τα παρόντα μέλη της επταμελούς Επιτροπής εκφράζουν ομόφωνα την πλήρη ικανοποίησή τους για την υψηλή ποιότητα του περιεχομένου και της υποστήριξης της διατριβής.

Τα ερευνητικά αποτελέσματα της εργασίας της *κας. Μανιαδάκη Αριστέας* είναι σημαντικά, πρωτότυπα και διευρύνουν το πεδίο της έρευνας στην Επιστήμη και Τεχνολογία Υλικών.

Ως εκ τούτου η Εξεταστική Επιτροπή προτείνει ομόφωνα την απονομή του Διδακτορικού Διπλώματος στην *κα. Μανιαδάκη Αριστέα*.

Τα μέλη της επταμελούς επιτροπής για την αξιολόγηση της Διδακτορικής Διατριβής της *κας. Μανιαδάκη Αριστέας*.

Η Επταμελής Επιτροπή:

Κοπιδάκης Γεώργιος

(Επιβλέπων)

Αναπληρωτής καθηγητής, Τμήματος Επιστήμης και Τεχνολογίας Υλικών, Παν/μίου Κρήτης

Ανδριώτης Αντώνιος

Ομότιμος ερευνητής Α', Ινστιτούτου Ηλεκτρονικής Δομής και Λείζερ, Ίδρυμα Τεχνολογίας και Έρευνας, Ηράκλειο

Ρεμεδιάκης Ιωάννης

Μόνιμος επίκουρος καθηγητής, Τμήματος Επιστήμης και Τεχνολογίας Υλικών, Παν/μίου Κρήτης

Καφεσάκη Μαρία

Αναπληρώτρια καθηγήτρια, Τμήματος Επιστήμης και Τεχνολογίας Υλικών, Παν/μίου Κρήτης

Κιοσέογλου Γεώργιος

Αναπληρωτής καθηγητής, Τμήματος Επιστήμης και Τεχνολογίας Υλικών, Παν/μίου Κρήτης

Πελεκάνος Νικόλαος

Καθηγητής, Τμήματος Επιστήμης και Τεχνολογίας Υλικών, Παν/μίου Κρήτης

Χαρμανδάρης Ευάγγελος

Μόνιμος επίκουρος καθηγητής, Τμήματος Μαθηματικών και Εφαρμοσμένων Μαθηματικών, Παν/μίου Κρήτης

Abstract

Carbon-based nanostructured materials (CNMs) exhibit fundamental interest and are promising candidates for numerous applications in hydrogen production, storage, and use in clean energy applications. Extensive research on carbon nanotubes, fullerenes and graphene has dramatically improved our knowledge about these materials. However, a wealth of other CNMs provide opportunities for technological advances while also presenting scientific challenges. There is strong evidence that complex nanostructures, nanoporous and disordered carbon phases, with or without other chemical substitutions, adsorb hydrogen more efficiently. Difficulties in controlling synthesis conditions, in characterization, and the complexity of these materials make their detailed theoretical study imperative.

Among these CNMs, the mixed phase of amorphous carbon (a-C) and diamond nanocrystals (n-D) has been less studied and characterized, with many of its properties remaining unexplored. We perform atomistic simulations with empirical potentials in order to create several a-C-n-D samples with different n-D sizes and a-C densities, and samples of ultra-nanocrystalline diamond (UNCD) with various grain sizes. We analyze the structure, stability, and mechanical properties of these nanocomposite materials and our results compare well with experiment and previous simulations. Furthermore, we study their dynamical properties to find that some pronounced features of their vibrational spectra may be observed in experiments. Finally, the effects of hydrogen in the structural and mechanical properties of these materials are investigated.

We also investigate CNMs for the adsorption and desorption of hydrogen. Recent studies have shown that transition metal dichalcogenides (TMDs) MX_2 ($M = \text{Mo}, \text{W}$; $X = \text{S}, \text{Se}, \text{Te}$) are rising candidates in the replacement of Pt as catalysts in the water splitting process. We focus on the hydrogen evolution reaction (HER) part of this process and on how Hydrogen (H) interacts with the TMDs. Specifically, we perform Density Functional Theory (DFT) calculations for MoS_2 as free standing nanostructures or positioned on a graphene substrate. These MoS_2 nanostructures as well as MoS_2 /Graphene hybrid systems are investigated for their stability. Our calculations of the adsorption of H on the MoS_2 /Graphene hybrid systems indicate that the effect of graphene in the adsorption process of H on MoS_2 nanostructures is quite significant.

Strain in the hybrid MoS_2 /Graphene systems, inherent due to lattice mismatch, plays an important role in their properties. This leads into a theoretical investigation of the structural, electronic and dielectric properties of single-layer TMDs under various types of strain. We find that electronic band gaps decrease while dielectric constants increase for heavier chalcogens. The direct gaps of equilibrium structures often become indirect under certain types of strain. The effects of strain and of broken symmetry on the band structure are discussed. The DFT results concerning the effect of strain in the dielectric properties are theoretically explained using only structural parameters and equilibrium dielectric constants.

Abstract (Ελληνικά)

Τα νανοδομημένα υλικά με βάση τον άνθρακα (Carbon-based Nanostructured Materials - CNMs) παρουσιάζουν θεμελιώδες ενδιαφέρον και είναι καλοί υποψήφιοι για πολυάριθμες εφαρμογές στην παραγωγή, αποθήκευση και χρήση του υδρογόνου σε εφαρμογές καθαρής ενέργειας. Εκτεταμένες έρευνες στους νανοσωλήνες άνθρακα, στα φουλερένια και στο γραφένιο έχουν βελτιώσει δραματικά τις γνώσεις μας σχετικά με τα υλικά αυτά. Ωστόσο, μια πληθώρα από άλλα CNMs προσφέρουν ευκαιρίες για τεχνολογική πρόοδο ενώ ταυτόχρονα παρουσιάζουν επιστημονικές προκλήσεις. Υπάρχουν σημαντικές ενδείξεις ότι πολύπλοκες νανοδομές, νανοπορώδεις και άτακτες μορφές άνθρακα, με ή χωρίς άλλες χημικές υποκαταστάσεις, προσροφούν υδρογόνο πιο αποτελεσματικά. Δυσκολίες στον έλεγχο των συνθηκών σύνθεσης, στον χαρακτηρισμό, καθώς και η πολυπλοκότητα αυτών των υλικών, καθιστούν αναγκαία την λεπτομερή θεωρητική μελέτη τους.

Μεταξύ αυτών των CNMs, η μεικτή φάση από άμορφο άνθρακα (a-C) με νανοκρυστάλλους διαμαντιού (n-D) είναι λιγότερη μελετημένη και χαρακτηρισμένη, με πολλές από τις ιδιότητές της να παραμένουν αδιερεύνητες. Πραγματοποιούμε ατομιστικές προσομοιώσεις με εμπειρικά δυναμικά προκειμένου να δημιουργήσουμε αρκετά δείγματα a-C - n-D με διαφορετικά μεγέθη n-D και διαφορετικές πυκνότητες a-C, καθώς επίσης και δείγματα υπερ-νανοκρυσταλλικού διαμαντιού (UNCD) με διάφορα μεγέθη κόκκων. Αναλύουμε τη δομή, τη σταθερότητα και τις μηχανικές ιδιότητες των νανοσύνθετων αυτών υλικών και τα αποτελέσματά μας συγκρίνονται καλά με το πείραμα και προηγούμενες προσομοιώσεις. Επιπλέον, μελετάμε τις δυναμικές τους ιδιότητες και διαπιστώνουμε ότι κάποια έντονα χαρακτηριστικά των δονητικών τους φασμάτων μπορούν να παρατηρηθούν σε πειράματα. Τέλος, διερευνάται η επίδραση του υδρογόνου στις δομικές και μηχανικές ιδιότητες των υλικών αυτών.

Διερευνούμε επίσης CNMs για προσρόφηση και εκρόφηση υδρογόνου. Πρόσφατες μελέτες έχουν δείξει ότι τα διχαλκογενίδια μεταβατικών μετάλλων (Transition Metal Dichalcogenides - TMDs) MX_2 ($\text{M} = \text{Mo}, \text{W}$; $\text{X} = \text{S}, \text{Se}, \text{Te}$) είναι ανερχόμενοι υποψήφιοι για την αντικατάσταση του Pt ως καταλύτες στη διαδικασία διάσπασης του νερού. Εστιάζουμε στο μέρος αυτής της διαδικασίας που αφορά στην αντίδραση έκλυσης υδρογόνου (Hydrogen Evolution Reaction - HER) και στο πώς το υδρογόνο (H) αλληλεπιδρά με τα TMDs. Συγκεκριμένα, εκτελούμε υπολογισμούς θεωρίας συναρτησιακού πυκνότητας (Density Functional Theory - DFT) για ελεύθερες νανοδομές MoS_2 ή τοποθετημένες σε υπόστρωμα γραφενίου. Αυτές οι νανοδομές MoS_2 καθώς και τα υβριδικά συστήματα MoS_2 /γραφενίου διερευνώνται για τη σταθερότητά τους. Οι υπολογισμοί μας σχετικά με τη προσρόφηση του H στα υβριδικά συστήματα MoS_2 /γραφενίου δείχνουν ότι η επίδραση του γραφενίου στη διαδικασία της προσρόφησης H σε νανοδομές MoS_2 είναι αρκετά σημαντική.

Η μηχανική παραμόρφωση (τάση) των υβριδικών συστημάτων MoS_2 /γραφενίου, η οποία είναι εγγενής λόγω της πλεγματικής αναντιστοιχίας, παίζει σημαντικό ρόλο στις ιδιότητές τους. Αυτό οδηγεί σε θεωρητική διερεύνηση των δομικών, ηλεκτρονικών και διηλεκτρικών ιδιοτήτων των μονοστρωματικών TMDs υπό διάφορα είδη παραμόρφωσης. Βρίσκουμε ότι τα ηλεκτρονικά ενεργειακά χάσματα μειώνονται ενώ η διηλεκτρική σταθερά αυξάνεται για μεγαλύτερα χαλκογενή. Τα άμεσα χάσματα των

δομών ισορροπίας συχνά μετατρέπονται σε έμμεσα υπό την επίδραση κάποιων ειδών παραμόρφωσης. Αναλύονται επίσης οι επιδράσεις της παραμόρφωσης και η απώλεια συμμετρίας στην δομή των ενεργειακών ζωνών. Τα αποτελέσματα της DFT σχετικά με την επίδραση της παραμόρφωσης στις διηλεκτρικές ιδιότητες εξηγούνται θεωρητικά χρησιμοποιώντας μόνο δομικές παραμέτρους και τη διηλεκτρική σταθερά ισορροπίας.

Acknowledgments

First and foremost, I would like to express my gratitude to my supervisor, Prof. G. Kopidakis, for providing me with valuable opportunities and resources throughout this project. His scientific expertise and patience to my just-for-a-minute questions that turned into long discussions were catalytic in the realization of this work.

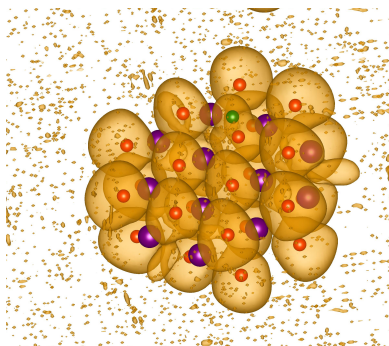
I would also like to express my acknowledgments to Prof. A. Andriotis and Prof. I. Remediakis for their key input and advice during our collaboration and to Prof. G. Kioseoglou for providing his experimental point-of-view in many aspects of my work.

I would also like to thank my previous and current fellow group members and colleagues, particularly my office-mate G. Vantarakis, who is responsible for my introduction into the \LaTeX world and whose insight and company is always appreciated.

All the simulations were performed using computational resources of the MST - Computational Theory Group. Big thanks are also due to D. Counalakis, for his patience with questions and requests, any time and any day.

Special thanks are owned to my sisters, brother and friends whose constant presence and support didn't let me get too absorbed in the scientific world, especially my friend Cos for his constant encouragement, advice and infinite "walking discussions" during this eventful journey.

The last and biggest thanks go to my parents whose love and patience during this journey, that cannot be limited to only the last few years, have been supporting and inspiring me.



Contents

| | |
|--|-----------|
| Thesis Committee | v |
| Thesis abstract | ix |
| Thesis Abstract (Ελληνικά) | xi |
| Acknowledgments | xiii |
| 1 Introduction | 1 |
| 2 Methodology | 5 |
| 2.1 Molecular Dynamics (MD) | 6 |
| 2.1.1 Tersoff Potential | 8 |
| 2.1.2 Brenner Potential | 10 |
| 2.2 Density Functional Theory | 11 |
| 3 Vibrational Properties of Carbon Nanostructures | 15 |
| 3.1 Introduction | 15 |
| 3.2 Results and Discussion | 18 |
| 3.2.1 Crystalline Carbon | 18 |
| 3.2.2 Amorphous Carbon (a-C) | 22 |
| 3.2.3 Free Spherical Nanostructures(n-D) | 27 |
| 3.2.4 Spherical Nanocrystals Embedded in Amorphous Carbon (n-D - a-C) | 30 |
| 3.2.5 Ultra-Nanocrystalline Diamond (UNCD) | 38 |
| 3.2.6 H on 3D Carbon nanostructures | 41 |

CONTENTS

| | | |
|----------|--|-----------|
| 3.3 | Conclusions | 43 |
| 4 | Hydrogen Evolution edge-site activity of MoS₂ and hybrid MoS₂/Graphene structures | 45 |
| 4.1 | Introduction | 45 |
| 4.2 | Methodology | 48 |
| 4.3 | Results and Discussion | 48 |
| 4.3.1 | Free Standing MoS ₂ nanostructures | 48 |
| 4.3.2 | MoS ₂ on Graphene | 50 |
| 4.3.3 | H with MoS ₂ | 56 |
| 4.3.4 | H - MoS ₂ Graphene | 58 |
| 4.4 | Conclusions | 61 |
| 5 | Electronic Properties Engineering of TMDs: strained monolayer | 63 |
| 5.1 | Introduction | 63 |
| 5.2 | Methodology | 69 |
| 5.3 | Results and Discussion | 70 |
| 5.3.1 | Strain definitions | 70 |
| 5.3.2 | Structural details of strained structures | 71 |
| 5.3.3 | Effect of strain on electronic properties | 72 |
| 5.3.4 | Effect of Strain on dielectric constant | 77 |
| 5.4 | Conclusions | 81 |
| 6 | Summary and Perspective | 83 |
| A | Appendix A | 85 |
| | Bibliography | 101 |

Introduction

Excessive use of fossil fuels has resulted in their near depletion as well as the increase of international interest in new technologies of renewable energy sources. Apart from the political and economic problems this issue has caused, the long lasting environmental effects (air pollution and the consequential climate changes) are more important. In the last decades, the interest has been directed towards alternative energy sources. Despite the fact that there are several options (solar and wind power, hydro-power, geothermal energy, biomass, nuclear power), there are also many problems that first have to be dealt with, from the lack in efficiency to even possible dangers. A potential solution to some of these issues is given with hydrogen. Though it's difficult to find it isolated mainly because of its lightness, its abundance is ensured due to its existence in water, hydrocarbons biomass, etc.

At the moment, the vast amount of hydrogen used as a fuel is produced from hydrocarbons. Steam methane reforming ($\text{CH}_4 + \text{H}_2\text{O} \rightarrow 3\text{H}_2 + \text{CO}$) is a well developed technology. Although other options, such as:

- *Renewable Electrolysis*, where water is separated into hydrogen and oxygen gas,
- *Glasification*, where biomass ($\text{CH}_x\text{O}_y + (1 - y)\text{H}_2\text{O} \rightarrow \text{CO} + (1 + 0.5x - y)\text{H}_2$) or coal ($\text{C} + \text{H}_2\text{O} \rightarrow \text{CO} + \text{H}_2$) under heat and pressure produce H_2 ,
- *Biological*, where microbes extract H_2 from green algae, cyanobacteria or even biomass,
- *Nuclear High-Temperature Electrolysis*, which enhances the efficiency of water electrolysis, since the increase in the temperature of water requires less electricity, thus energy and

- *High-Temperature Thermochemical Water-Splitting*, which exploits the same principle by using solar concentrators for the temperature increase

are available, they are not yet in the level of mass use, mainly due to large cost and efficiency issues. Also, some of them cannot be considered "clean" since the byproducts of the H₂ production can be CO and CO₂.

The final goal is a production method that can be used on-site and help in avoiding any distribution problems from the current distribution methods, like pipeline networks, high pressure cylinders and cryogenic tanks.

Compressed gas, cryogenic liquid and solid materials comprise the three main approaches in hydrogen storage. Hydrogen storage in solid materials can be achieved through two options, chemisorption and physisorption. When chemisorption occurs, molecular hydrogen is split in hydrogen atoms and interacts with the surface of the adsorbate. Materials proposed, using chemisorption, for hydrogen storage are Metal Hydrides and Intermetallic materials. Temperature issues, slow kinetics and low capacity are some of the drawbacks of these materials. Whereas with physisorption molecular hydrogen is adsorbed beyond the surface (e.g. filling of micropores) and it offers fast kinetics and complete reversibility. Physisorption occurs in cryogenic isolated or high pressure tanks and porous materials (Metal Organic Frameworks (MOFs), microporous polymers, zeolites and carbon nanostructures). In these materials efficiency is the major issue.

All these materials need to be engineered to accommodate the standards that are set in order for hydrogen to be able to be considered a clean and usable energy source. These guidelines include gravimetric and volumetric standards, fast loading/unloading time, cyclability and of course safety. Despite this fact, carbon nanostructures, still attract scientific interest mainly for practical reasons, particularly their light weight. The need for materials that adsorb hydrogen in high quantities and desorb it with low cost in energy is still high and carbon nanostructures are investigated in that context.

The initial experimental reports [1] turned interest towards nanotubes, although the results were overestimated. Pure carbon nanotubes are not efficient in storage capability. Recent experiments show that other carbon nanostructured materials yield the same or even better results as solid structures for hydrogen storage.

The end of the line for hydrogen is its use in fuel cells (FCs). FCs combine oxygen and hydrogen and produce energy with water as a byproduct making hydrogen a completely environment-friendly fuel (by current standards). Molecular hydrogen goes through the negatively charged anode and splits into electrons and positively charged hydrogen atoms (protons). The flow of electrons from the anode to the cathode produces electricity. The positively charged protons go through an electrolyte

to the cathode and then recombine with oxygen (assisted by the electrons that have reached the cathode) and give water. Usually FCs are categorized by the type of electrolyte used. The FCs that replace internal combustion engines are usually Polymer Electrolyte Membrane (PEM) FCs. On each side of the electrolyte, in between of the electrodes, there is a catalyst which is usually a precious metal (Pt). This leads to an unwelcomed increase in the cost of a FC. For this reason, alternative materials to replace these catalyst are under investigation.

The objective of this work is the scientific assistance in some of the challenges mentioned before. The storage of compressed or liquid hydrogen demands a lot of energy and thus results in low efficiency. That is why we are going to focus on the characterization of carbon nanostructures having in mind the possible storage of hydrogen in carbon nanoporous materials. Disordered carbon nanostructures allow hydrogen to interact with the structure at room temperature and relatively low pressure which is why they are considered one of the best approaches. Additionally, they adsorb hydrogen more efficiently when they contain a small number of pores. High storage capability has been reported also in mechanically treated nanocrystalline graphite, carbon nanofibers [2], [3], [4], [5], or even, as some studies suggest more exotic forms, like nanocones. Imperfections and pores in a structure create areas of more effective hydrogen adsorption in the structures, even though the involved mechanisms are not yet clear. Particularly the addition of metal alloys seems to improve the adsorption ability and gives new perspective to the use of composite metal-organic materials[6].

Carbon nanostructures have also been proposed as catalysts for the adsorption and desorption of hydrogen in metal hydrides, giving new potentials to these materials for hydrogen storage[7]. However, experiments often give difficult to verify or even contradicting results since the fabrication and the characterization of amorphous and nanostructured carbon is not easy. The uniqueness of Carbon lies in its ability to exist in various forms. Also, different forms, either natural or composite (diamond, graphite, amorphous carbon, fullerenes, nanocrystalline diamond, graphene, etc.) display individual properties (density, hardness, conductivity, etc.). In the first part of this thesis a non invasive characterization method is introduced. The presence of hydrogen alters the structural, mechanical, electronic and optical properties. Although, this creates bigger challenges in the understanding of the mechanisms behind these changes, it also presents new technological advancements.

Another objective is the replacement of the FC's catalyst with a less expensive material. Transition Metal Dichalcogenides (TMDs) have already been proposed as possible alternatives as catalysts for the Hydrogen Evolution Reaction (HER). Here we investigate the effect of a graphene substrate on the TMDs, the effect they have in their stability and efficiency as catalysts.

The structure of the thesis is indicated below.

In the second chapter of this thesis, a brief summary of the different methodologies used is presented.

The third chapter covers the evaluation of the simulation method used, (by comparing our results with previous works), the introduction of the characterization method of carbon nanostructures and finally the introduction of Hydrogen in nanostructured Carbon.

In the fourth chapter the stability of the hybrid TMDs/Graphene system is estimated. For this we use various MoS₂ structures, from the 2D infinite sheet to the 1D nanoribbon and the 0D nanoflakes. After the stability of each structure is examined, Hydrogen is added in various edge sites. The stability and activity of each of these sites is also investigated.

Since the TMD structure in the hybrid system is submitted to strain as a result of the lattice mismatch, which seems to affect its properties, the fifth chapter is dedicated to the investigation of the TMDs under strain. The changes in the structural, electronic and dielectric properties of the structure under strain are examined.

In the final, sixth chapter, the general conclusions and the future aspirations of this work are presented.

Methodology

“If we were to name the most powerful assumption of all, which leads one on and on in an attempt to understand life, it is that all things are made of atoms, and that everything that living things do, can be understood in terms of the jiggings and wiggings of atoms”

Richard Feynman

Since the focus of this work is neither the implementation nor the manipulation of any computational method, a concise description of the main aspects of each method used will be attempted, with more details in each part of this thesis.

There are three basic categories of atomic-scale materials computer simulations. The first category are the Empirical/Classical Simulations which use parameters such as the bond length/angle between atoms, etc. derived either from other more accurate simulations (first principles) or from experimental data. These have the advantage of low computational cost, making them useful in large systems but a big disadvantage is that they cannot describe quantum phenomena. They use potentials like Lenard-Jones (pair potential), Morse, Tersoff (many body potential).

The next category are the semi-empirical potentials which include some quantum mechanical properties making them more accurate but with a higher cost in computational power. Such is the Tight-binding method.

The final category are the simulations from first principles (*ab-initio*) which are almost completely based on theoretical assumptions. This makes the method extremely expensive in computational power and thus used only for small systems. This is implemented through Density Functional Theory

Depending on the demands and the complexity of the system the right approach

is used.

2.1 Molecular Dynamics (MD)

In a molecular dynamics simulation the evolution of a system of atoms in time is observed through the equations of motion. Newton's law $F_i = m_i \cdot a_i$ is followed for each atom i , with m_i and $a_i = \frac{d^2 r_i}{dt^2}$ its mass and acceleration due to the interaction with the other atoms of the system. The basic numerical implementation of an MD simulation is shown in fig. 2.1

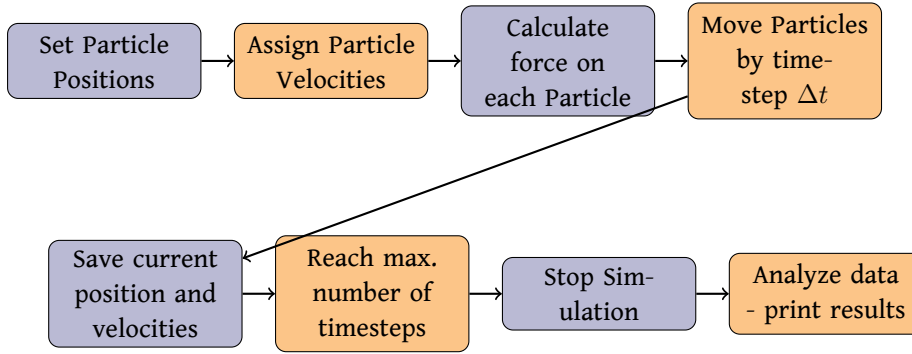


Fig. 2.1: Molecular Dynamics numerical implementation

For a system with N atoms in a unit cell of volume V the total energy is $E = K + U$ with K the kinetic and U the potential energy, as given from the equivalent formulas in eq.2.1.

$$K = \frac{1}{2} \cdot \sum_{i=1}^N m_i \cdot u_i^2, \quad U = U(r_1, \dots, r_N) \quad (2.1)$$

where r_i , m_i and u_i are the position, the mass and the velocity of the atom i .

The forces F_i are connected with the kinetic and potential energy through eq.2.2

$$F_i = m_i \cdot \frac{du_i}{dt}, \quad F_i = \frac{\partial U}{\partial r_i} \quad (2.2)$$

these equations create a coupled system of differential equations too complicated to solve. A simple solution is presented when time is discretized (n steps of Δt timestep). $r_i(t_0) \rightarrow r_i(t_0 + \Delta t) \rightarrow \dots \rightarrow r_i(t_0 + n \cdot \Delta t)$ with the use of a Taylor expansion (Verlet

central difference method)¹

$$\begin{aligned} r_i(t_0 + \Delta t) &= r_i(t_0) + u_i(t_0) \cdot \Delta t + \frac{1}{2} \cdot a_i(t_0) \cdot \Delta t^2 + \dots \\ +r_i(t_0 - \Delta t) &= r_i(t_0) - u_i(t_0) \cdot \Delta t + \frac{1}{2} \cdot a_i(t_0) \cdot \Delta t^2 + \dots \\ \hline r_i(t_0 + \Delta t) &= -r_i(t_0 - \Delta t) + 2 \cdot r_i(t_0) + a_i(t_0) \cdot \Delta t^2 + \dots \end{aligned} \quad (2.3)$$

the new positions of the atoms can be determined if we know the present (t_0) positions, the positions of the previous timestep ($t_0 - \Delta t$) and the accelerations a_i .

To obtain the accelerations we need according to the left formula of eq.2.2 the force F_i , for which we need to define, according to the right formula, a potential or as mentioned otherwise a force field. The definition of this potential presents various challenges in the implementation of the method.

At this point it is important to mention the significance of the chosen timestep (Δt), which remains constant during the simulation. For a good description of the atomic bond vibrations the timestep needs to be small enough for the vibrations to be modeled correctly. One way to estimate the timestep is by considering the oscillation frequency of a harmonic oscillator:

$$\omega = \sqrt{\frac{k}{m}} \quad (2.4)$$

so,

$$\Delta t_{min} < \frac{2 \cdot \pi}{\omega} \quad (2.5)$$

Even then, vibrational properties of particularly light atoms may be extremely high and demand an even smaller timestep leading to higher computational cost. This leads to the *Timescale Dilemma*, which states that "Even though the number of atoms in a simulation can be easily increased by adding more processors (e.g. using parallel computing), time cannot be parallelized" [8].

In an MD simulation, since the system evolves in time, the time unit is an important parameter. In each simulation, the time unit depends on the units used for the energy, mass and distance. For example, if we use eV, amu, and Å as the energy, mass and distance units the time unit is calculated as:

$$\begin{aligned} E_{kin} &= \frac{1}{2} m u^2 = \frac{1}{2} \frac{L^2}{t^2} \rightarrow t = \sqrt{\frac{m(a.m.u.) \cdot L^2(A)}{2 \cdot E_{kin}}} \\ \rightarrow t_{unit} &= \sqrt{\frac{a.m.u. \cdot A^2}{eV}} \rightarrow t_{unit} = 35.28 fsec \end{aligned} \quad (2.6)$$

In our simulation the timestep = $0.02 \cdot t_{unit} = 0.707 fsec$.

¹Apart from the Verlet algorithm, the Leap-frog and the Beeman's algorithms are also used for updating the positions of the atoms

For the translation of the microscopic quantities (positions, velocities) to macroscopic observable properties of a material, such as energy, heat capacity, pressure, etc. the statistical mechanics character of the MD is required. All quantities are obtained as averages under a statistical ensemble. By integrating the Verlet equations (2.3) the total energy, E , of the system is preserved. Since the number of atoms, N , and the unit cell volume, V , are kept constant, the micro-canonical ensemble (NVE) is realized.

The canonical ensemble (NVT) is reached by changing the equations of motion since,

$$T = \frac{2}{3} \cdot \frac{K}{N \cdot k_B} \quad (2.7)$$

Another challenge in the implementation of the MD algorithm is the choice of the interatomic potential. For this several approaches exist. The choice of the potential for the *good* description of the system depends on the system itself. In this work, we used two different interatomic potentials who are both Morse type ($e^{-\alpha \cdot r}$) potentials (with many-atoms interactions); the Tersoff potential and the Brenner potential. Both are empirical potentials, meaning that their mathematical form is chosen in such a way as to describe the system correctly and several parameters are adjusted in each case to improve representation of the system. There is a constant improvement of these two potentials, for their implementation in various other systems, such as graphene. The Tersoff potential is implemented through the Ames Laboratory MD code[9] and the Brenner potential through the open source software LAMMPS[10]. A brief description of both will follow.

2.1.1 Tersoff Potential

The Tersoff potential [11] is a pair potential that includes effects of the "environment". Parameters exist for C, Si, Ge.

The basic idea is that the strength of a bond between two atoms depends not only on the in-between distance but also on the local environment.

The energy of the system is given by eq. 2.8

$$\mathcal{E} = \sum_i E_i = \frac{1}{2} \cdot \sum_{i \neq j} V_{ij} \quad (2.8)$$

with the potential V defined as

$$V_{ij} = f_C(r_{ij}) \cdot [f_R(r_{ij}) + b_{ij} \cdot f_A(r_{ij})] \quad (2.9)$$

where $f_R(r_{ij}) = A \cdot e^{(-\lambda_1 \cdot r_{ij})}$ and $f_A(r_{ij}) = B \cdot e^{(-\lambda_2 \cdot r_{ij})}$ are the repulsive and attractive part respectively.

The coefficient of the attractive part is the one that represents the effect of the local environment (where the many-body potential character comes from).

$$b_{ij} = (1 + \beta^n \cdot \zeta_{ij}^n)^{-1/2 \cdot n} \quad (2.10)$$

$$\zeta_{ij} = \sum_{k \neq i, j} f_c(r_{ij}) \cdot g(\theta_{ijk}) \cdot e^{\lambda_3^3 \cdot (r_{ij} - r_{ik})} \quad (2.11)$$

$$g(\theta_{ijk}) = 1 + \frac{c^2}{d^2} - \frac{c^2}{d^2 + (h - \cos\theta_{ijk})^2} \quad (2.12)$$

The summation on the ζ_{ij} formula is done for the k neighbours of atom i . Also the cut-off piecewise function is defined as

$$f_c(r_{ij}) = \begin{cases} 1 & r \leq R - D \\ \frac{1}{2} \cdot [1 - \sin[\frac{\pi}{2} \cdot \frac{R-D}{D}]] & R - D < r < R + D \\ 0 & r \geq R + D \end{cases} \quad (2.13)$$

The cut-off radius of the system is $R+D$, meaning that Tersoff potential doesn't take into account long range interactions.

In all the above equations the i, j, k denote the interacting atoms, r_{ij} is the distance between the i and j atoms, and θ_{ijk} is the angle between the i, j and k atoms. All the other parameters are derived from experimental data.

| Parameters | $C[\text{u}]$ |
|----------------------------|------------------------|
| A(eV) | 1393.6 |
| B(eV) | 346.7 |
| $\lambda(\text{\AA}^{-1})$ | 3.4879 |
| $\mu(\text{\AA}^{-1})$ | 2.2119 |
| β | $1.5724 \cdot 10^{-7}$ |
| n | 0.72751 |
| c | $3.8049 \cdot 10^4$ |
| d | 4.384 |
| h | -0.57058 |
| R(\AA) | 1.95 |
| D(\AA) | 0.15 |
| λ_3 | 0 |

Fig. 2.2: Carbon parameters for the Tersoff potential

While this potential is good for the representation of carbon systems, there are two basic things missing. The first is the lack of variety in the type of chemical elements we

can include in the simulation, and the second is lack of the representation of torsion. Both these problems are somewhat solved with the Brenner potential.

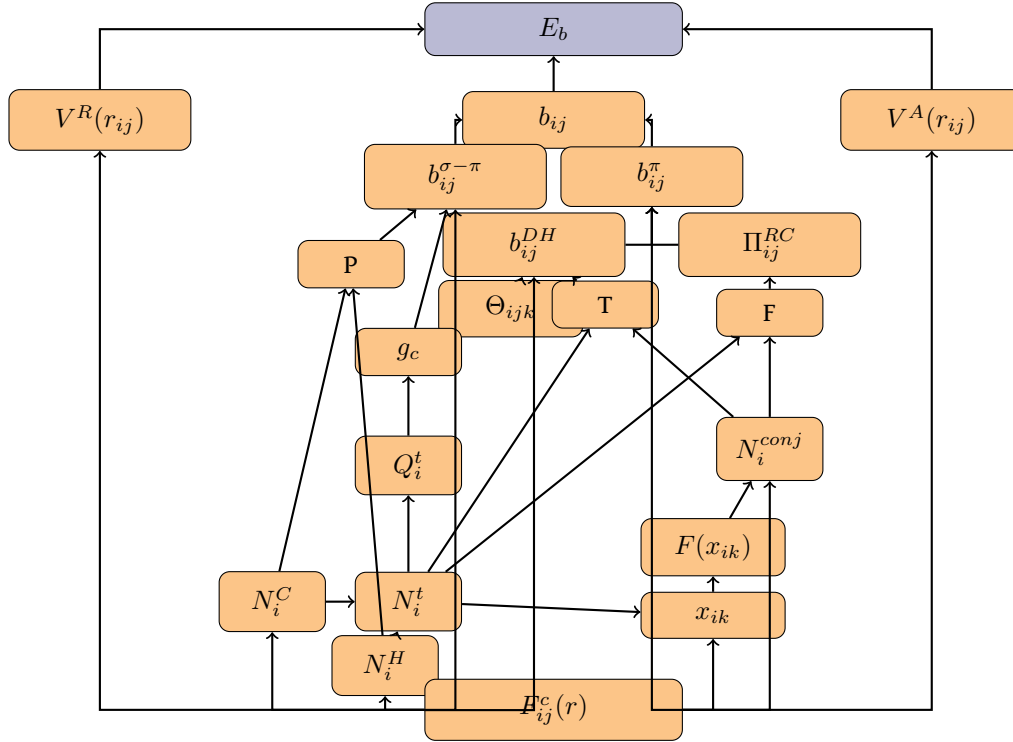


Fig. 2.3: Schematic illustration of the functions involved in the implementations of the Brenner potential

2.1.2 Brenner Potential

The Brenner potential [12], [13] is another bond order empirical potential, widely used for hydrocarbons, with the potential energy of the system given by eq. 2.14

$$V_{ij} = f_C(r_{ij}) \cdot [f_R(r_{ij}) + \bar{b}_{ij} \cdot f_A(r_{ij})] \quad (2.14)$$

where

$$f_R(r_{ij}) = \left(1 + \frac{Q}{r_{ij}}\right) \cdot A \cdot e^{(-\alpha_1 \cdot r_{ij})} \quad (2.15)$$

and

$$f_A(r_{ij}) = \sum_{n=1}^3 \cdot B_n \cdot e^{(-\lambda_n \cdot r_{ij})} \quad (2.16)$$

are the repulsive and attractive part respectively.

The coefficient of the attractive part is the one that again represents the effect of the local environment and is defined as:

$$\bar{b}_{ij} = \frac{1}{2} \cdot [b_{ij}^{\sigma-\pi} + b_{ji}^{\sigma-\pi}] + b_{ij}^{\pi} \quad (2.17)$$

where $b_{ij}^{\sigma-\pi}$ and $b_{ji}^{\sigma-\pi}$ are terms that depend on the local coordination and bond angles for the i and j atom respectively. With the last term given by the formula:

$$b_{ij}^{\pi} = \Pi_{ij}^{RC} + b_{ij}^{DH} \quad (2.18)$$

where the first term is there to determine whether the bond between atoms i and j is part of a conjugate system and the second term depends on the dihedral angle of carbon-carbon bonds. The local coordination and angle contribution is given from the equation:

$$b_{ij}^{(\sigma-\pi)} = [1 + \sum_{k \neq i,j} f_{ik}^C(r_{ik}) \cdot G(\cos(\theta_{ijk})) \cdot e^{\lambda_{ijk}} + P_{ij}(N_i^C, N_i^H)]^{-1/2} \quad (2.19)$$

The above, are the basic equations implemented in the Brenner potential, in which i, j, k denote the interacting atoms, r_{ij} is the distance between the i and j atoms and θ_{ijk} is the angle between the i, j and k atoms. A full schematic of all equations involved is shown in fig.2.3. All the other parameters are derived from experimental data.

2.2 Density Functional Theory

Classical simulation methods like Molecular Dynamics or Monte Carlo do not take into account the presence of electrons and cannot describe electronic properties. For this, Quantum Mechanics comes into play.

For a system with M nuclei (n) at positions R_1, \dots, R_M and N electrons (e) at positions r_1, \dots, r_N , the many-body, non-relativistic, time-independent Schrödinger's equation is:

$$\hat{H} \cdot \Psi(r_1, \dots, r_N) = E \cdot \Psi(r_1, \dots, r_N) \quad (2.20)$$

with the Hamiltonian

$$\hat{H} = \hat{T}_e + \hat{T}_n + \hat{U}_{ee} + \hat{U}_{en} + \hat{U}_{nn} \quad (2.21)$$

where

$$\hat{T}_e = -\frac{\hbar^2}{2 \cdot m_e} \cdot \sum_{i=1}^N \nabla_i^2 \quad (2.22)$$

is the kinetic energy operator for the electrons of the system,

$$\hat{T}_n = -\sum_{n=1}^M \frac{\hbar^2}{2 \cdot M_n} \cdot \nabla_n^2 \quad (2.23)$$

the kinetic energy operator for each nucleus and

$$\hat{U}_{ee} = \frac{1}{4 \cdot \pi \epsilon_0} \frac{1}{2} \sum_{i,j=1, i \neq j}^N \frac{e^2}{|\vec{r}_i - \vec{r}_j|} \quad (2.24)$$

,

$$\hat{U}_{nn} = \frac{1}{4 \cdot \pi \epsilon_0} \frac{1}{2} \sum_{n,m=1, n \neq m}^M \frac{Z_n \cdot Z_m e^2}{|\vec{R}_n - \vec{R}_m|} \quad (2.25)$$

and

$$\hat{U}_{en} = -\frac{1}{4 \cdot \pi \epsilon_0} \sum_n^M \sum_i^N \frac{Z_n \cdot e^2}{|\vec{r}_i - \vec{R}_n|} \quad (2.26)$$

are the Coulombic repulsions between electrons-electrons, nuclei-nuclei and the Coulombic attraction between electrons and nuclei of the system, respectively.

The exact solution of these equations is very difficult to find and that is why approximations are required. Since $m_n \gg m_e$, the electrons adjust to the movement of the nuclei almost instantly so, the degrees of freedom connecting the motion of the nuclei with the motion of the electron can be separated (*Born-Oppenheimer approximation*(BO)). Within the BO approximation, the wavefunction can be separated in the electronic and the nuclear part.

$$\Psi_{total}(\vec{r}, \vec{R}) = \Psi_n(\vec{R}) \Psi_e(\vec{r}) \quad (2.27)$$

From the electron point of view the \hat{T}_n term can be neglected and the \hat{U}_{nn} term can be considered a constant.

Density Functional Theory (DFT)[14] is based on two basic theorems proven by Hohenber & Kohn[15] and a set of equation introduced by Kohn & Sham[16]. The first theorem states that: "The ground state energy from Schrödinger's equation is a unique functional of the electron density"

$$E_0 = E(n_0(\vec{r})) \quad (2.28)$$

The second theorem states that: "The electron density that minimizes the energy of the overall functional is the true electron density corresponding to the full solution of the Schrödinger equation"(Variational principle).

$$E_0 = \min E(n(\vec{r})) \quad (2.29)$$

The electron density $n(\vec{r})$ represents the probability that N electrons are at a particular set \vec{r} of coordinates.

What is expressed according to these theorems is that the energy functional can be separated into two different terms the *known* part and the *exchange-correlation*(XC)

part, which includes all the not known quantum-mechanical effects. Still, the solution of the resulting equation is very difficult to find. This obstacle can be bypassed with the equations proposed by Kohn & Sham, which focus on a single particle wave function solution.

Now, eq.2.21 becomes:

$$\left[-\frac{\hbar^2}{2 \cdot m} \nabla^2 + V_{ne}(\vec{r}) + V_H(\vec{r}) + V_{XC}(\vec{r})\right] \psi_i(\vec{r}) = \varepsilon_i \psi_i(\vec{r}) \quad (2.30)$$

where V_{ne} is the Coulombic interaction between the electron and the nuclei, V_H is the Hartree potential defined as $V_H(\vec{r}) = e^2 \int \frac{n(\vec{r}')}{|\vec{r}-\vec{r}'|} d^3\vec{r}'$ which describes the repulsion of an electron and the electron density of the system, the self interacting character of this potential emerges from the fact that the electron described has also been taken into account in the electron density of the system. The last potential is the exchange-correlation potential defined as the functional derivative of the exchange-correlation energy.

$$V_{XC}(\vec{r}) = \frac{\delta E_{XC}(\vec{r})}{\delta n(\vec{r})} \quad (2.31)$$

The self consistent cycle of solving the Kohn-Sham equations consists of the following steps:

- Guess $n(\vec{r})$
- Solve the Kohn-Sham equations to find $\psi_i(\vec{r})$
- Calculate $n_{KS} = 2 \cdot \sum_i \psi_i^*(\vec{r}) \psi_i(\vec{r})$
- If $n_{KS}(\vec{r}) = n(\vec{r})$ then $n_{KS}(\vec{r})$ is the ground state electron density $n_0(\vec{r})$
- If not, then we change the electron density and try again.

For this self consistent solution we need to define an exchange-correlation functional. The only case that this functional is known is the electron gas, where the electron density is constant for a point in space. So the exchange-correlation potential can be written in the form

$$V_{XC}(\vec{r}) = V_{XC}^{electron\ gas}[n(\vec{r})] \quad (2.32)$$

Since only the local density is used in the definition, this functional is called *Local Density Approximation*(LDA) functional[17] and is one of the most popular exchange-correlation functional along with the *Generalized Gradient approximation*(GGA)[18] which not only takes into account the local electron density of a system but also its local gradient.

$$V_{XC}(\vec{r}) = V_{XC}^{electron\ gas}[n(\vec{r})] \cdot F[n(\vec{r})] \quad (2.33)$$

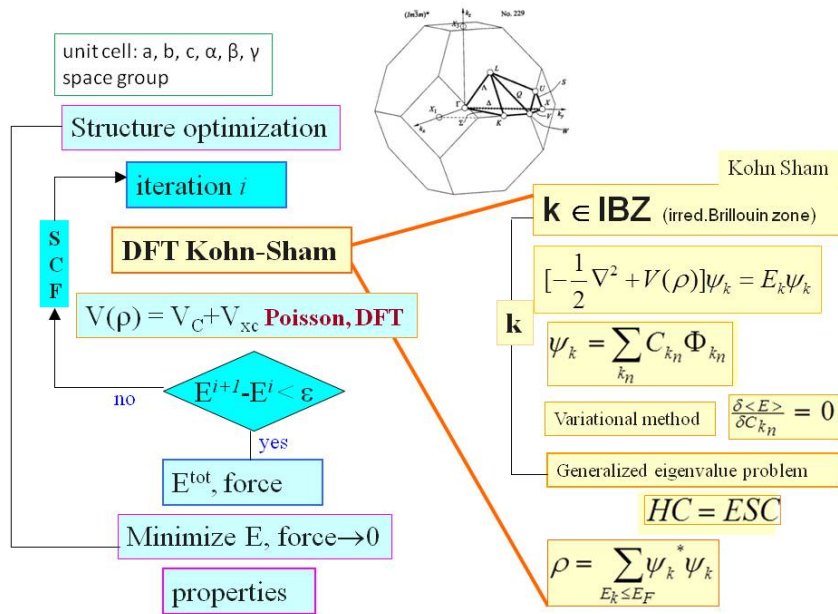


Fig. 2.4: Schematic illustration of the major steps in DFT electronic structure calculations: self-consistent field (SCF) cycle; Kohn-Sham equations solved within a \vec{k} -points loop. [19]

A schematic illustration with a DFT electronic calculation can be seen in fig. 2.4.

In this work the implementation of the DFT codes is done through two different softwares. The commercial VASP (Vienna *Ab initio* Software Package) and the open source GPAW (Grid-based Projector Augmented-Wave Method). Both are based on the projector augmented wave (PAW) method.

Vibrational Properties of Carbon Nanostructures

Modern methods in materials synthesis take advantage of the ability of carbon atoms to form bonds with different hybridizations and result in a variety of allotropic forms of carbon. Carbon-based nanostructures exhibit fundamental interest and have promising applications. Among these nanostructures, the mixed phase of amorphous carbon (a-C) and diamond nanocrystals (n-D) has been less studied and characterized, with many of its properties remaining unexplored. We perform atomistic simulations with empirical potentials in order to create several a-C-n-D samples with different n-D sizes and a-C densities, and samples of ultrananocrystalline diamond (UNCD) with various grain sizes. We analyze the structure, stability, and mechanical properties of these nanocomposite materials and our results compare well with experiment and previous simulations. Furthermore, we study their dynamical properties to find that some pronounced features of their vibrational spectra may be observed in experiments. Finally some effects of hydrogen on the properties of these materials are discussed.

3.1 Introduction

Carbon's ability to form composite structures with various properties makes it one of the most interesting elements. This ability is due to its different possible hybridizations (shown in fig. 3.1).

Apart from the fundamental interest and its important biological role, there are many promising applications based on carbon. Hydrocarbons are used as fuel, fibers, paints, solvents, etc. Most common forms like graphite are used in pencils and as brushes, while activated charcoal plays an important role in the purification/ filtration of water. Lightweight and strong carbon fibers are also extensively used. De-

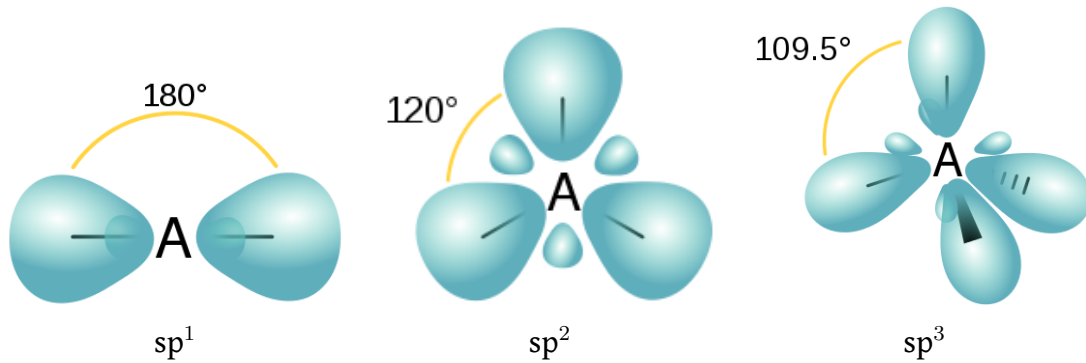


Fig. 3.1: Carbon hybridizations

pending on the allotropic form the properties of carbon materials vary. Recently, technological and scientific advances have taken advantage of the huge variety of allotropic carbon forms to create, study and use more exotic nanostructures (nanotubes, fullerenes, nanofoams, nanocones, etc). Carbon Nanotubes (CNTs) and fullerenes have been extensively studied for many applications, including hydrogen storage. Last but not least, atomically thin graphene, easily exfoliated from graphite, has turned the scientific interest to its direction with many promising properties as a stand alone structure or as a heterostructure.

Among the most interesting of the bulk carbon structures are the amorphous (a-C) and crystalline carbon (diamond). Even though these two phases have been studied extensively their mixed phase is less studied, with many difficulties in its characterization, especially in structures where Hydrogen is present introducing further difficulties.

Amorphous carbon is a complex phase that consists of carbon atoms with different hybridizations forming rigid three dimensional networks. Extensive research showed that the percentage of sp^3 , sp^2 and sp^1 atoms is mainly dependent on density. Different synthesis methods result in a variety of amorphous structures with different mechanical and optoelectronic properties [20], [21], [24], [22], [23].

In this work, we study the stability and some properties of this mixed phase in two main different configurations. The first one is the embedded spherical nanocrystals in an amorphous matrix and the other one is ultra-nanocrystalline diamond, which has recently attracted the scientific interest due to its interesting mechanical properties. The unit cell of the crystalline/diamond lattice consists of eight carbon atoms (fig.3.2). In our calculations the lattice constant of a single unit cell is 3.56\AA and the carbon-carbon bond is 1.54\AA . Also the density in this phase is $3.54\text{gr}/\text{cm}^3$.

For the structural characterization one of the most popular techniques is Raman spectroscopy, with many models (phonon confinement model (PCM), elastic sphere

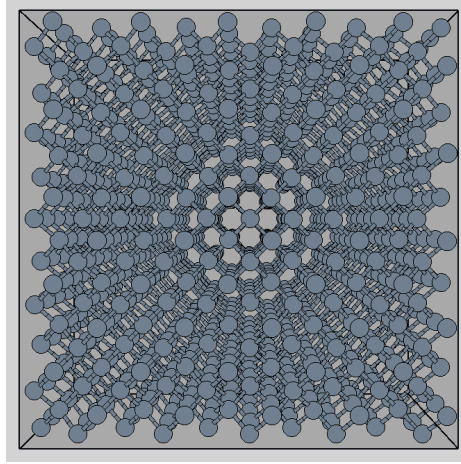


Fig. 3.2: Crystalline diamond structure of a Carbon super-cell

model (ESM) etc.) for the interpretation of the results. All these models mainly focus on the area of the D and G bands associated with the sp^2 and sp^3 content, respectively. In one of this studies, by Osswald et al. [25], they study the effect of phonon confinement in the Raman spectrum and observe a broadening and a shift to the left of the peak at 1250cm^{-1} as the size decreases from 10nm to 3nm.

In this work we propose that the size of a nanostructure can be obtained from the vibrational spectra. The idea is simple and comes from the known wave equation, the mathematical formula connecting the speed u of a wave with its wavelength λ and its frequency f as shown in 3.1:

$$u = \lambda \cdot f \rightarrow u_{dim} = d \cdot f \rightarrow f = \frac{u}{d} \quad (3.1)$$

where d is the diameter of the nanostructure and f is the vibration frequency. In order to compare our results with theoretical data, we use as reference that the sound velocity in diamond is around 12000m/s .

Understanding of the structural/mechanical properties and the spectroscopic signature of the structures before the addition of hydrogen is important in order to isolate the effects of hydrogen.

3.2 Results and Discussion

The evaluation of the Tersoff interatomic potential is done separately for the pure amorphous and crystalline phase of Carbon. We use properties like vibrational modes, bulk modulus, thermal expansion coefficient, radial distribution function, etc. to both demonstrate the cases where the Tersoff potential gives a good representation of the system in both phases, and also pinpoint its shortcomings.

3.2.1 Crystalline Carbon

Vibration Spectra

The vibrational spectra are used mainly for mining basic structural information. They are usually used in crystallography in order to determine the distance between two planes and the crystal structure, as well as in Chemistry for the identification of molecules and in Medicine for substance tracing. Experimentally the spectra are derived from techniques like Raman Spectroscopy and Infrared Spectroscopy. Computationally, the spectra are calculated from the change of the velocities over a period of time. For the transition from the time domain to the frequency domain we use the Discrete Fourier Transform(DFT)[26].¹

Tersoff potential slightly overestimates the vibrational frequencies of Carbon. A detailed comparison of the characteristic peaks of diamond can be found in table 3.1. We compare our results with computational [27] and experimental techniques [11] (such as Raman spectroscopy). As we can see, our results are within the acceptable

| Vibration type | Experiment (cm^{-1}) | Tersoff (cm^{-1}) | ALCMD (cm^{-1}) |
|------------------|--------------------------|-----------------------|---------------------|
| | | | 1000 atoms |
| LTO (Γ) | 1331 | 1561 | 1428 |
| LOA (X) | 1191 | 1300 | 1266 |
| TO (X) | 1077 | 1121 | 1110 |
| TA (X) | 801 | 804 | 924 |

Table 3.1: Vibration modes of carbon, Tersoff from [11] ALCMD with our MD simulations.

¹ In a simulation the calculation of the vibrational spectrum can be easily done, as we mentioned before, with the DFT. So, in order to do that we have to figure out the Nyquist Frequency which is given by the equation: $f_c = \frac{1}{2 \cdot \Delta}$ where Δ is our time step. $\Delta = 10 \cdot 0.02t_{unit} \Rightarrow \Delta = 0.2 \cdot 35.28fsec \Rightarrow \Delta = 7.07fsec$, so, the Nyquist Frequency is: $f_c = \frac{1}{2 \cdot \Delta} \Rightarrow f_c = \frac{10^{15}}{2 \cdot 7.07}Hz \Rightarrow f_c = 70.72THz \Rightarrow f_c = 2358.2388cm^{-1}$ (if $\Delta = 7 \cdot 0.02t_{unit} \Rightarrow f_c = 3378.9496cm^{-1}$)

error margins, compared with the other known values. A shift to higher values with the Tersoff [11] potential in comparison with the experiment is observed. This shift is also found when using the Brenner potential [31] but as it is mentioned, the main features are retained (such as the three peaks above 800cm^{-1}). In the spectra from our MD simulations we can observe a deviation of almost 100cm^{-1} (for the peak @ 1600cm^{-1}) and 65cm^{-1} (for the peak @ 1100cm^{-1}) whereas with the *ab initio*, tight-binding method the shift is less than 60cm^{-1} .

High activity in the low frequency region begins at approximately 350cm^{-1} . That makes it difficult to differentiate frequencies that are above 300cm^{-1} and consequently, as we'll see later, spherical nanostructures with diameter smaller than 1.35nm .

Bulk Modulus

Bulk Modulus is the property of a material that describes its compressibility. When pressure is applied to a material its volume will decrease and when the pressure is released the material will tend to return to its original state. The equation that expresses this is

$$B = -V \frac{\partial P}{\partial V} \quad (3.2)$$

where $P = \frac{-\partial E}{\partial V}$. In order to calculate the bulk modulus of Diamond Carbon, we use the following formula;

$$B = V \frac{\partial^2 E}{\partial V^2} \quad (3.3)$$

According to bibliographic data[32], the bulk modulus of diamond carbon is $B = 442\text{GPa}$. For the calculation of the bulk modulus of crystalline carbon we use a sample of 4096 atoms, the volume relaxation of which is shown in graph 3.3. After regressing the data,

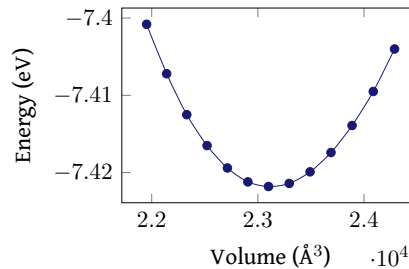


Fig. 3.3: Diamond Carbon relaxation

the equation that connects the energy per atom with the volume of the cell is : $E(V) = 0.21 - 6.59 \cdot 10^{-4} \cdot V + 1.42 \cdot 10^{-8} \cdot V^2$ (with a minimum at $(E, V) = (-7.4218, 23100.42)$ or $(E, a) = (-7.4218, 3.56)$).

With this the bulk modulus is calculated to be $B = 432\text{GPa}$ with an approximately 2% underestimation from the expected value. All the following values of bulk moduli are calculated in the same manner.

Thermal Expansion Coefficient

For the investigation of the behavior of the Tersoff potential with temperature we calculate the Thermal Expansion Coefficient (T.E.C.). Diamond has the smallest thermal expansion coefficient of any semiconductor [33]. The T.E.C. is calculated using the formula:

$$a_V = \frac{1}{V} \cdot \left(\frac{\partial V}{\partial T}\right)_P \quad (3.4)$$

and

$$a_L = \frac{1}{L} \cdot \left(\frac{\partial L}{\partial T}\right) \quad (3.5)$$

for the volumetric and linear approach respectively. The reference values for the T.E.C. of Diamond range from $1.1 \cdot 10^{-6} K^{-1}$ [34] to $1.18 \cdot 10^{-6} K^{-1}$ ($T_0 = 0K$)[35], With extremes at $2 \cdot 10^{-6} K^{-1}$. These values changes the length of the sample less than 0.03%, which is almost undetectable from the Tersoff potential. That's why an evaluation of the T.E.C. is needed.

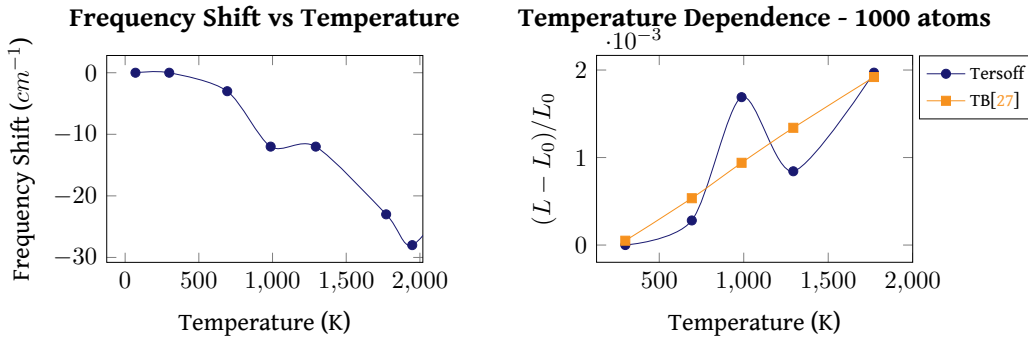


Fig. 3.4: Frequency Shift vs Temperature and the temperature dependence of the lattice parameters of a sample with 1000 atoms

By observing the spectra of graph 3.5² we detect a red shifting of the peaks with the increase of temperature. A detailed graph with the frequency shifts vs Temperature, of the main peak ($@1400\text{cm}^{-1}$) that can be distinguished from the spectra, can be seen in fig.3.4

²The spectra in the image 3.5 have been filtered with a Lorentz-Cauchy distribution whose probability density function is given by the following formula, $f(x; x_0, \gamma) = [\pi \cdot \gamma \cdot [1 + ((x - x_0)/\gamma)^2]^{-1}]^{-1}$. In our case the location parameter $x_0 = 1435\text{cm}^{-1}$ and the scale parameter $\gamma = 100$

In the work done by Clen et al. [28] and Schelling et al. [29] with the use of the Tersoff potential the thermal expansion coefficient is calculated at around $6 \cdot 10^{-6} K^{-1}$. Here the T.E.C. is calculated to be $1.28 \cdot 10^{-6} K^{-1}$ with a deviation less than 10% from the bibliography.

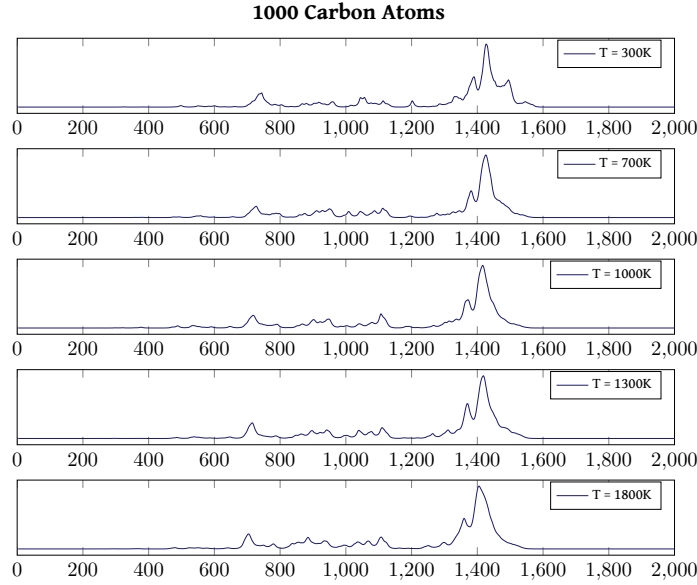


Fig. 3.5: Spectra for various temperatures in a sample of 1000 atoms. The y-axis denotes intensity in a.u.

The right graph in fig. 3.4 describes the temperature dependence of the lattice parameters and from which we calculate the T.E.C.. The graph on the left show the frequency shift compared to the temperature for the peak at around $1400 cm^{-1}$.

As mentioned in other works [27] using Tight-Binding Molecular Dynamics (TBMD) the shift of the LTO (Γ) peak (which is found around $1250 cm^{-1}$) from $T=100K$ to $T=850K$ is about $20 cm^{-1}$. In other recent experimental results [30] the frequency shift of the same peak (which is measured at around $1332 cm^{-1}$ from $T=280K$ to $T=600K$) is about $9 cm^{-1}$. In our data, the down-shift of that peak, found at $1428 cm^{-1}$ from $T=300K$ to $T=1000K$ is $12 cm^{-1}$.

3.2.2 Amorphous Carbon (a-C)

Sample Preparation

For the examination of the Tersoff potential's behavior with amorphous carbon (a-C) structures, we prepare samples with different densities. The preparation procedure mimics the experimental process for the creation of an a-C sample. In order to extract some of the mechanical and structural properties of the material, each of the samples has different initial density. First we heat the crystalline carbon sample and let the system evolve at 12000K for 14psec. An a-C structure is generated by cooling the above liquid to the final temperature of 0K at the rate of 140K/psec. A schematic representation of the procedure described above can be seen in image 3.6

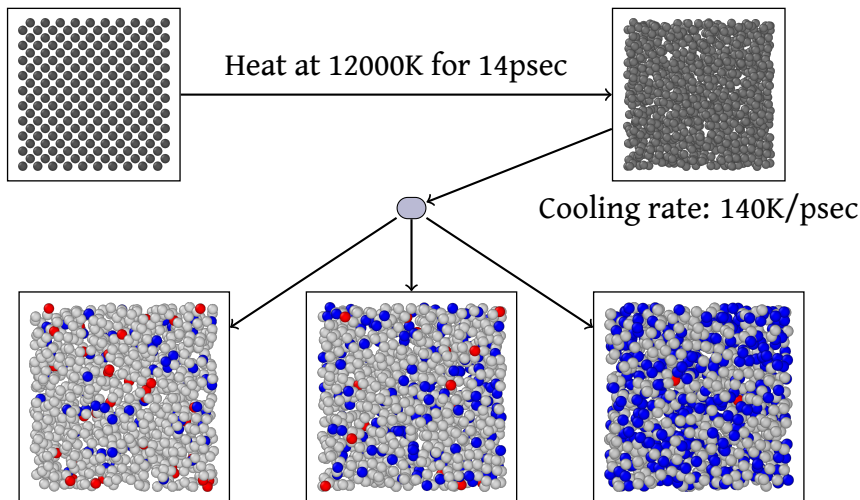


Fig. 3.6: Schematic representation of the preparation procedure. The grey atoms denote Carbon atoms in crystalline or amorphous phase, while the hybridizations are denoted with red, white and blue for sp^1 , sp^2 and sp^3 respectively. The resulting densities shown in the right, center and left image above are 3.00, 2.59, 2.28 gr/cm^3 respectively

Typical Sample

A fully detailed description of all a-C samples' input and output values can be found in Appendix A.3. In this section, we describe a typical a-C sample. In fig.3.7 we can see the input and output values related to this sample, as well as a snapshot of its final atom configuration.

It can be seen that the size of the unit cell increases from the crystalline phase to the amorphous phase as expected. So, the density decreases. As it is already shown[36],

| Output Data | 300K |
|-------------------------|---------|
| $a_{final}(\text{\AA})$ | 3.66 |
| $\rho_{final}(gr/cm^3)$ | 3.25 |
| $sp^1(\%)$ | 0.07 |
| $sp^2(\%)$ | 33.4 |
| $sp^3(\%)$ | 65.9 |
| $R(\text{\AA})$ | 1.52 |
| m.c.n | 3.644 |
| Bulk modulus(GPa) | 336.47 |
| Total Energy (eV/atom) | -6.9156 |

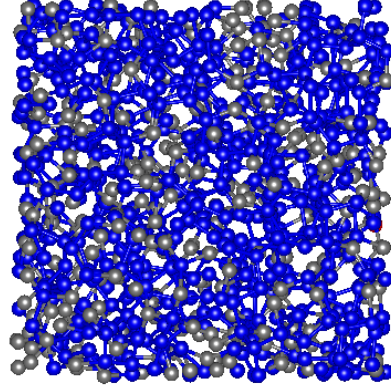


Fig. 3.7: Final configuration of a typical a-C sample. The sp^1 , sp^2 and sp^3 atoms are denoted with red, white and blue respectively

most of these values are correlated with density. For each sample apart from the properties shown in the table of fig.3.7, the radial distribution and vibrational spectrum are also calculated. Specifically for this specific sample these graphs can be seen in fig.3.8

Depending on which of the sp^3 and sp^2 percentages is dominant, the vibrational spectrum for all atoms displays the equivalent properties, i.e. the D and G peaks which are characteristic of the sp^2 bonds or the peak at around $1400cm^{-1}$ of the LTO(Γ) vibration mode, characteristic of diamond.

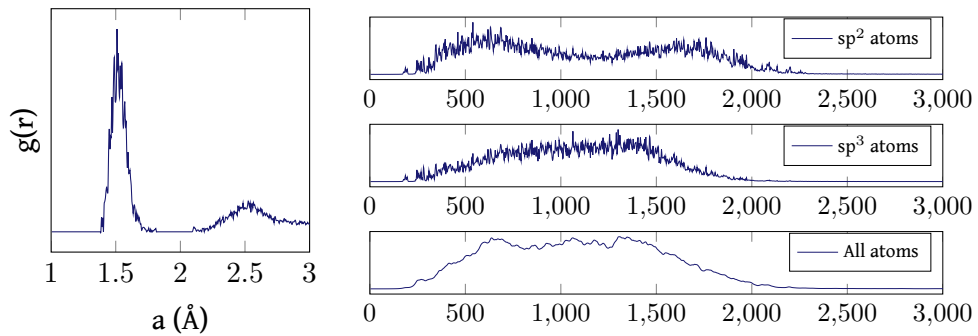


Fig. 3.8: Radial distribution function and Vibrational spectrum of the a-C typical sample

The overall analysis of the a-C samples follows.

Radial Distribution Function (R.D.F.)

It has already been observed[36] that the nearest neighbour distance (estimated from the radial distribution function(R.D.F.)), should increase when the density of the structure increases. This shift is indeed observed with the Tersoff potential. This is an expected result since the nearest neighbour distance for graphite (which consist mainly from sp^2 atoms) is 1.43\AA whereas in diamond (a fully sp^3 structure) is 1.54\AA .

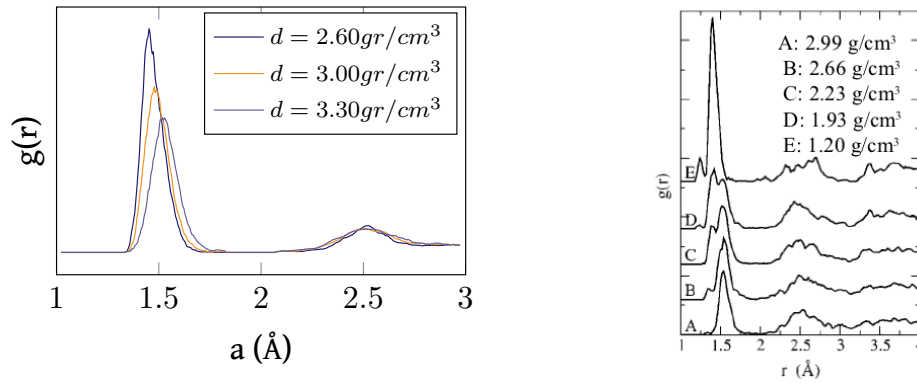


Fig. 3.9: Radial Distribution Function calculated with Tersoff and the Environment Dependent Tight-Binding[36]

Mean Coordination Number and Sp^3 Fraction

The mean coordination number \bar{z} of a system describes the average number of the nearest neighbours of a system and it can be experimentally determined by various techniques (e.g Extended X-ray Absorption Fine Structure (EXAFS) experiment, and X-ray Computerized Tomography (CT)[37])

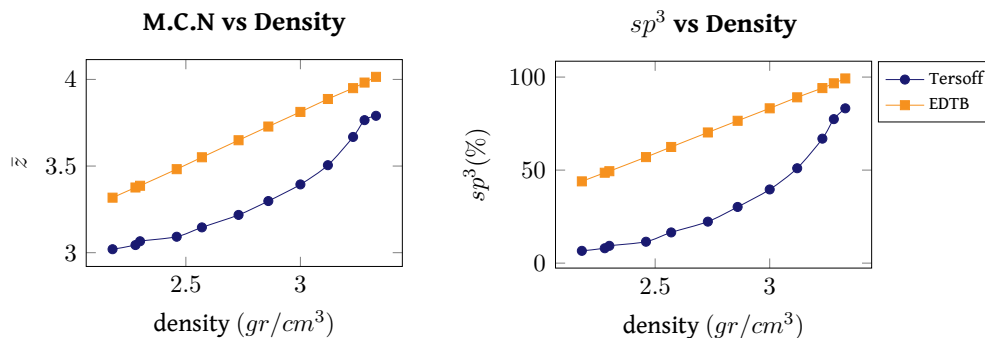


Fig. 3.10: Mean coordination number versus density. TB results from[36]

From this analysis we see that the Tersoff potential underestimates the mean coordination number. Consequently, the sp^3 fraction is underestimated as well. In the `` sp^3

vs density" graph of fig.3.10, the results of Tight-binding Molecular Dynamics [36] are also compared with the results of the Tersoff potential. As shown in the graph on the right, our curve is not a good representation for low densities, but Tersoff potential is suitable for high density a-C.

Bulk Modulus vs Mean Coordination Number (m.c.n.)

For the calculation of the bulk modulus we follow the same procedure described before. As we can see from diagram 3.11 Tersoff potential overestimates the bulk modulus, with an almost linear dependency between the bulk modulus and the m.c.n. This comes in contrast to the results obtained with the EDTB model where: $B = 167.3 * (\bar{z} - 2.33)^{1.5}$.

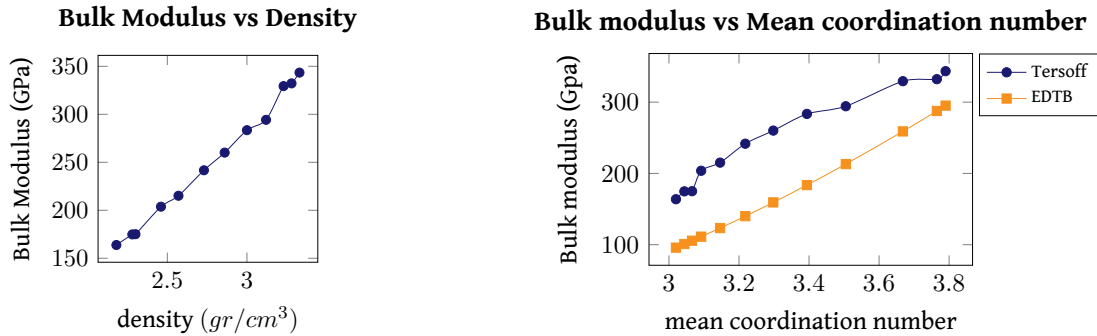


Fig. 3.11: Bulk modulus graphs

Vibration Spectra

From the vibrational spectra of amorphous structures we can extract various useful information about basic lattice properties. A typical graph can be seen 3.8, where we can observe the two characteristic wide peaks D (disorder) and G (graphitic), both from sp^2 bonds. Usually [38], the D peak is observed at $1350cm^{-1}$ and the G peak is observed at $1580cm^{-1}$. These two modes (fig. 3.12) are really important in the characterization of an amorphous carbon sample, since their shifting can be used in the estimation of the sp^3 and sp^2 content. From the sp^3/sp^2 ration many structural parameters can be estimated. Moreover, from the shifting of the G mode we can calculate the Tauc gap, which is often used to characterize optical properties of amorphous materials.

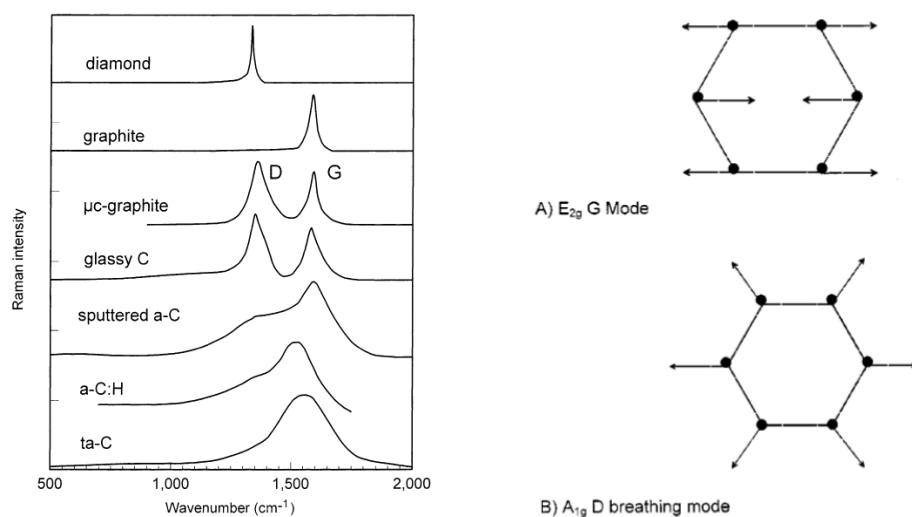


Fig. 3.12: In the right panel a comparison of typical Raman spectra of Carbon is shown [23] and in the left panel a schematic representation of the two vibration modes [38]

3.2.3 Free Spherical Nanostructures(n-D)

Here we present the results of free spherical carbon nanocrystals ("free" n-D). With this term, we define spherical nanocrystals with diameters varying from 2.00nm up to above 5.00nm. Each unit cell has an at least 1nm vacuum in each direction. A typical image of an n-D is shown in fig. 3.13. The preparation protocol for these structure is as follows. We heat each sample at 200K for about 2psec. All the structural values are calculated after the structure is cooled down to 0K, while the vibrational density of states (VDOS) is obtained after a canonical (NVT) ensemble at 200K during a micro-canonical (NVE) ensemble. With thermal annealing up to 1500K we verify that these structures are stable. The resulting size of each spherical nanostructure can be calcu-

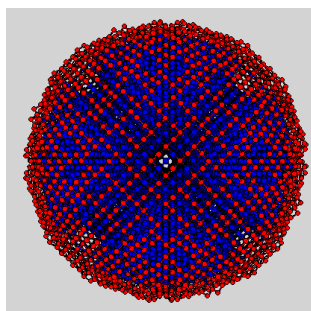


Fig. 3.13: Typical n-D sample

lated in two ways. In the first we use the first neighbour distance obtained from the $g(R)$ curve to estimate the volume and consequently the diameter of the nanostructure ($D_{g(R)}$). In the second way we measure the distance between two diametrically opposed atoms of the spherical nanostructure ($D_{measured}$), since the nanospheres are well defined. A small contraction in the size of the n-D after annealing is observed. In table A.4 all input and output parameters are presented. Next, the VDOS for each

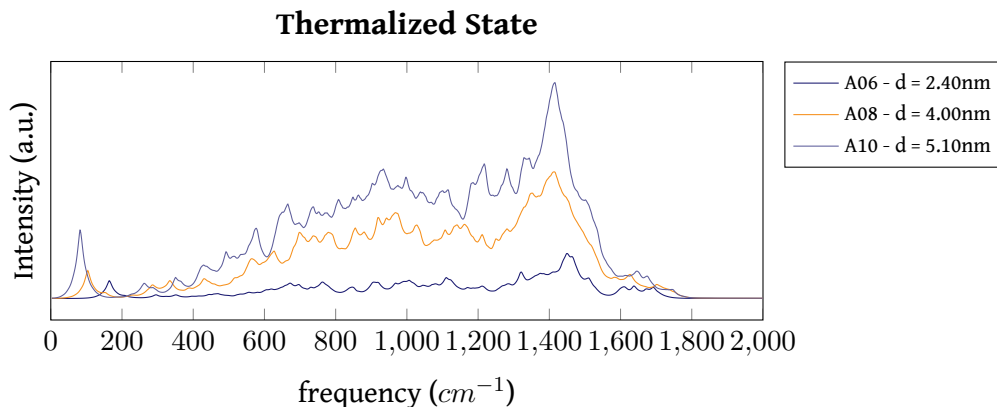


Fig. 3.14: Spectra for Free-n-D

sample is calculated. In fig. 3.14 we see the spectra for three samples with diameters 2.40nm, 4.00nm and 5.10nm in their thermalized state (200K). In these we can clearly observe the characteristic diamond peak at around 1400cm^{-1} (LTO(Γ)) and also, a slight tilt in the spectrum indicates one more peak close below 1000cm^{-1} (TA(X) or TO(X)).

Another interesting peak is observed in the low frequency region, which becomes more prominent in an "excited" state of the structure as shown in fig. 3.15. This "excited" state refers to the state of the structure after minor isotropic expansion.

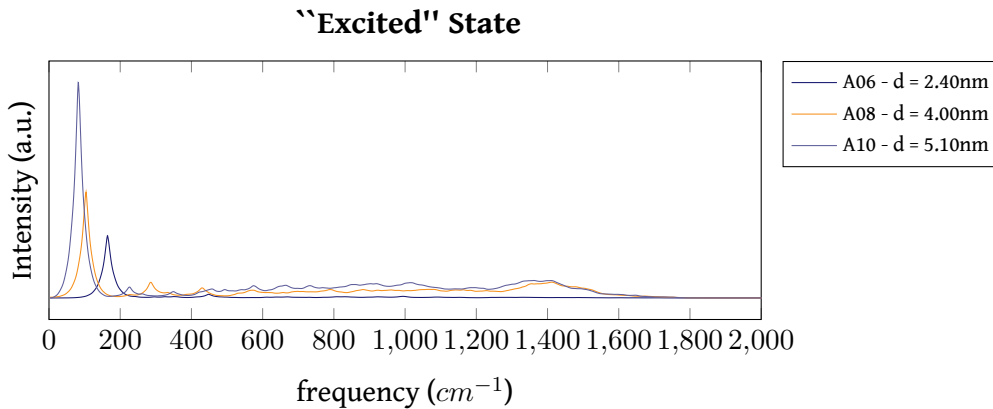


Fig. 3.15: Spectra for Free-n-D

The theoretical assumption we made, that connects the vibration frequency with the size of the nanosphere is verified for the free n-Ds. Figure 3.16 on the left shows the *Frequency versus Diameter* graph and on the right shows the graph of *Frequency versus 1/Diameter*, both for the measured diameters and the ones estimated from the $g(R)$ curve. In the same graphs we also see the frequencies that correspond to these diam-

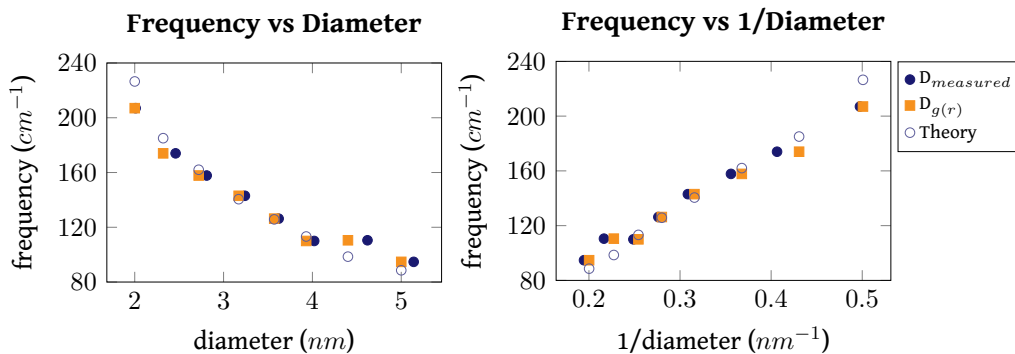


Fig. 3.16: Frequency vs Diameter and 1/Diameter graphs of the free spherical nanostructures (n-D)

eters according to the theoretical prediction, where 12000m/s is use as sound velocity

in diamond. By fitting our data to a least squares curve we estimate the sound velocity to be 13613m/s.

We also see that this theory fits better for spherical nanostructures with diameters close to 3nm, which is the size of the nanostructures mostly observed in experiments[39]. For smaller samples the size is underestimated whereas for bigger samples its overestimated.

3.2.4 Spherical Nanocrystals Embedded in Amorphous Carbon (n-D - a-C)

Although the results of the n-D samples show a clear agreement with the theoretical assumption, they are an isolated system difficult to be observed experimentally. We investigate samples with spherical carbon nanocrystals (right image in fig.3.17) embedded in a amorphous carbon matrix (a-C - n-D)(right image in fig.3.17) which are observed in experiments[39]. Theoretical studies of optical properties of a-C - n-D have shown that these are dominated by the optical properties of the a-C phase that surrounds the n-D structure[40]. In this section, we present the results concerning these structures. Our samples consist of spherical nanocrystals with various diameters varying from 2.00nm up to above 7.00nm, within amorphous carbon with various initial densities.

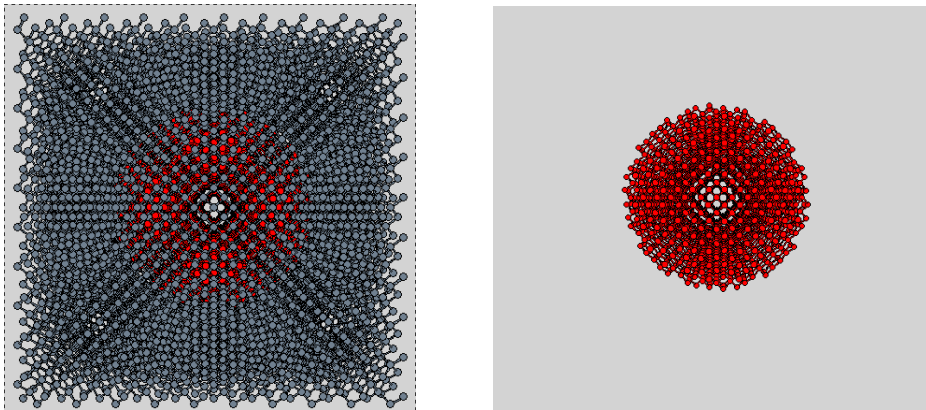


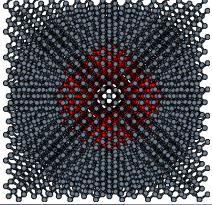
Fig. 3.17: Typical a-C - n-D sample. On the left we see the full structure and on right only the embedded spherical nanocrystal

For the preparation of each sample, we start from a crystalline carbon structure which we heat at 12000K for 14psec maintaining motionless the atoms of the embedded sphere. An a-C structure is generated around the sphere by cooling the above liquid to the final temperature of 0K at the rate of 140K/psec. At this point we release the sphere atoms and reheat the sample at 700K for about 2psec and finally reduce the temperature at 0K. From this point on, the preparation protocol followed is the same as the one for the free spherical nanocrystals.

For each sample, various parameters are tested, such as the quenching rate, the initial density of the amorphous matrix, the initial density of the embedded nanostructure and the relation between the size of the nanostructure and the size of the unit cell. For our final results, as we will see later, we consider various factors. A fully detailed table with the input and output data of the a-C - n-D samples is presented in table A.5.

A detailed analysis for some individual properties of a sample is presented next. In figure 3.18 we can see the input and the output parameter related to the sample, as well as an image of the input unit cell, where d_{init} is the initial size of the n-D sphere, ρ_{init}

| Sample B09 | Input Data |
|------------------------|------------|
| $d_{init}(nm)$ | 2.03 |
| Cell Length (nm) | 3.01 |
| $\rho_{init}(gr/cm^3)$ | 3.45/3.00 |
| QR(K/ps) | 140 |
| N_{tot} | 4096 |
| $N_{c_{init}}$ | 633 |



| Sample B09 | Output Data |
|-------------------|-------------|
| Nc | 775 |
| Na | 3321 |
| R(Å) | 1.57 |
| $d_{final}(nm)$ | 2.07 |
| $\rho_c(gr/cm^3)$ | 3.33 |
| $\rho_a(gr/cm^3)$ | 2.97 |

| Sample B09 | Output Data |
|---------------------|-------------|
| $F_{sim}(cm^{-1})$ | 174.0 |
| $F1_{sim}(cm^{-1})$ | 194.02 |
| deviation1 (%) | 10.32 |
| $F2_{sim}(cm^{-1})$ | 184.32 |
| deviation2 (%) | 5.60 |
| $F3_{sim}(cm^{-1})$ | 163.14 |
| deviation3 (%) | 6.66 |

Fig. 3.18: Input data and initial atom configuration of a typical sample, as well as the output structural values at 0K and vibrational values at 300K

is the initial density of the n-D sphere and the amorphous (initially crystalline) matrix. QR is the quencing rate mentioned in the preparation protocol, N_{tot} is the total number of atoms and $N_{c_{init}}$ is the number of crystalline atoms (n-D sphere atoms).

In the output data at 0K, Nc and Na are the number of crystalline and amorphous atoms, R is the position of the first peak in the $g(R)$ curve of the crystalline atoms as shown in fig. 3.20(c) and d_{final} is the resulting from it size of the nanosphere. Also, ρ_c and ρ_a are the final densities of the crystalline and the amorphous phase respectively.

In the output data at 300K, F_{sim} is the position of the first prominent peak as seen in fig. 3.20(b), in the low frequency region of the Vibrational Density of States(VDOS). $F1_{sim}, F2_{sim}$ and $F3_{sim}$ is the expected position of this peak with the assumption that the velocity of sound in carbon is 12000m/s, 13613m/s and 10620m/s respectively as taken from the bibliography[41], and the mean and fitted values estimated from the free n-D spheres. deviation1, 2 and 3 are the equivalent deviations of the simulation from these values.

The graphs in figure 3.20 are obtained in two different stages of the preparation process. The R.D.Fs are obtained after the canonical (NVT) ensemble at 300K and 0K during a micro canonical (NVE) ensemble. Whereas, the VDOS graph was produced after a canonical ensemble at 300K followed by a micro canonical ensemble.

For precision, all the structural details (densities, number of amorphous and crystalline atoms) are obtained at 0K after an NVE ensemble. While, the vibrational spectrum is calculated after the NVE ensemble at 300K.

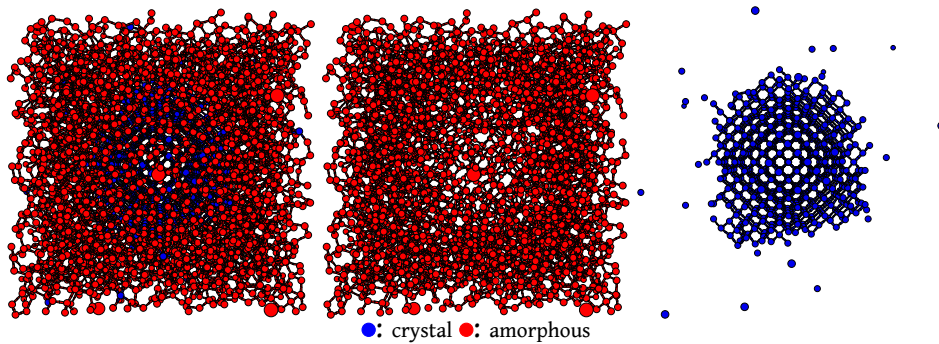


Fig. 3.19: Output configuration for the typical a-C - n-D sample

Consequently, the significant graphs are shown in fig.3.20. In the VDOS graph the diamond character, with the characteristic peak at 1400cm^{-1} , of the crystal atoms is evident and also the characteristic D and G peaks, at 800cm^{-1} and 1500cm^{-1} respectively, in the spectrum of the amorphous atoms can be slightly observed. What is quite obvious in the low frequency ($<300\text{cm}^{-1}$) region is a clear peak at 174cm^{-1} which coincides with our prediction regarding the size of the nanocrystal. A graph with the spectrum of all atoms can be seen in fig. 3.21.

Using the first peak of the radial distribution function of crystal atoms ($R=1.57\text{\AA}$) at 0K, we can calculate the size of the nanocrystal. In addition, we note the dispersion of the curve of the R.D.F at 300K, due to the increase in temperature.

In total we examine 32 different samples. The initial conditions for some of these samples can be seen in the table A.5. With these samples we examine the effects of different quenching rates, various combinations of initial densities for the a-C matrix and the n-D sphere. As mentioned before, a lower limit as far as the size of the nanostructure is concerned has been established, due to the difficulty to differentiate frequencies that are above 300cm^{-1} , thus, nanostructures with diameter smaller than 1.35nm are not included in the final study. The two neighbouring nanospheres are connected in samples with thin (less than 0.5\AA) a-C matrix around them, after the preparation procedure. Another factor that affects our samples is the initial difference between the density of the sphere and the matrix. We focus on high a-C densities where Tersoff gives correct results.

The final difference between amorphous phase's density and the density of the crystal phase's seems to be at around $0.30\text{gr}/\text{cm}^3$. This can be seen in fig 3.22 in the Density vs Diameter graph, while the detailed distribution function is shown in 3.23. Our final sample sizes extend from 1.5nm to 6nm in diameter.

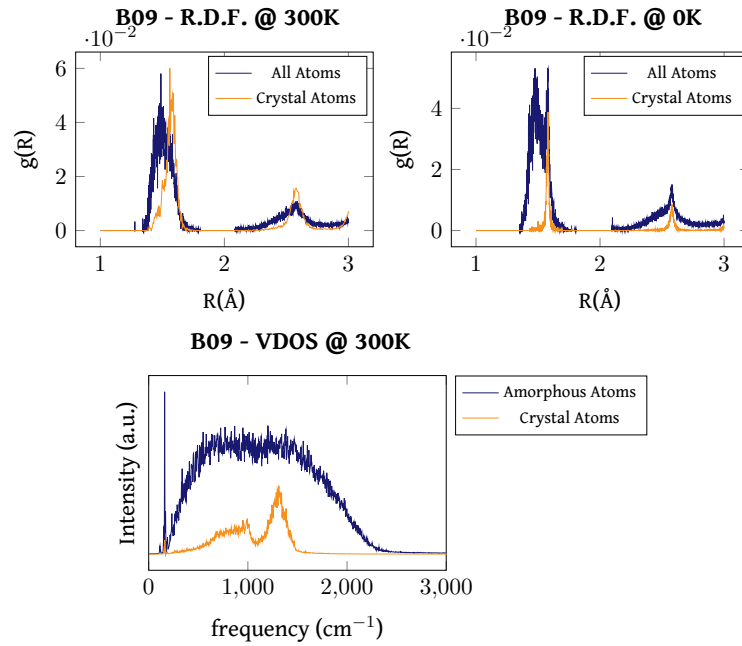


Fig. 3.20: Radial Distribution Function and Vibrational Density of States in different stages of the preparation protocol

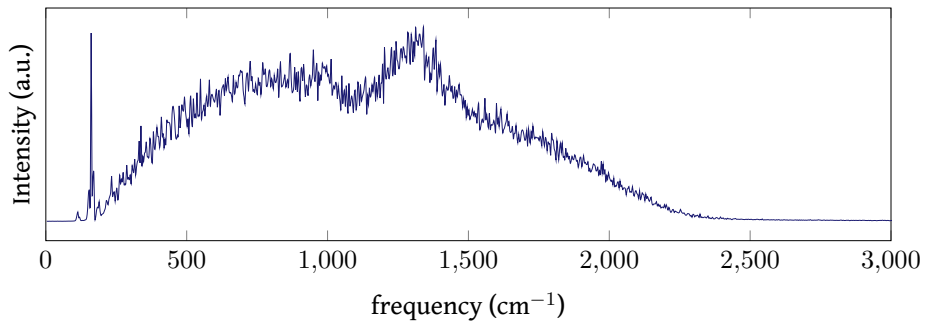


Fig. 3.21: VDOS of the typical sample at 300K for all the atoms of the sample

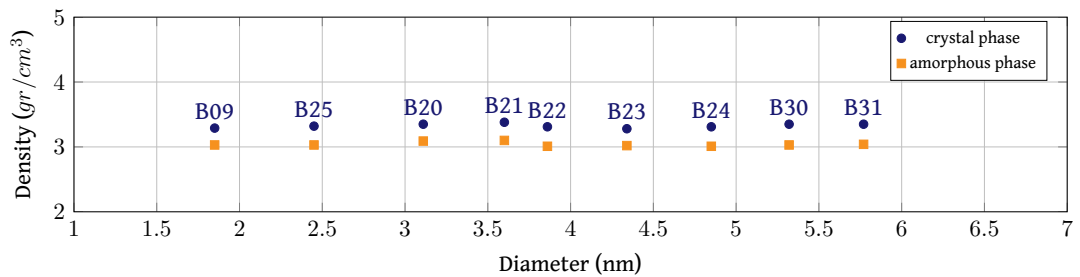


Fig. 3.22: Diameter versus density for all the a-C - n-D samples

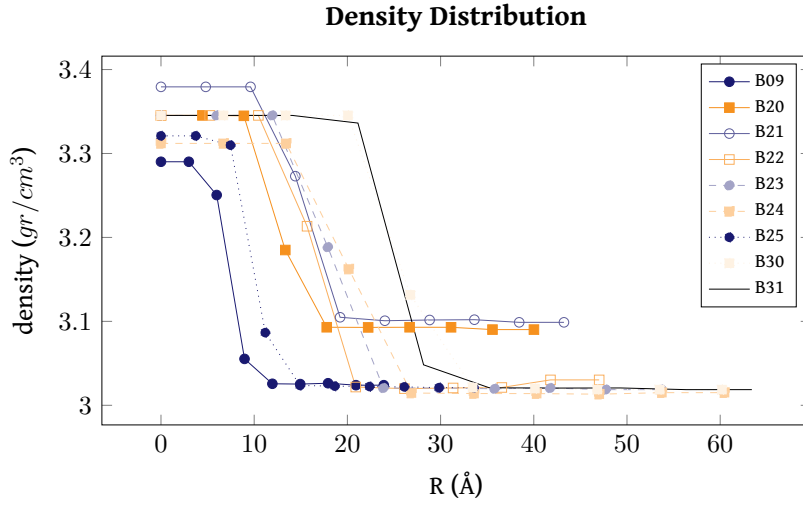


Fig. 3.23: Density Distribution for the a-C - n-D samples

Bulk Modulus

The bulk modulus is calculated for each sample, both for 0K and 300K. The bulk modulus (at 0K) of a structure that contains both the amorphous matrix and the diamond nanocrystals doesn't depend on either the total density of the structure or on the diameter of the nanostructure that is embedded in the a-C and remains almost constant at around 300GPa.

Formation Energy

For the stability of the a-C - n-D samples the formation energy of the nanocrystals is calculated. We define the formation energy as shown in equation 3.6

$$E_{form}(eV/atom) = \frac{N_{total} \cdot E_{totalSim}(eV/Atom) - N_a \cdot E_a - N_c \cdot E_c}{N_{total}} \quad (3.6)$$

where N_{total} , N_a and N_c are the number of the total, amorphous and crystal atoms respectively, $E_{totalSim}$ is the total energy obtained from the simulation and E_a and E_c are the total energy of the amorphous and the crystal atoms respectively as estimated. A structure is considered stable when its formation energy is below zero. A metastable structure has positive formation energy. In the left graph of figure 3.24 we see two different versions of the formation energy. In the first one (denoted with blue) E_a and E_c are calculated from the "Energy vs Density" graphs of the respective phase, already shown in the previous sections. In the second one (denoted with yellow) the E_a and E_c are extracted directly from the simulation. Both diagrams show that for most of our structures formation energy is below or very close to zero, which indicates

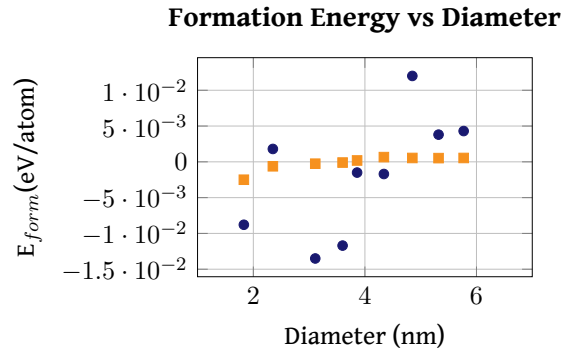


Fig. 3.24: Formation energy vs diameter graph

that our structures are stable or metastable. It is also observed that the *more stable* nanostructures are those around 3.00nm and that nanostructures above 6.00nm tend to be *less stable*.

Vibrational Density of States

Graph 3.25 is a typical VDOS graph of our samples. We observe the clearly distinguished peak that corresponds with the size of the nanostructure (n-D) at around 75cm^{-1} . We also see the two characteristic peaks of the amorphous phase of the sample. The latter two, can be seen at around 1100cm^{-1} and 1350cm^{-1} . It is interesting to note that those two peaks are further apart. Usually the D and G peaks can be found at around 1380cm^{-1} and 1580cm^{-1} respectively.

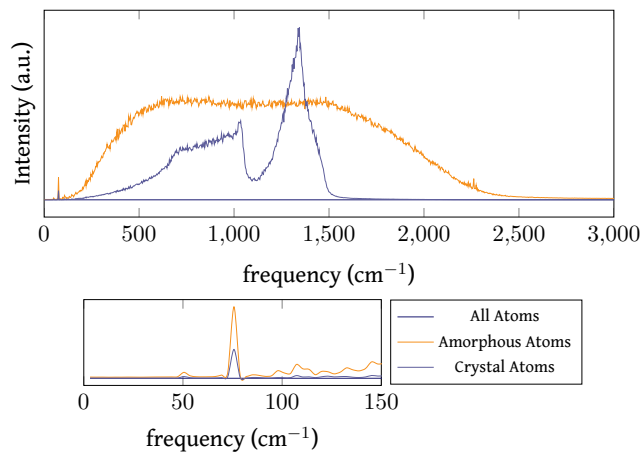


Fig. 3.25: VDOS for sample B31

Frequency -- Size of n-D

We have already "proved" that we can obtain the size of a free n-D. In figure 3.26 we can see a comparison of the vibration frequency versus the diameter of the nanocrystal that is embedded in the a-C, for our samples. We can see that the theoretical prediction

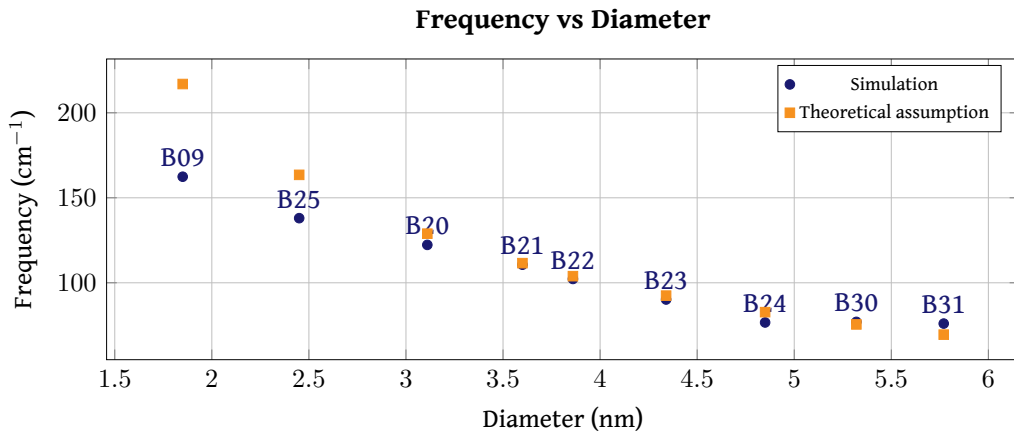


Fig. 3.26: Diameter versus frequency for final Samples

is very close to the data obtained from the simulation, especially for n-Ds with size greater than 3nm, which are better defined, as we can be seen from image 3.27.

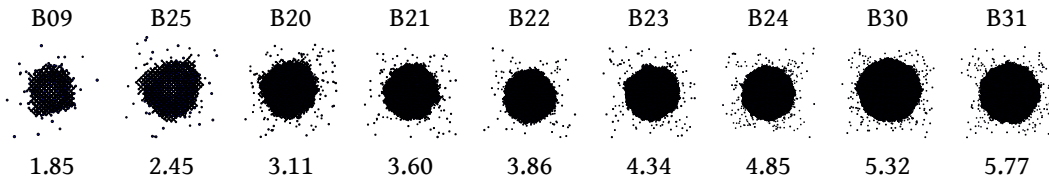


Fig. 3.27: Images of the embedded nanospheres of the a-C - n-D samples, with their labels and sizes(in nm)

The vibrational density of states for all of the final samples can be seen in image 3.29 We can clearly observe the decrease in frequency of the low-frequency peak. Also we can observe the sharpening in the diamond-peak (1350cm^{-1}) mentioned in this work [25]. But the pattern concerning the shift of this peak (to the left as the size of the nanostructure get bigger) is not observed. The peak seems to remain in the same position for nanocrystals smaller than 3nm in diameter and shifts to the right for nanocrystals bigger than 3nm. This pattern is also displayed in image 3.28

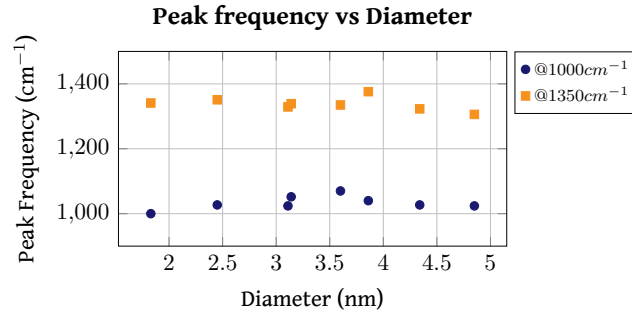


Fig. 3.28: n-D size versus peak frequency, @1000cm⁻¹ and @1350cm⁻¹ for final Samples

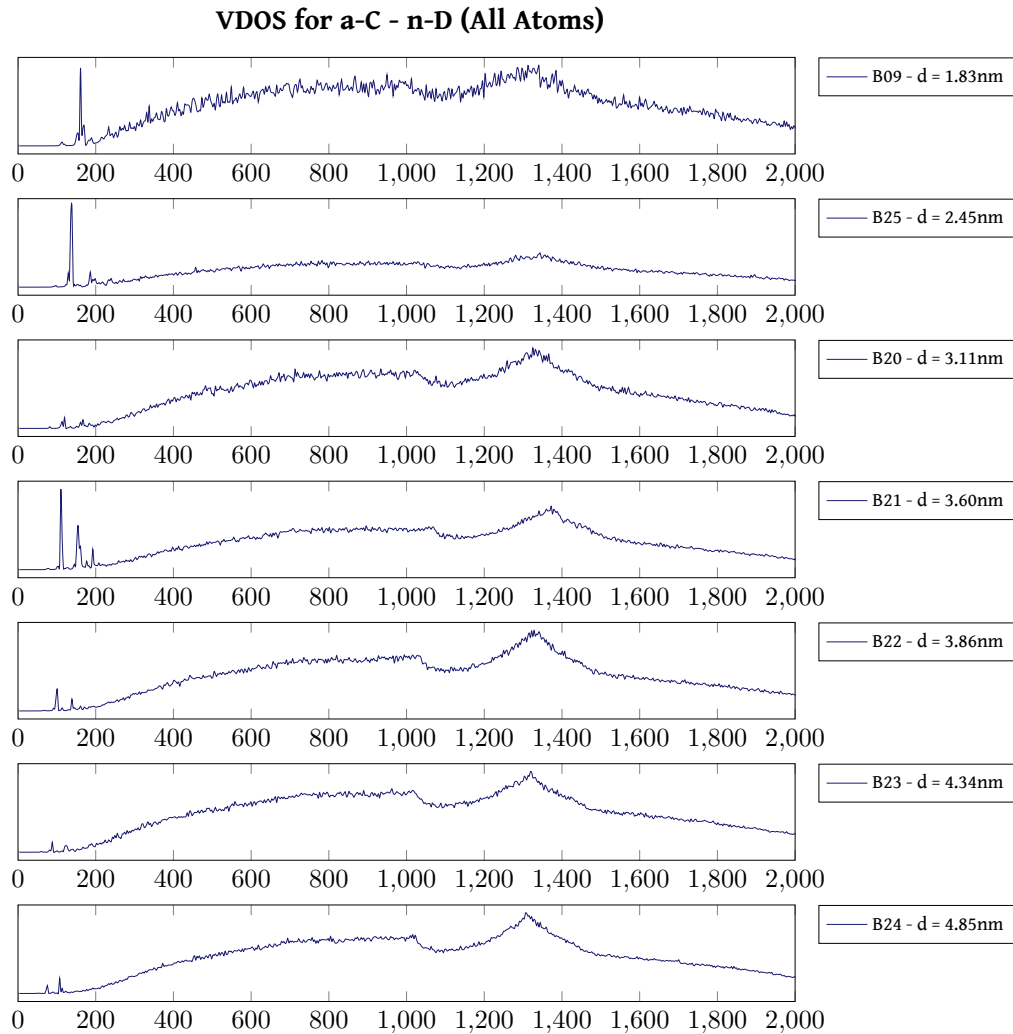


Fig. 3.29: Spectra for n-D-a-C

3.2.5 Ultra-Nanocrystalline Diamond (UNCD)

Our assumption that the size of a nanocrystal can be determined by observing the peaks in the low region of the vibrational spectrum has been proven correct for nanocrystals embedded in an amorphous matrix. In this section we investigate whether this statement is correct for Ultra-Nanocrystalline Diamond (UNCD).

UNCD is a popular material due to its good mechanical properties. In average the size of a UNCD grain ranges from 2 to 5nm [43]. In this work the average grain size ranges from 3.5 to 5nm. Each sample contains eight randomly oriented grains and is created by the Voronoi diagram construction method as provided by the CAMPOS ASE algorithm [44].

The preparation protocol is the following, the sample is heated at 300K and is slightly compressed to eliminate the grain boundary voids. Next, the structure is annealed at 800K for about 2ps and cooled to 300K with a quenching rate of 120K/ps. A

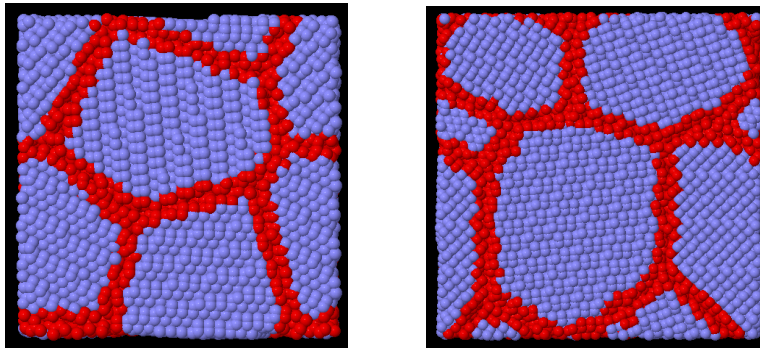


Fig. 3.30: Uncd typical samples. With blue spheres we denote the crystalline atoms and with red the amorphous grain boundary atoms

second annealing at 1200K ensures equilibration and finally a full relaxation is allowed at 300K. At this stage the velocities are obtained (that are needed for the vibrational spectrum) during a period of 10.6ps. In a previous work by Adiga et al. [45] in which they study the vibrational properties and specific heat of UNCD, they obtain the velocities after a 2.5ps period, but as we saw in the previous section, we get more clear results in the low frequency region if the sample remains in the micro canonical assembly for at least 10ps. Again all the structural parameters are obtained at 0K.

In fig. 3.30 we can see two typical samples. It can be seen that the size of the grains is random. Some grains are oval shaped and some are elongated. Table A.6 contains all the input and output details of our samples. Each unit cell contains from 25000 atoms up to 160000 atoms. The bulk modulus is estimated at 0K and 300K. Figure 3.31 shows the results of this calculation. As we can see our structures are much softer than the ones presented in [46] calculated with Monte Carlo (MC) Tersoff potential and the ones

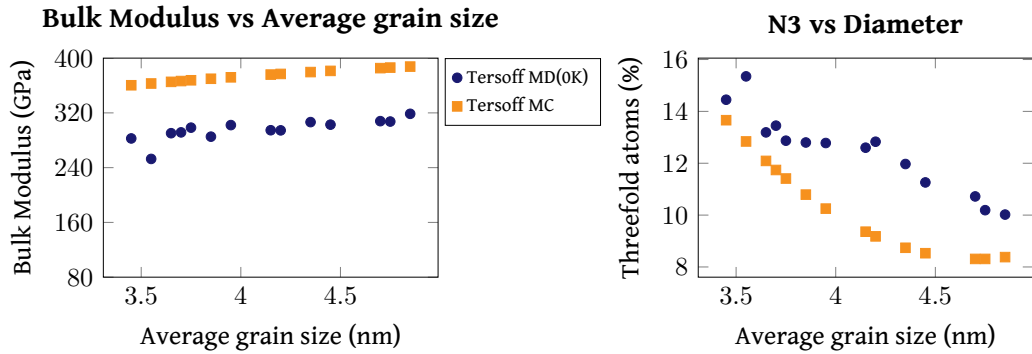


Fig. 3.31: Average grain size versus Bulk modulus for the UNCD samples at 0K and 300K, compared with the theoretical model [46]

whose bulk modulus is estimated using the REBO II[13] potential with Molecular Dynamics by Adiga et al. [45]. This is due to the higher percentage in threefold atoms, in comparison to the other two works, which leads in a softer structure and consequently in lower bulk modulus. As seen in fig. 3.31 samples with small average grain sizes are softer than those with big grain sizes.

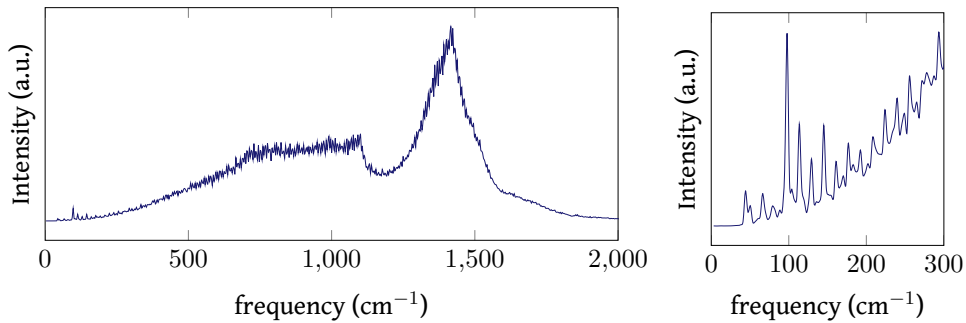


Fig. 3.32: VDOS of the typical UNCD sample at 300K

The vibrational density of states (VDOS) of a sample, shown in fig. 3.32 is presented next. The two characteristic peaks of diamond are visible at 1100cm^{-1} and 1400cm^{-1} . Also in the low frequency region a high activity area is observed. In the right panel of the same figure we can observe in detail what happens in that area. Even though the grains have random shape they are well defined structures for an estimation of the average grain size. The average grain size for this sample is 3.55nm . For this size we would expect a peak at around 100cm^{-1} . Instead, various peaks around that area are observed, which correspond to the actual grain sizes.

By taking the average frequency of these peaks we can compare our results with the theoretical prediction. In fig.3.33 the respective graph is presented. An interesting

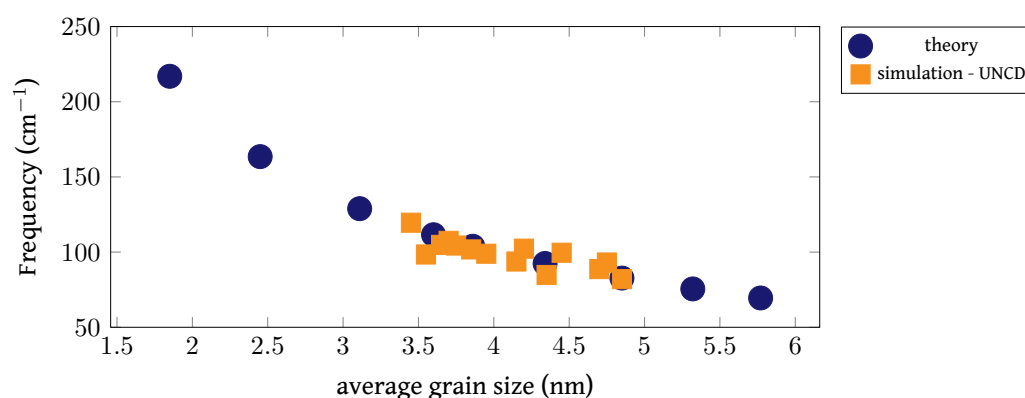


Fig. 3.33: Average grain size versus average frequency for the UNCD samples

correlation between the expected grain sizes and the average grain size obtain from the simulation is noted.

As a general note, when a grain is enclosed around a *thick* layer of amorphous atoms the corresponding frequency is quite prominent in the spectrum. If a particularly elongated grain is observed, two more intense peaks at frequencies corresponding to the width and the height of the grain are observed, this leads us to the conclusion that not only the size of a spherical nanocrystal can be estimated from the spectrum but also the size of *oval* shaped nanostructures. Also, in samples with average grain size less than 3.2nm we couldn't observe any excited peaks in the low frequency region. Which agrees with the conclusion in the previous section that embedded nanocrystals smaller than 3nm are not measured correctly.

3.2.6 H on 3D Carbon nanostructures

The presence of hydrogen in carbon nanostructures affects the structural and mechanical properties of carbon. Despite the fact the general acceptance that the hydrogen adsorption in metal hydrides is higher than that in carbon nanostructures, there is still an excessive interest in both areas since carbon based materials attract big interest because of their practical advantages, particularly their light weight.

Until recently theoretical studies, in an overwhelming majority, concern ideal nanostructures like nanotubes [47]. This is not only due to the innovative experiments that reported an excessive hydrogen adsorption that was attributed in nanotubes, but also to the fact that established computational techniques from first principles can not be used in the study of complex and disordered structures. Here we attempt to understand these changes.

The simulation of this part are performed with the Brenner interatomic potential as implemented in the open source software LAMMPS[10].

Free n-D with Hydrogen

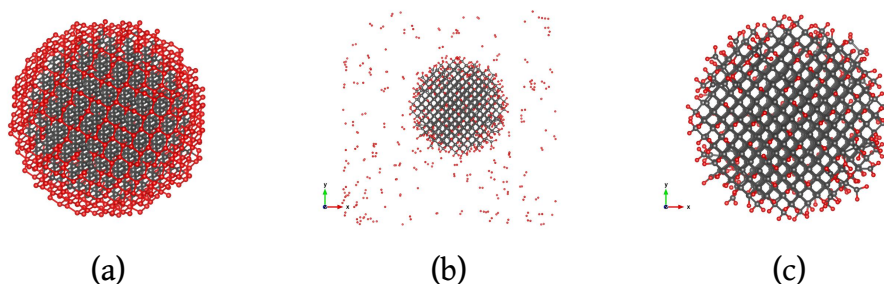


Fig. 3.34: Carbon free n-D with Hydrogen in three stages of the calculation; the initial configuration (left panel), the final configuration (central panel) and an image showing the H atoms bonded on the surface of the n-D (right panel)

The free-n-D in fig.3.34 is used to investigate the effect of hydrogen in vibrational spectrum is one that consists of 742 atoms of carbon. In the initial configuration, the number of hydrogen atoms in the surface of the n-D are 604. After annealing the system at 400K the hydrogen atoms remaining in the surface reduce to 302. The images corresponding to these three states of the simulation can be seen in fig.3.34.

From the vibrational spectrum of the Free n-D with Hydrogen we can see the characteristic peak of diamond at 1400cm^{-1} , the peak corresponding to the size of the n-D at 200cm^{-1} and the peak in the range of $2800 - 3000\text{cm}^{-1}$ associated with the vibration mode of methane (hydrogated sp^3). Also, as seen from fig. 3.35 the peak near zero is attributed to the free hydrogen atoms.

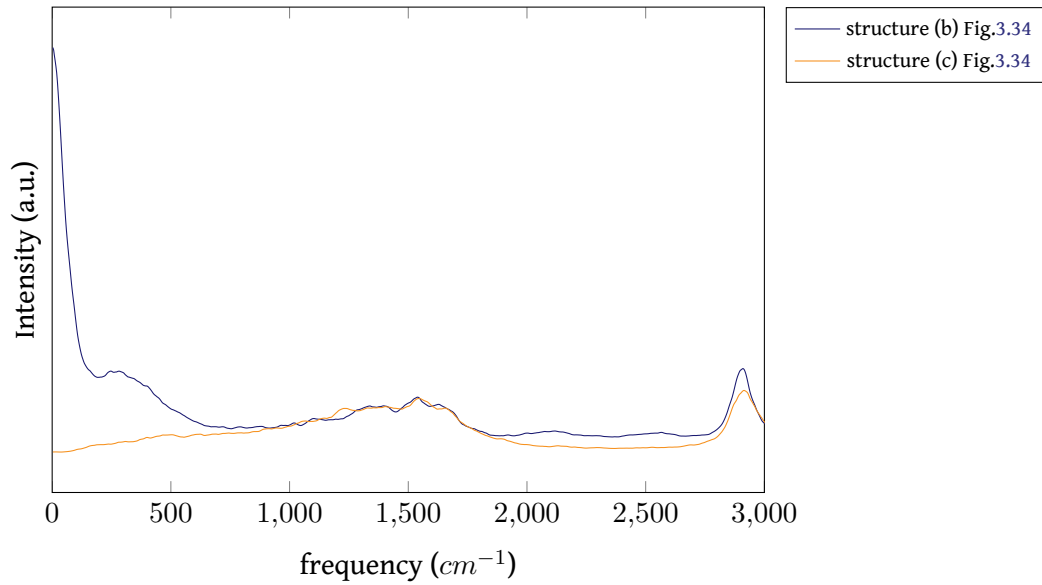


Fig. 3.35: Vibrational Spectrum of a Free-n-D with Hydrogen

H in amorphous carbon

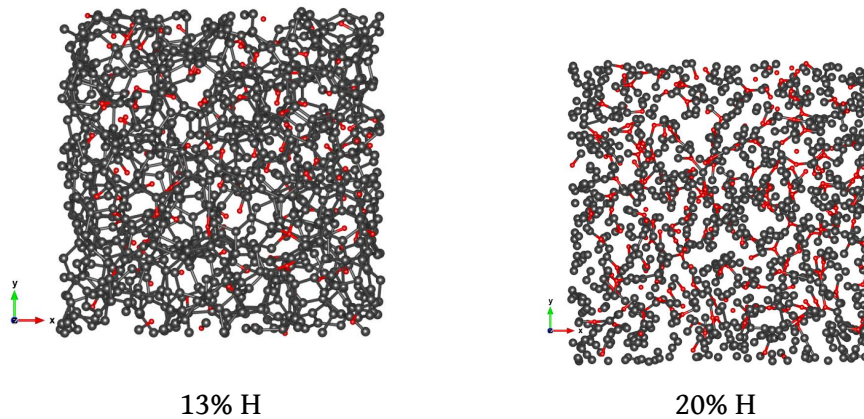


Fig. 3.36: a-C samples with 1000 atoms of carbon in two different concentration of H. The first with 150 and the second with 250 atoms of H

The a-C sample we present here has 3.25 gr/cm^3 final density, with 65.9% sp^3 atoms. The bulk modulus of the structure is calculated with the Tersoff potential at 337Gpa.

With the introduction of hydrogen in the structure the bulk modulus reduces to 182.85GPa for the structure with the 150 H atoms and at 118.55GPa for the structure with the 250 H atoms. Comparing with results obtained with Tight-binding MD[48] we see that our structure are much softer.

3.3 Conclusions

As a conclusion a comparison of all the different nanostructures studied is made. In fig. 3.37 we see the spectra of a 4.67nm free n-D structure, a n-D - a-C sample with a

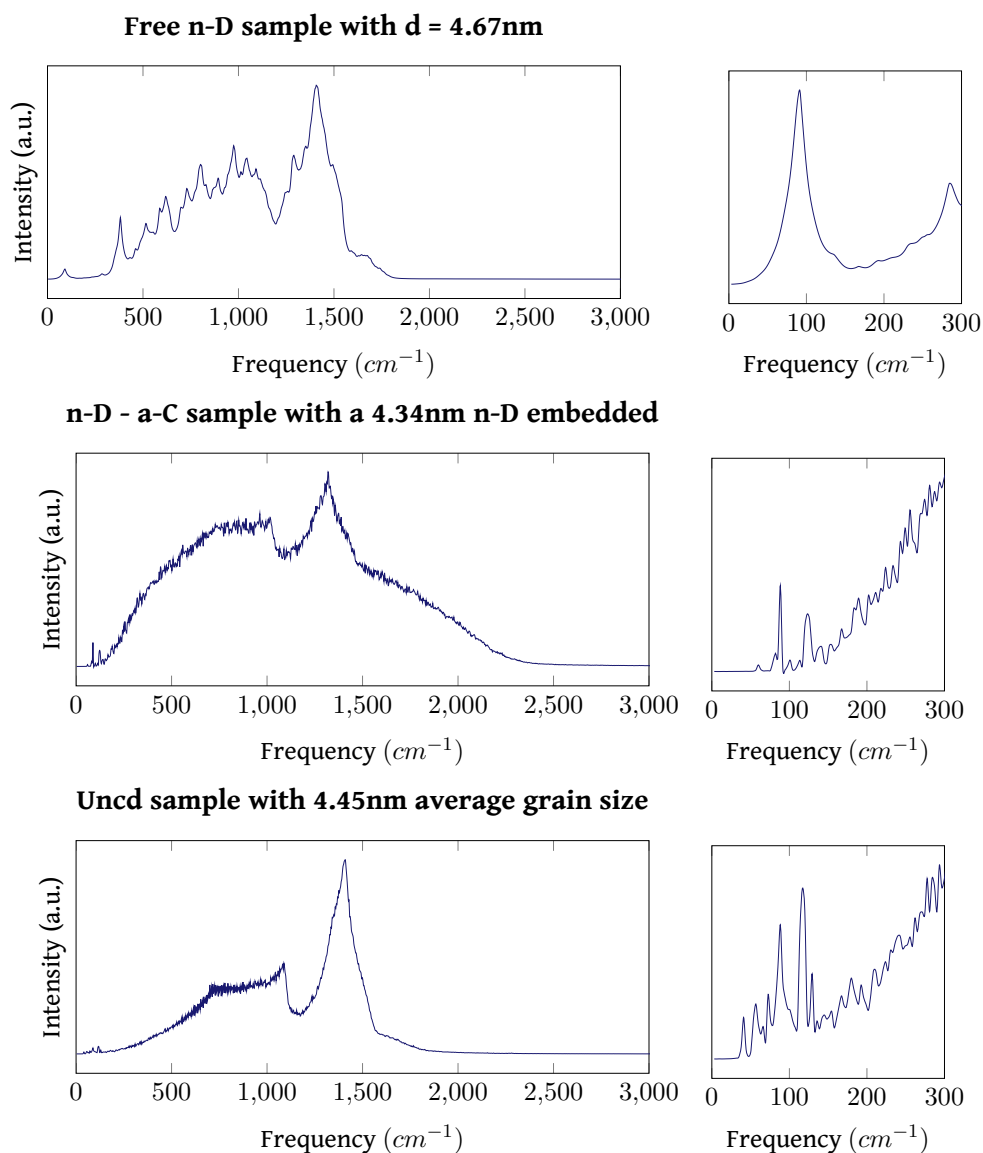


Fig. 3.37: Vibrational Density of states for an free n-D, n-D - a-C and a UNCD sample with similar nanocrystal and average grain sizes. The left panel we see the full three spectra, while on the right panel the respective low frequency regions of each spectrum

4.34nm n-D embedded and a UNCD sample with a 4.45nm average grain size. In all three spectra the associated with diamond peaks in 1400cm^{-1} and 1100cm^{-1} are present.

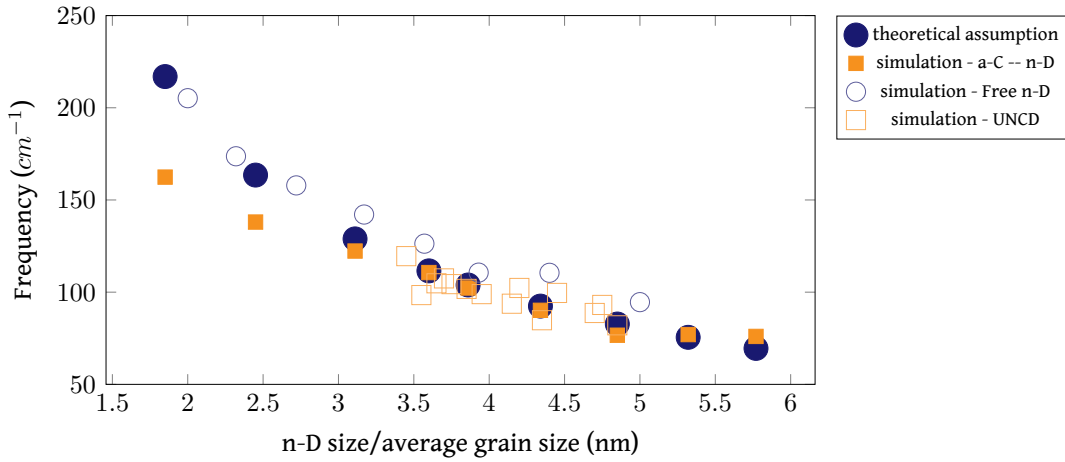


Fig. 3.38: Comparative image of the diameter of a nanocrystal or the average grain size of a UNCD sample with the frequency that corresponds to that size

The presence of amorphous carbon can also be detected from these images. The n-D - a-C sample with a higher percentage in amorphous atoms than the UNCD sample, displays two wide peaks around 800cm^{-1} and 1600cm^{-1} . These positions are connected with the D and G peaks of an a-C sample with the equivalent percentage in sp^2 atoms (50%). In contrast the UNCD sample with only 11% sp^2 atoms has an opposite behaviour in these areas.

Finally, the peaks in the low frequency region that correspond to the respective size are observed more clearly in the n-D - a-C samples where the shape of the nanocrystal is spherical rather than in the UNCD sample where the grains have random shape. Obviously, that peak is clear in the spectrum of the free n-D, but as we mentioned before they are isolated and that is expected. A quantitative comparison is presented in fig. 3.38. We see that for n-D sizes below 3nm the nanoparticle size is underestimated. For the UNCD samples as we saw before, the average grain size seems to agree well with the theoretical assumption.

Concluding, we can see that vibrational spectra analysis is a precise, non invasive way to characterize carbon samples with embedded nanocrystals.

Hydrogen Evolution edge-site activity of MoS₂ and hybrid MoS₂/Graphene structures

Recent studies have shown transition metal dichalcogenides (TMDs) are rising candidates in the replacement of Pt as catalysts in the water splitting process. In this study we focus on the hydrogen evolution reaction (HER) part of this process and how Hydrogen (H) interacts with the TMDs, specifically MoS₂, as a free standing nanostructure or when positioned on a graphene substrate. Our results are obtained through Density Functional Theory (DFT) calculations.

First we show the stability of the MoS₂ structures. We examine various nanostructures, from a 2D infinite MoS₂ monolayer to the quasi-1D MoS₂ ribbons and the quasi-0D MoS₂ flakes. Next, we calculate the adsorption of H on various sites of the TMD, including their Mo and S edges and their respective corners. We also evaluate the activity of each site.

Furthermore, the MoS₂/Graphene hybrid system is investigated for its stability. Additional calculations of the adsorption of H in the MoS₂/Graphene hybrid structure indicate that the effect of graphene in the adsorption process of H on MoS₂ nanostructures is quite significant.

4.1 Introduction

Recent developments in the *Hydrogen Economy* have increased the interest in Fuel Cells (FCs)(fig.4.1). FCs combine oxygen and hydrogen and produce energy with water as the byproduct making hydrogen an environment friendly, by current standards, fuel. Apart from the huge advantages in the use of FCs an unwelcoming downside is the increase of the FCs cost with the use of precious metals (mainly Pt) as catalysts during the water splitting process (eq. 4.1).

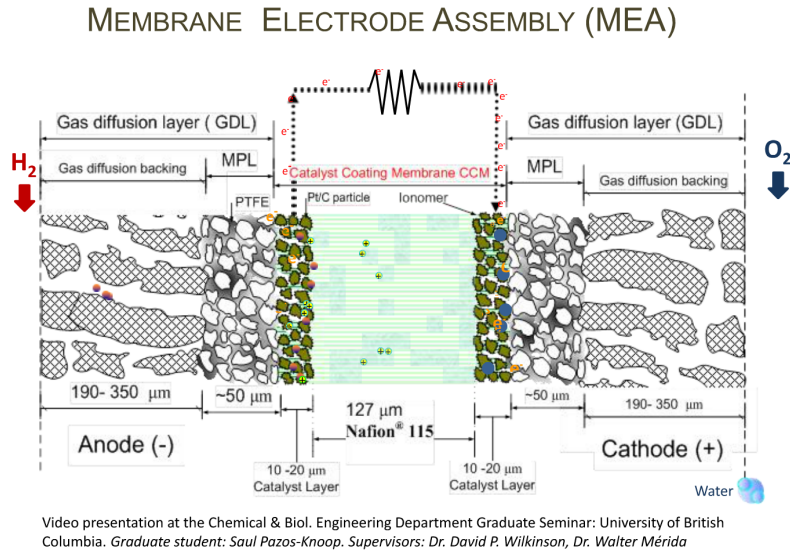
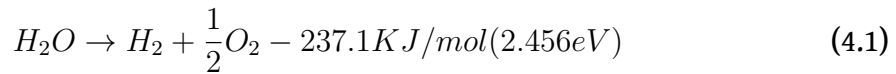
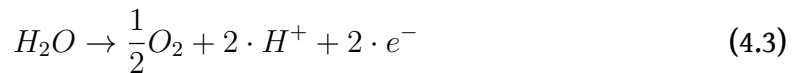


Fig. 4.1: Membrane Electrode Assembly(MEA) Fuel Cell. (Snapshot taken from video presentation [\[49\]](#) of S. Pazos-Knoop. University of British Columbia)



The two half reactions involved in the process are the Hydrogen Evolution Reaction (HER), shown in eq. 4.2 and the Oxygen Evolution Reaction (OER), shown in eq. 4.3.



For the adsorption and desorption of Hydrogen during the HER on the catalyst, three possible steps are considered [49]. The Volmer step, eq.4.4 refers to the adsorption part. Then, either the Heyrovsky step, eq.4.5 or the Tafel step, eq.4.6 can achieve desorption.



The success of this adsorbed-transition-desorbed process can be achieved with either the Volmer-Heyrovsky or the Volmer-Tafel mechanism. [The first is supposed to be the rate-limiting step for the electrochemical desorption [50]]

Up to now, the catalyst used in the HER, is mainly Pt. Despite the fact that Pt's efficiency is almost perfect, it's a very expensive and rare material. That is why alternative catalysts for the HER would be more practical and favorable.

For the evaluation of a material as a feasible catalyst in the HER, there are various quantitative ways [51]. One is by calculating the stability of the adsorbed H in a crystal, represented by the binding energy of the system (ΔE_H) and estimated from equation 4.7,

$$\Delta E_H = E_{tot}^{crystal+H} - E_{tot}^{crystal} - \frac{1}{2} \cdot E_{tot}^{H_2} \quad (4.7)$$

where $E_{tot}^{crystal+H}$ is the total energy of the system with the adsorbed H, $E_{tot}^{crystal}$ is the total energy of the system without the H and $E_{tot}^{H_2}$ is the total energy of the Hydrogen molecule.

Another quantity that can be used for the evaluation of a material is the Gibbs free energy difference (ΔG_H^o), which represents the possibility/probability of the process and which is estimated from equation 4.8

$$\Delta G_H^o = \Delta E_H + \Delta E_{ZPE} - T \cdot \Delta S_H^o \quad (4.8)$$

where ΔE_{ZPE} and ΔS_H^o are the zero point energy and the entropy respectively. These two terms used to be considered as a constant (0.24eV[52]), a more recent work by Seo et al.[53] has estimated that these two terms can fluctuate from 0.36eV to 0.49eV, while in the work done by Pandey et al. [54] they estimate that the zero-point energy difference (ΔE_{ZPE}) between the gas phase and the absorbed state is 0.12eV and the term of the equivalent entropy difference at standard conditions ($-T \cdot \Delta S$) is 0.20 eV. Resulting in a constant value for the $\Delta E_{ZPE} - T \cdot \Delta S$ part. Based on these, our indirect estimation of the Gibbs free energy is going to encase values where the last two terms of eq.4.8 fluctuate from 0.22eV to 0.49eV.

A functional catalyst's H binding energy should be big enough for it to be absorbed but small enough for the desorption to occur and should also have ΔG_H^o near zero, meaning that H shouldn't bind too strongly or too weakly.

It has already been shown [55], [52], that MoS₂ is a good candidate for the HER, especially the nanostructures with active edges (quasi-1D ribbons). The renewed attention to TMDs as catalysts in the hydrogen evolution reaction is due to the interesting properties recently observed in the edges of TMDs' particles[56], [57]. These recent developments clearly have considerable impact. In this work we are going to estimate the binding energy for hydrogen on top of an infinite 2D sheet of MoS₂, as well as various sites on an quasi-1D ribbon of MoS₂ and quasi-0D hexagonal and triangular flakes. We investigate both the Mo and the S edge of the structures as well as their respective corners. All these structures are also positioned on top of a graphene sheet.

4.2 Methodology

The calculations are carried out using the Vienna *Ab initio* Simulation Package (VASP) [58]- [61]. The projector augmented wave method (PAW) [62], [63], [64] with both the Perdew-Burke-Ernzerhof(PBE)[18] and the Local Density Approximation (LDA) [17] exchange-correlation functionals were used. After the convergence tests, we conclude to a 480eV E_{cutoff} for the plane waves and a Γ -centered 3x3x1 k-point mesh for the Brillouin Zone. Also for the geometric relaxation we use the conjugate-gradient approximation. All our systems are modeled with an at least 12Å vacuum in the out of plane direction.

4.3 Results and Discussion

4.3.1 Free Standing MoS₂ nanostructures

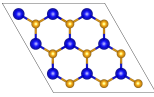
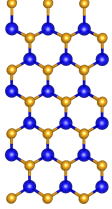
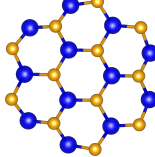
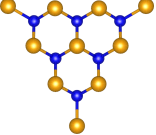
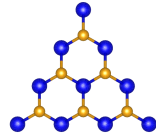
| Name | 2D MoS ₂ (1) | 1D Ribbon (2) | 0D Hex Flake (3) | 0D S - T Flake (4) | 0D Mo - T Flake (5) |
|-------------------------------|---|---|---|--|---|
| Images |  |  |  |  |  |
| E_{coh} eq.4.9 (eV/atom) | -7.78 | -7.38 | -7.03 | -6.31 | -7.50 |

Fig. 4.2: Free Standing MoS₂ structures. The Mo atoms are denoted with blue and the S with yellow. The x axis of these structure is along the lines to the right and the y axis is perpendicular to them

During this study we are going to use various MoS₂ nanostructures. In this section we demonstrate the shape and evaluate the stability of each of them. In fig. 4.2 we see all the MoS₂ structures we are going to examine alone or with the graphene substrate. The stability (E_{coh}) of each structure is calculated according to equation 4.9,

$$E_{coh} = E_{Mo_lS_m}^{tot} - l \cdot E_{Mo} - m \cdot E_S \quad (4.9)$$

where, $E_{Mo_lS_m}^{tot}$ is the total energy of the MoS₂ nanostructure l are the number of Mo atoms, m the number of S atoms and E_{Mo} and E_S is the total energy of the Molybdenum and the Sulfur atom respectively.

The stability of a single-layer MoS₂ structure, whose unit cell consists of one Molybdenum atom and two Sulfur atoms is calculated (eq. 4.9) at -7.84eV/atom. As shown

in fig. 4.2 the stability of a MoS₂ structure whose unit cell consists of 9 Mo and 18 S atoms is very close to the small unit cell at -7.78eV, inside the margin of error of the method.

Quasi-1D ribbons, systems already observed experimentally[65], are an interesting structure since they allow the exploration of their exposed edges. The ribbons we use are constructed as shown in the work done by Bollinger et al. [55]. We start with an orthogonal unit cell that consist of 2 Mo atoms and 4 S atom with 2 additional S atom that saturate the exposed Mo edge. With x repetitions in the x-direction and y repetitions in the y-direction we create each Rib _{x,y} ribbon. As far as their stability is concerned we can see that the ribbons with greater y are more stable (as shown in table A.7). Rib_{2,2} and Rib_{3,2} have E_{coh} -7.12 and -7.18 eV/atom respectively, whereas Rib_{2,3} and Rib_{3,3} have cohesive energy -7.38 eV/atom.

The hexagonal flake (Hex flake) we use consists of 12 Molybdenum atoms and 24 Sulfur atoms, retaining the stoichiometry of MoS₂. Its shape is a hexagon with consecutive Mo and S edges. While, the triangular flakes (T flakes) we use, can either be S-edge flake or Mo edge flakes. In fig. 4.2 we also see the two triangular flakes. The Mo terminated flake, has 10 Mo atoms and 12 S atoms, the stoichiometry of which is broken with Mo in excess (Tmo). Realistically, this configuration is difficult to exist in an experimental setup since the environment which can be rich in Sulfur and possibly Oxygen won't allow a highly, as we will see, active Mo edge to be available for H adsorption. On the other hand, the triangular flake has 6 Mo and 20 S atoms, resulting in excess in Sulfur(Ts).

When the stoichiometry is retained the triangular flakes instead of being equilateral are isosceles (T), on one of the sides of the triangular flake Mo or S will have to be added to complete the stoichiometric analogy. In this case, two sides will be similarly terminated with the third having the opposite termination, either S or Mo. For this work, we examine one triangular flake with a 4x4x4 S edge (F₂₆Ts) and one with a 4x4x4 Mo edge (F₂₂Tmo) as shown in fig. 4.2.

As far as their stability is concerned, we see that the quasi-0D structures with the Mo edges are the most stable(F22Tmo has -7.50eV/atom). Less stable, but more stable than the structure with S excess (F30Hex has -5.54eV/atom cohesive energy) are the structures whose stoichiometry is retained (F9Hex has -6.46eV/atom and F36Hex has -6.31eV/atom cohesive energy). Additional information about the structures not shown in fig. 4.2 can be found in tab. A.7.

4.3.2 MoS₂ on Graphene

The hybrid MoS₂/Graphene system has attracted interest not only on a theoretical level [66], [67], [68], but also in very interesting experimental set ups [69], [70], [71], [72] where the hybrid system is used for catalysis [50], storage purposes [73] and other applications [74]. MoS₂ and Graphene interact with van der Waals forces. Usually the interlayer distance in hybrid systems with Graphene is in the range of 0.3-1.0nm[75]. Specifically for MoS₂ the distance between the two layers, d_{C-S} , distance between the C layer and the nearest to it S layer is close to 0.34nm[76].

The stability of these structures is assessed through eq. 4.10,

$$E_B = E_{tot}^{XY-hybrid} - E_{tot}^{X-str} - E_{tot}^{Y-str} \quad (4.10)$$

where, E_B is the binding energy of the structure, $E_{tot}^{XY-hybrid}$ is the total energy of the MoS₂/graphene structure, E_{tot}^{X-str} is the total energy of the MoS₂ structure and E_{tot}^{Y-str} is the total energy of the graphene sheet.

2D infinite sheet

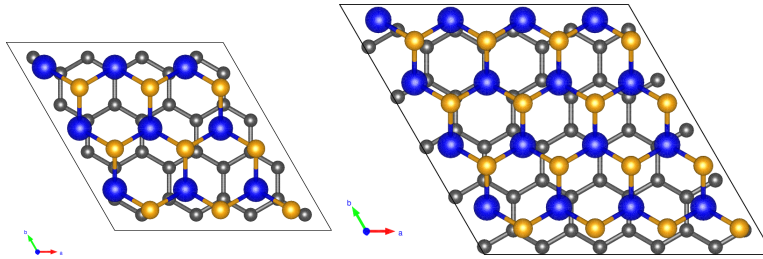


Fig. 4.3: C₃₂Mo₉S₁₈ and C₅₀Mo₁₆S₃₂ structures, Carbon, Molybdenum and Sulfur atoms are denoted with gray, blue and yellow color respectively. The x axis is along the vector \vec{a} of the unit cell as shown in the images and z axis is vertical to the page

We use two different hexagonal unit cells for this structure shown in fig.4.3. The first is a 4x4 super-cell of graphene (C₃₂) with a 3x3 super-cell of MoS₂. The structure consists of 32 atoms of Carbon, 9 atoms of Mo and 18 atoms of S (C₃₂Mo₉S₁₈ structure). The second structure is a 5x5 graphene super-cell(C₃₂) with a 4x4 MoS₂ super-cell. The structure consists of 50 atoms of Carbon, 16 of Mo and 32 of S (C₅₀Mo₁₆S₃₂ structure). For the 2D MoS₂ infinite sheet on graphene two possible configurations are proposed[68]. The TS configuration where a S atoms is directly on top of a C atom and the TM configuration with a Mo atom is positioned on top of a C atom. We examine both configurations with both LDA and GGA-PBE exchange correlation functionals. In table 4.1 we see the relaxation results of the C₃₂Mo₉S₁₈ structure in both configu-

| $C_{32}Mo_9S_{18}$ | Free Standing Structures | TS_{PBE} | TM_{PBE} | TS_{LDA} | TM_{LDA} |
|--------------------------------|--------------------------|------------|------------|------------|------------|
| C - C | 1.42Å | 1.41Å | 1.41Å | 1.41Å | 1.40Å |
| $\hat{C}\hat{C}\hat{C}$ | 120.0° | 120.01° | 119.82° | 119.94° | 120.04° |
| Mo - S | 2.43Å | 2.43Å | 2.43Å | 2.41Å | 2.40Å |
| S - S | 3.15Å | 3.07Å | 3.07Å | 3.01Å | 3.04Å |
| $\hat{S}\hat{M}\hat{o}\hat{S}$ | 81.07° | 78.40° | 78.39° | 77.24° | 78.41° |
| d_{C-S} | — | 4.34Å | 4.33Å | 4.46Å | 3.30Å |
| Strain MoS_2 | | +1.98% | +2.09% | +4.70% | -1.33 % |
| Strain Graphene | | -1.01% | -0.91% | 0% | +3.31 % |
| a'_{PBE} | 9.59/9.88 | 9.78 | 9.79 | | |
| a'_{LDA} | 9.36/9.80 | | | 9.80 | 9.67 |
| E_B (eV) | | -0.21 | -0.25 | -0.17 | -1.15 |

Table 4.1: $C_{32}Mo_9S_{18}$ relaxation results, using PBE and LDA potentials in TS TM configuration

rations with both exchange correlation functionals. The lattice constant mentioned, refers to the supercell. The lattice constants of MoS_2 are 3.20Å and 3.12Å with GGA-PBE and LDA respectively. For graphene the respective values are 2.47Å and 2.45Å. What is observed is that despite the good representation of the structure with the PBE functional as far as the in plane parameters are concerned, the out-of-plane distance d_{C-S} is described correctly only with the LDA functional in the TM configuration. For the

| $C_{50}Mo_{16}S_{32}$ | Free Standing Structures | TS_{PBE} | TM_{PBE} | TS_{LDA} | TM_{LDA} |
|--------------------------------|--------------------------|------------|------------|------------|------------|
| C - C | 1.42Å | 1.44Å | 1.4248Å | 1.42Å | 1.44Å |
| $\hat{C}\hat{C}\hat{C}$ | 120.0° | 120.34° | 119.9374° | 119.86° | 119.93° |
| Mo - S | 2.43Å | 2.34Å | 2.3753Å | 2.37Å | 2.37Å |
| S - S | 3.15Å | 3.17Å | 3.1459Å | 3.14Å | 3.14Å |
| $\hat{S}\hat{M}\hat{o}\hat{S}$ | 81.07° | 82.83° | 82.9370° | 82.94° | 82.93° |
| d_{C-S} | — | 4.22Å | 3.32Å | 3.32Å | 3.32Å |
| Strain Graphene | | +0.89% | -0.24% | 0.49% | 0.56% |
| Strain MoS_2 | | -2.50% | -3.60% | -1.36% | -1.29% |
| a_{PBE} (Å) | 12.35/12.78 | 12.46 | 12.32 | | |
| a_{LDA} (Å) | 12.25/12.48 | | | 12.31 | 12.32 |
| E_B (eV) | | -0.55 | -0.38 | -3.62 | -3.65 |

Table 4.2: $C_{50}Mo_{16}S_{32}$ relaxation results, using PBE and LDA potentials in TS TM configuration

bigger structure ($C_{50}Mo_{16}S_{32}$) we see that the out-of-plane parameter d_{C-S} is described correctly in the TM configurations (for both LDA and PBE) and in the TS configuration with LDA (shown in table 4.2). What is interesting to see is the strain each configura-

tion results in. We see that with PBE the strain the MoS₂ structure undergoes is bigger than with the LDA functional. The structure with the minimum strain is the TM configuration with LDA. Our results agree well with previous calculations, where the d_{C-S} distance is calculated in at 3.32Å[68] and 3.35Å[66], and is experimentally measured at around 3.4Å[76]. Consequently, from here on we use the TM configuration with the LDA functional for further analysis, which seems to be preferable for transition metal dichalcogenides hetero-structures[77].

In fig.4.4 we see the band structure of the hybrid Graphene/MoS₂ system in the big supercell configuration.

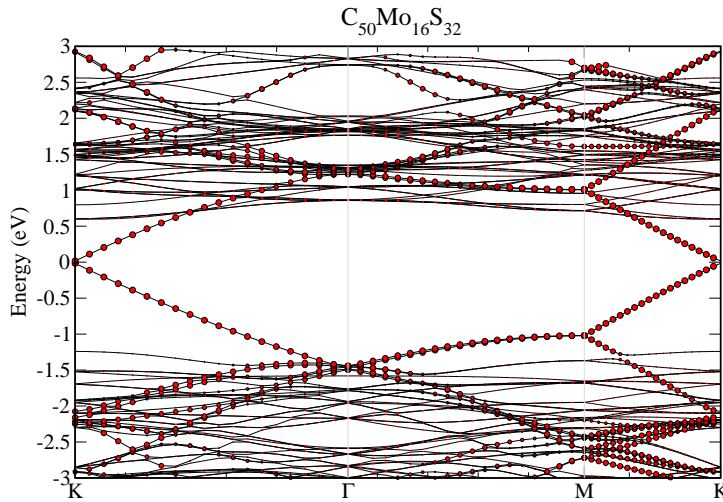


Fig. 4.4: Electronic band structure in the $K - \Gamma - M - K$ path of the Brillouin Zone of the $C_{50}Mo_{16}S_{32}$ structure. The red points correspond to the contribution of graphene

The direct gap at K-point is 0.037eV for graphene, in agreement with previous calculations [68], [77] and for MoS₂ is 1.84eV, pointing to small compressive strains, according to the analysis of the next chapter and verified by the structural analysis of table4.2.

The stability of these two structures is examined through eq.4.10. As shown in table A.7, $C_{50}Mo_{16}S_{32}$, with the smaller graphene strain, is more stable than $C_{32}Mo_9S_{18}$.

1D ribbons

As mentioned before, the ribbons we study have a saturated with dimers of Sulfur Mo-edge, the two different unit cells shown in figure 4.5, differ in the size of the substrate, while the MoS₂ ribbon is the Rib_{3,3}. The width of the ribbon is important for tuning various of its properties, but as shown [78] the effects of its edge are retained

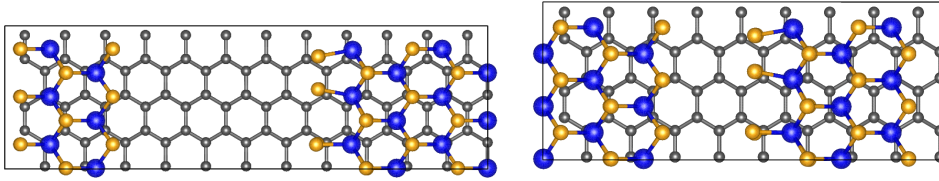


Fig. 4.5: Rib_{3,3} on top of C₇₂ and C₉₆ graphene substrate. Carbon, Molybdenum and Sulfur atoms are denoted with gray, blue and yellow color respectively, the y axis is parallel to the text lines and the x axis vertical to them

even with the width change. The ribbon we use has three y repetitions of the arm-chair edge unit cell. The ribbon is also repeated in the zig zag edge (S-edge) direction three times (x repetitions) in order to match the size of the orthogonal unit cell of the graphene substrate. So, the MoS₂ (Rib_{3,3}) ribbon has 18 Mo atoms and 36 S with 6 extra Sulfur atoms that saturate the Mo edge.

The size of Rib_{3,3} unit cell is 9.29Å in the x-direction and 28.68Å in the y-direction (the distance from edge to edge is 16.61Å and the vacuum between the edges is 12.07Å). The orthogonal graphene unit cells we use consists of 72 and 96 atoms of Carbon. Its initial dimensions are; 8.54Å in the x-direction and 22.2Å and 29.6Å in the y-direction for the C₇₂ and the C₉₆ graphene substrate respectively. The initial lattice mismatch in the x direction is 8.1% and in the y direction the ribbon should be "compressed" when positioned in the C₇₂ graphene substrate. The y- direction vacuum is reduced to 5.6Å instead of 12.07Å. When the ribbon is positioned in the C₉₆ graphene substrate the ribbon has 7.4Å of extra vacuum in the y direction. In the final configuration, the C₇₂ substrate is strained by -1.26% in the y direction and 1.76% in the x direction with a 5.00Å vacuum between the edges. On the other hand, the C₉₆ substrate is strained by -1.25% in the y direction and by 1.33% in the x direction with the distance between the saturated Mo edge and the S edge at 12.42Å. The strain the ribbon undergoes is -6.45% in the C₇₂ substrate and -6.85% in the C₉₆ substrate in the x-direction.

By comparing C₉₆Rib_{3,3} and C₇₂Rib_{3,3} we see that the more stable structure is the one with the ribbon edges further apart, a fact which is verified when we position a ribbon with smaller width on a C₉₆ graphene substrate (C₉₆Rib_{2,3} structure).

0D Flakes

Even though ribbons with their infinite edges let us exploit the edge effects to the maximum, finite-size flakes present the opportunity to study possible effects of the MoS₂ corners.

We are going to use two different shapes for these quasi-0D structures. One with

hexagonal shape and one with triangular. Each shape can be either stoichiometrically correct, with an analogy of 2 S atoms per Mo atom, or have an excess of either Mo or S. Both shapes have already been observed experimentally [55], [80], [81], [79]. In order to achieve realistic results in the hybrid system of graphene and the quasi-1D flake of MoS₂, we first study the orientation between the two structures. In figure

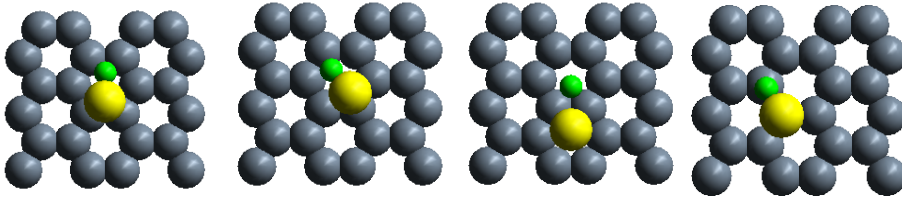


Fig. 4.6: Various MoS₂ molecule orientations on a orthogonal C₂₄ graphene substrate. The gray colored atoms denote Carbon atoms, the yellow Sulfur atoms and the green the Molybdenum atoms

4.6 we present the orientations of a single MoS₂ molecule in respect to Carbon atoms of the graphene substrate that are examined. In the first two orientations, the MoS₂ molecule is positioned in the center of the graphene hexagon, the first one along two opposite sides and the second along two opposite corners. The third orientation has the MoS₂ molecule perpendicularly on top of a C-C bond and in the final orientation the molecule is positioned on top and in parallel to a C-C bond. The binding energy of the structures is calculated through eq. 4.10 at -0.58, -0.58, -0.59 and 0.23 eV/atom for each of the orientations respectively. This means that some orientations are more preferable than others.

[In the work done by Huang et al. [82] they obtain a monolayer of MoS₂ by using a controllable etching process. PL and Raman spectroscopy results between exfoliated samples of monolayer MoS₂ and samples treated with the etching technique are in good comparison.]

The hexagonal flake (Hex flake) we use consists of 12 Molybdenum atoms and 24 Sulfur atoms, retaining the stoichiometry of MoS₂. The shape is a hexagon with consecutive Mo and S edges. We maintain the TM configuration, where a Molybdenum atom is aligned with a Carbon atom and position the flake on a rectangular graphene sheet of 96 carbon atoms, as shown in figure 4.9.

The flake is rotated counterclockwise by 20°, 40°, 60°, 80°, 100° and 120° degrees around the Mo-C axis of the TM configuration. Structures with 0° and 120° rotation can be considered equivalent, a fact which is verified by the results with the only noticeable change between them is in the d_{C-S} distance a difference of 0.01Å in graph 4.7 we plot the total energy of the structure versus the rotation angle of the MoS₂ flake. Also all the relaxation details can be seen in table 4.3. It can be seen that the structure with the

| | 2D MoS ₂ | 0° | *20° | 40° | *60° | 80° | 100° | 120° |
|--------------------------------|---------------------|---------|--------|---------|---------|---------|---------|---------|
| C - C | 1.42Å | 1.41Å | 1.41Å | 1.41Å | 1.41Å | 1.41Å | 1.41Å | 1.41Å |
| $\hat{C}\hat{C}\hat{C}$ | 120.0° | 119.90° | 119.8° | 119.62° | 119.96° | 119.93° | 120.32° | 119.85° |
| d_{C-S} | — | ~3.33Å | ~3.30Å | ~3.19Å | ~3.25Å | ~3.35Å | ~3.30Å | ~3.34Å |
| Mo - S | 2.43Å | ~2.38Å | ~2.31Å | ~2.38Å | ~2.37Å | ~2.38Å | ~2.37Å | ~2.39Å |
| S - S | 3.15Å | ~3.02Å | ~3.04Å | ~3.03Å | ~3.03Å | ~3.02Å | ~3.02Å | ~3.01Å |
| $\hat{S}\hat{M}\hat{o}\hat{S}$ | 81.07° | 78.88° | 81.99° | 79.23° | 79.12° | 79.06° | 79.11° | 78.89° |

Table 4.3: Relaxation results of the different orientations of the F₃6Hex flake on top of the C₉₆ graphene substrate

lowest energy is the one with the counterclockwise rotation of the flake by 40°, where $d_{C-S} = 3.19$. We must also note that the difference in the total energy between the structures is 14 meV which can be considered almost negligible. Nevertheless, we use this configuration for our further studies of this hybrid system. The resulting strain of

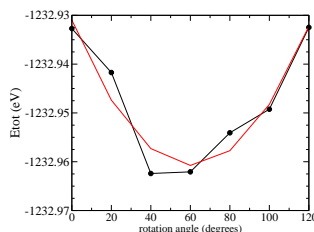


Fig. 4.7: Total energy (eV) of the hexagonal MoS₂ flake rotated around the C - Mo axis of the TM configuration, denoted with the black curve

the graphene substrate is less than the two previous configurations (with the 2D MoS₂ and the quasi-1D Rib_{3,3}) with -0.75% strain in x-direction and -0.91% in the y-direction. The binding energy of the structure is -1.26eV which shows that this structure is a bit more stable than the hybrid structure with the infinite MoS₂ sheet in the small configuration. The main difference is the strain the two components of the hybrid system undergo. Also the MoS₂ flake seems to be coming closer to the graphene substrate by at most 0.1Å. By observing the flake more closely, we see that it shrinks in favor of the substrate. Especially in the edges of the flake the distance of the Sulfur atoms (S-S) reduces to 3.04Å and the Mo-S distance to 2.36Å. This *compression* of the flake seems to be more prominent at the edges. The triangular flake (T flakes) we use are the ones described in the previous section. All three quasi-0D flakes positioned on the graphene substrate are shown in fig.4.8. Details on the stability of the MoS₂/Graphene systems can be found in table A.7 Comparing the quasi-0D structures we can see that the hexagonal flake is the more stable structure with the Mo-edge flake close to zero stability. We also see that the quasi-1D ribbons that undergo higher strain are not stable. From the two configurations with the 2D MoS₂ we see that the bigger one is more sta-

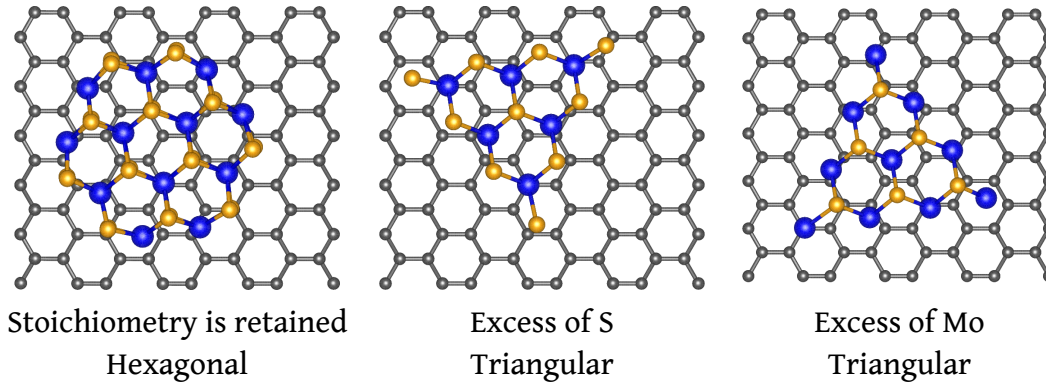


Fig. 4.8: Quasi-0D structures (Hexagonal and triangular) on a C₉₆ graphene substrate. Carbon, Molybdenum and Sulfur atoms are denoted with gray, blue and yellow color respectively

ble. This increase in stability seems to depend on the strain the two structures of the hybrid system undergo.

From the structures examined (see table A.7) here we see that the stability of the MoS₂/Graphene structure is not a straightforward issue. It seems to depend on several parameters, such as stoichiometry, strain and dimensionality.

4.3.3 H with MoS₂

In this section we present the results of the adsorption of H on MoS₂ structures. The structures we consider are the MoS₂ structures mentioned in the previous subsection. The adsorption sites of Hydrogen(s), where H is positioned on top or below the sulfur atoms of the edges, have been examined by Bollinger et al. [55] concerning the MoS₂ (2,6) ribbon structure, since their ribbon has a smaller, in width, edge, our results cannot be quantitatively compared, but as a general observation we see that the activity of the edge sites of an MoS₂ ribbon depends on the concentrations of both the Sulfurs and the Hydrogens at the edge.

Here we examine the stability and activity of the sites, where H is initially in the level of the Mo plane, in between the four neighboring sulfurs. In our final configurations, the hydrogen atoms move from the center of the square, created by the edge Sulfurs, to the side at the edge of a Sulfur layer. A similar resulting configuration is also observed in the structures examined by Bollinger et al. [55] although the ratio of Sulfurs and Hydrogens is higher.

The adsorption energies in the table of fig.4.4 are calculated using equation 4.11,

$$\Delta E_{ads} = E_{tot}^{crystal+n \cdot H} - E_{tot}^{crystal} - \frac{n}{2} \cdot E_{tot}^{H_2} \quad (4.11)$$

| | structure | ΔE_{ad} (eV) eq.4.11 |
|----|---|------------------------------|
| 2D | MoS ₂ H _{p0} | 1.66 |
| | Mo ₉ S ₁₆ H _{p0} | 1.17 |
| 1D | Rib _{2,3} H _{p0} | 0.57 |
| | Rib _{3,3} H _{p1} | -0.25 |
| | Rib _{3,3} H _{p3} | -0.14 |
| | Rib _{3,3} H _{p2+p3} | 0.20 |
| 0D | F ₃₀ HexH _{p0} | 0.37 |
| | F ₃₆ HexH _{p0} | 0.41 |
| | F ₃₆ HexH _{p5} | -0.12 |
| | F ₃₆ HexH _{p6} | -1.36 |
| | F ₃₆ HexH _{p5+p6} | -1.42 |
| | F ₃₆ HexH ₆ | -4.04 |

Table 4.4: Adsorption energies of Hydrogen on MoS₂ structures

where, ΔE_{ads} is the adsorption energy of H in the equivalent structure, n is the number of Hydrogen atoms adsorbed in the structure and $E_{tot}^{crystal+n \cdot H}$, $E_{tot}^{crystal}$ and $E_{tot}^{H_2}$ are the total energies of the structure with the Hydrogen(s), of the structure without the Hydrogen and of the H₂ molecule respectively.

As we can see, Hydrogen cannot bind on a basal site ($p0$) of the MoS₂ structure. The hexagonal flake we study, as shown in figure 4.9, has three S-edges($p5$) and three Mo-edges($p6$) that remain unsaturated. From the results of table 4.4 we conclude that the H adsorption site in the Mo-edge is more stable than the site in the S-edge. When we position the H atom on site $p7$ as shown in fig.4.9 after the relaxation of the structure the H has moved to the $p6$ position.

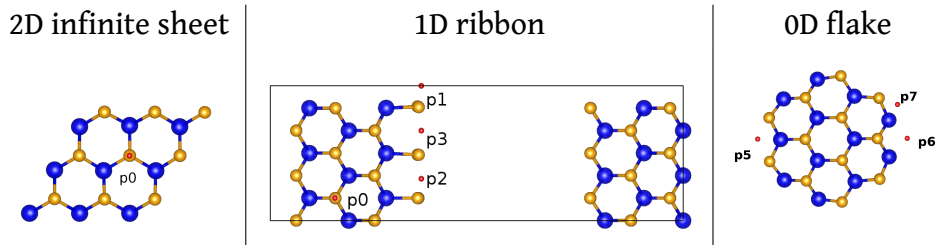


Fig. 4.9: MoS₂ structures indicating the initial Hydrogen sites. Molybdenum, Sulfur and Hydrogen atoms are denoted with blue, yellow and red respectively

If we try to add a second Hydrogen in the F₃₆Hex on the S-edge, when one has already been adsorbed in the Mo-edge, the binding energy of the structure is -0.06 eV. This means that the probability for a second Hydrogen to stably bond to the structure

is low. On the other hand, the adsorption energy of a second Hydrogen in Mo-edge of the F₃₆Hex flake, when the first has bonded in the S-edge is -1.30 eV, further proving the high activity of the Mo-edge.

4.3.4 H - MoS₂ Graphene

Next, we add Hydrogen in the hybrid system of MoS₂/Graphene. The positions we examine are the edge sites of the structures mentioned before. The four possible sites on the 1D ribbon coincide with the sites of H in the free standing ribbon. Positions *p1*, *p2* and *p3* are sites in between the Sulfur dimers that saturate the Mo-edge. The only obvious differentiation between these three positions is the relevant position of the Sulfur dimers in respect to the graphene substrate, where *p2* is on top of the center of a graphene hexagon, *p3* on top of a C-C bond and *p1* on top of a C atom. Site *p4* is initially in between the MoS₂ structure and the graphene substrate below the *p2* site.

For both the hexagonal and triangular flakes the positions of H are in the plane of the Mo layer either in a Mo- or a S- edge.

| structure | ΔE_H (eV/H atom) (eqs.4.7) |
|---|------------------------------------|
| C ₇₂ Rib _{3,3} H _{p2+p3} | -0.17 |
| C ₇₂ Rib _{3,3} H _{p2} | -0.31 |
| C ₇₂ Rib _{3,3} H _{p3} | -0.60 |
| C ₇₂ Rib _{3,3} H _{p4} | -0.89 |
| C ₉₆ Rib _{3,3} H _{p3} | -0.72 |
| C ₉₆ F ₃₆ H _{mo-edge} | -1.34 |
| C ₉₆ F ₃₆ H _{s-edge} | -0.09 |

Table 4.5: Adsorption energies of H on the hybrid system of MoS₂/Graphene

As far as the adsorption of H on MoS₂ ribbon positioned on a graphene substrate is concerned we can see that Hydrogens in the sites *p2* and *p3*, which are equal if we consider only their position in relevance to the MoS₂ ribbon, have quite different adsorption energies. The adsorption of H in *p2* is -0.31 eV, whereas in *p3* is -0.60 eV. By considering the substrate, where *p2* is on top of a C-C bond and *p3* is almost on top of a Carbon atom, we conclude that graphene significantly affects the adsorption of Hydrogen(s). If we try to position a Hydrogen closer to the graphene substrate (*p4*) we see that it binds stronger with an -0.89 eV adsorption energy. All final configurations of the ribbon can be seen in fig. 4.10.

We increase the distance between the two edges of the ribbon, by taking a bigger cell for the graphene substrate and by comparing the adsorption energies of the same

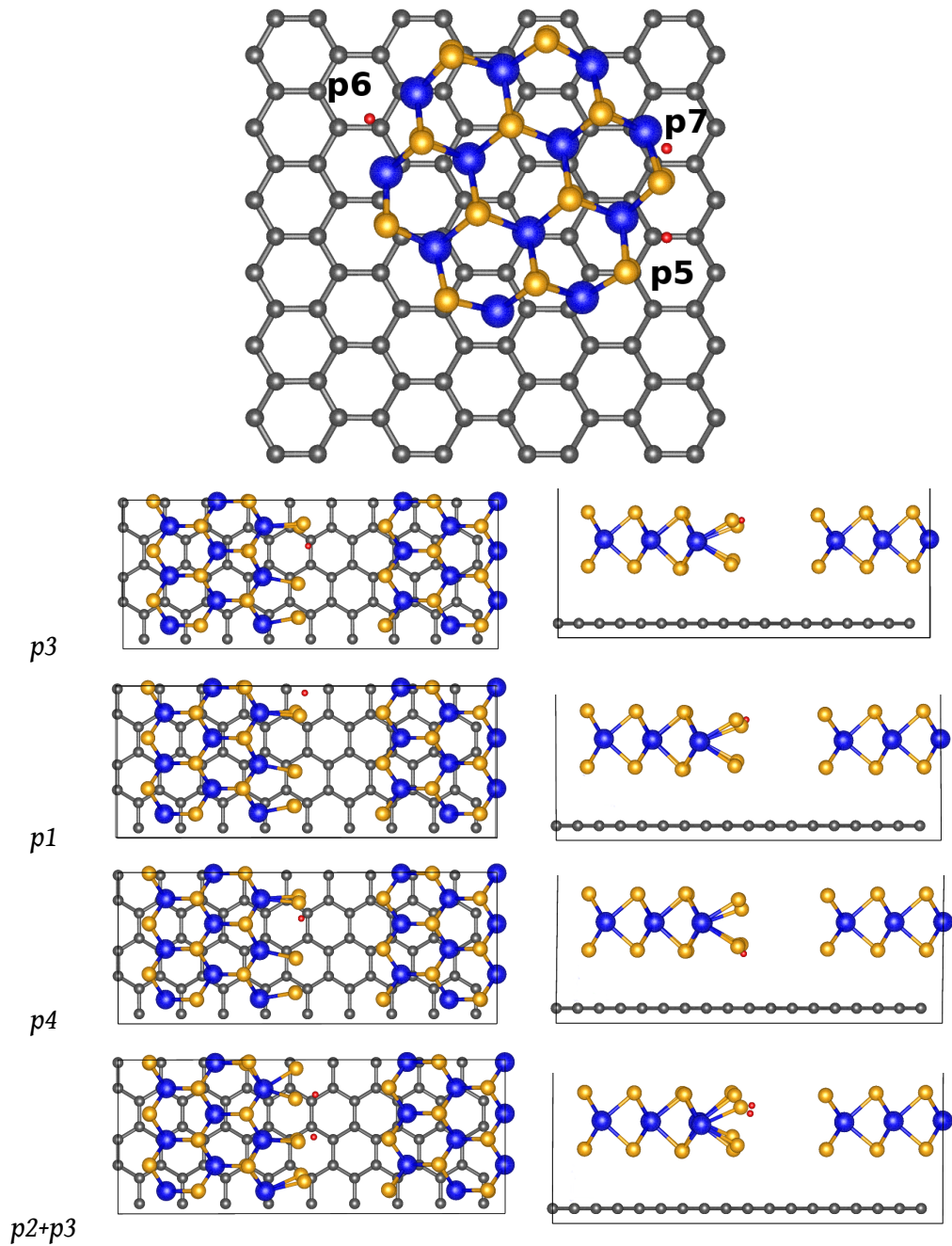


Fig. 4.10: Final configurations of Hydrogen in the Graphene/MoS₂ system. Carbon, Molybdenum, Sulfur and Hydrogen atoms are denoted with grey, blue, yellow and red respectively

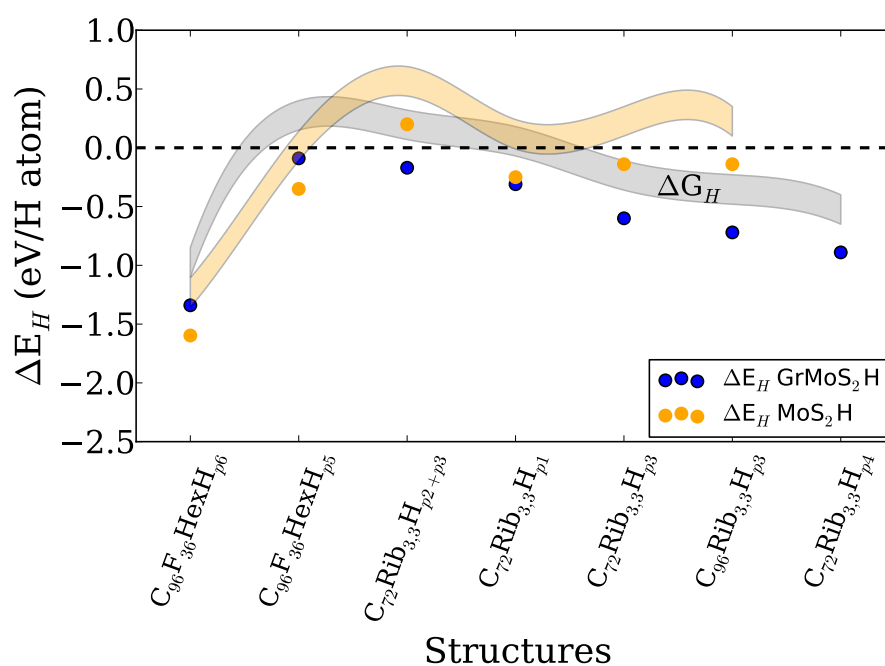


Fig. 4.11: Graph of the adsorption energy of H on a hybrid Graphene/MoS₂ structure (denoted with blue dots) and the possible area of the Gibbs free energy change ΔG_H (gray area). The minimum of the area is calculated with the value of 0.24 eV [52] for the $\Delta E_{ZPE} - T \cdot \Delta S$ of the ΔG_H and the maximum with the 0.49 eV [53] value.

site ($p3$), that is on top of a C-C bond, we see that the adsorption energy increases from -0.60 eV (C_{72} substrate) to -0.72 eV (C_{96} substrate). In the *small* graphene substrate the distance between the Sulfur dimers of the S-edge and the ones that saturate the Mo-edge is 5.00\AA , whereas the distance for the *big* graphene substrate is 12.42\AA .

Two Hydrogen atoms in sites $p2$ and $p3$ seem to bind too weakly at -0.17 eV. If we contemplate what happens when one Hydrogen is already adsorbed in $p2$ and a second Hydrogen gets adsorbed in $p1$ then the adsorption energy of the second hydrogen is 0.14 eV meaning that the adsorption of the second Hydrogen is not favored energetically.

For the evaluation of the $F_{36}\text{Hex}$ as the MoS_2 structure on the graphene substrate, we consider two possible sites for the adsorption of Hydrogen on MoS_2 . Both positions are in the level of the Molybdenum layer. One is on the side of the Sulfur dimmers ($p5$) and the other on the side of the Molybdenum atoms ($p6$). The adsorption energy on the S-edge is -0.09 eV and on the Mo-edge is -1.34 eV. This shows that the binding on the Mo edge is too strong and not helpful in the HER. All these results can be seen in table 4.5.

4.4 Conclusions

Concluding, as far as the free standing MoS_2 is concerned, we observe that higher MoS_2 dimensionality increases the structural stability with an exception in the Mo-edge triangular flake which achieves the highest stability. When MoS_2 is positioned on the graphene substrate this pattern is reversed, with MoS_2 structures with lower dimensionality being more stable with a clear exception again in the Mo-edge flake which shrivels and loses its stability. Also we must note that due to the lattice mismatch with graphene, the MoS_2 structure on top of it gets compressed. As shown in fig.4.11 the stability of H increases when the graphene substrate is present. A clear indication of the importance of the substrate is the different effect it has in the $p1$ and $p3$ sites whose main difference is the relevant position in regards to the substrate. Also the distance between the edges seems to slightly influence the adsorption of H. From this diagram we also conclude that the optimum edge sites are on the 1D ribbon and the 0D S-edge of the flake.

Electronic Properties Engineering of TMDs: strained monolayer

We present Density Functional Theory (DFT) results for the electronic and dielectric properties of single-layer (2D) semiconducting transition metal dichalcogenides MX_2 ($M = Mo, W$; $X = S, Se, Te$) under isotropic, uniaxial (along the zigzag and armchair directions), and shear strain. Electronic band gaps decrease while dielectric constants increase for heavier chalcogens X . The direct gaps of equilibrium structures often become indirect under certain types of strain, depending on the material. The effects of strain and of broken symmetry on the band structure are discussed. Gaps reach maximum values at small compressive strains or in equilibrium, and decrease with larger strains. In-plane dielectric constants generally increase with strain, reaching a minimum value at small compressive strains. The out-of-plane constants exhibit a similar behavior under shear strain but under isotropic and uniaxial strain they increase with compression and decrease with tension, thus exhibiting a monotonic behavior. These DFT results are theoretically explained using only structural parameters and equilibrium dielectric constants. Our findings are consistent with available experimental data.

5.1 Introduction

For the last decade, two-dimensional materials have attracted a lot of interest. Since the appearance of graphene [83] single layer MoS_2 has been excessively studied. The monolayer structure was first observed by Lee et al. [84], with the first successful mechanical exfoliation from the bulk structure a little later by Mak et al. [85] in 2010. Due to strong surface effects there is a drastic change in the properties of this material with the change in the number of its layers. The characterization of the structure showed a transition of the material from an indirect semiconductor (bulk MoS_2) to a direct-gap material [86]. Since then, their electronic and magnetic properties [87],

[88],[89],[90],[91] have been extensively studied with more recent studies focusing on MoS₂ and WS₂ [92],[93].

Bulk Transition Metal Dichalcogenides (TMDs) are layered, anisotropic materials, known for various of their properties[94],[95]. Their ability to be easily exfoliated into separate layers makes them great candidates for many applications, such as optoelectronics, photovoltaics, photocatalysis and of course lubrication applications. Their general type is MX₂, where M:Mo,W and X:S, Se, Te. These materials have hexagonal symmetry ("Hexagonal, hP6, P6₃/mmc, No 194" space group) and the parameters that characterize them are the distance between neighboring Mo atoms in the x-direction (a), in the z-direction (c) and an internal parameter u which describes the relative distance between the M and the X atoms. The distance between the M-plane and the X-plane is $(\frac{3}{4} - u) \cdot c$ [96], usually mentioned as internal parameter z .

The bulk MX₂ structure is computationally represented with a unit-cell of 6 atoms; two atoms of a transition metal and four of a chalcogen. The left image in figure 5.1 shows a 4x4x1 top view of the unit cell and the on the right image a side view of the unit-cell of molybdenum disulfide. As seen from the top view the atoms create a hexagon similar with the one of graphene, only here the atoms are not in the same "layer". Bulk MX₂ consist of two trilayers. Each trilayer has a monolayer of M atoms sandwiched between two monolayers of X atoms. The trilayers interact with each other (the neighboring X monolayers) with weak van Der Waals interactions. There are vari-

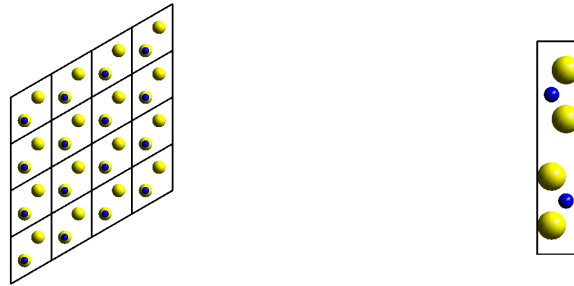


Fig. 5.1: MoS₂ bulk unit-cell where Mo and S atoms are denoted with blue and yellow spheres respectively

ous references in literature about the value of the lattice parameters. We can see some of them as well as the resulting values for each parameter of our calculations in table A.7 for MoS₂, in A.8 for MoSe₂, in A.9 for MoTe₂, in A.10 for WS₂, in A.11 for WSe₂ and in A.12 for WTe₂. It can be seen that GPAW overestimates the in-plane lattice parameter a by about 1%, apart from the WTe₂ structure, where it is underestimated by 1%. As far as the out-of plane parameter u is concerned the behavior is the same for all the structures; an overestimation of about 1.2%. It is already shown, that PBE functional is better for describing the in-plane behavior of the structure, compared to the LDA

which is best for the out-of-plane behavior.

MX_2 as bulk materials are indirect semiconductors with their band gaps shown in table 5.1 as calculated in this work. The valence band maximum (VBmax) is always located at the Γ -point of the Brillouin Zone (BZ) and the conduction band minimum (CBmin) at or near the K-point. In the second column of the same table we can see some experimental values of the band gap. The last column contains the results of experimental works on the in-plane dielectric constant. The electronic band structure

| Structure | E_g (eV) | E_g -exp(eV) | ϵ_{\perp} | ϵ_{\parallel} | ϵ_{eff} | ϵ (exp) |
|-------------------|------------|--------------------|--------------------|------------------------|------------------|------------------|
| MoS ₂ | 1.34 | 1.29[97], 1.23[98] | 12.3 | 7.2 | 9.4 | 17.0[99] |
| WS ₂ | 1.29 | 1.35[98] | 11.0 | 7.2 | 8.9 | 13.5[100] |
| MoSe ₂ | 1.24 | 1.10[97], 1.09[98] | 14.0 | 9.0 | 11.2 | 18.0[99] |
| WSe ₂ | 1.21 | 1.20[98] | 12.3 | 8.6 | 10.3 | 14.0[100] |
| MoTe ₂ | 0.87 | 1.00[97] | 19.2 | 13.0 | 15.8 | 20.0[99] |
| WTe ₂ | 0.88 | | 16.7 | 11.7 | 14.0 | |

Table 5.1: MX_2 bulk band gap, theoretical and experimental values, dielectric constant for in-plane and out-of-plane polarization and the respective effective value

for bulk MoS₂ and WS₂ is shown in fig.5.2.

The weak van der Waal interaction between the tri-layers makes it possible to easily obtain a monolayer[101] by mechanical exfoliation with no impurities as well as the Chemical Vapor Deposition (CVD) method[79]. In detail the atom positions and the vectors of the unit cell for a MX_2 monolayer can be seen in figure 5.3, as well as an image (a) of the lattice structure and (b) the respective Brillouin Zone(BZ).

There are many studies focusing on the electronic properties of TMDs [102], [103]. The value of the gap depends on the method used for the calculation. For example, for MoS₂ it varies from 1.53eV to 2.84eV [104], [105], [106], [107], [108], [94], [87] with the experimental values at 1.90eV [85] and 1.75eV [86]. The band gap for these structures

| | | | | | |
|---------|------------|-----------|------------|------------|------|
| Exp | 1.90 [85] | 1.75 [86] | | | |
| GW | 2.76 [94] | 2.14[157] | | | |
| GGA+vdW | 1.63 [107] | | | | |
| HSE06 | 2.10 [106] | | | | |
| LDA | 1.87 [108] | 1.89 | 1.9 [157] | | |
| PBE | 1.78 [104] | 1.72 [87] | 1.58 [108] | 1.70 [106] | 1.69 |

Table 5.2: MoS_2 single layer calculated and experimental band gap values

as calculated in this work is shown in table 5.3. All TMDs display similar electronic behavior with a direct gap at K-point as shown in figure 5.4 and a decrease in the value of the gap for heavier TMDs.

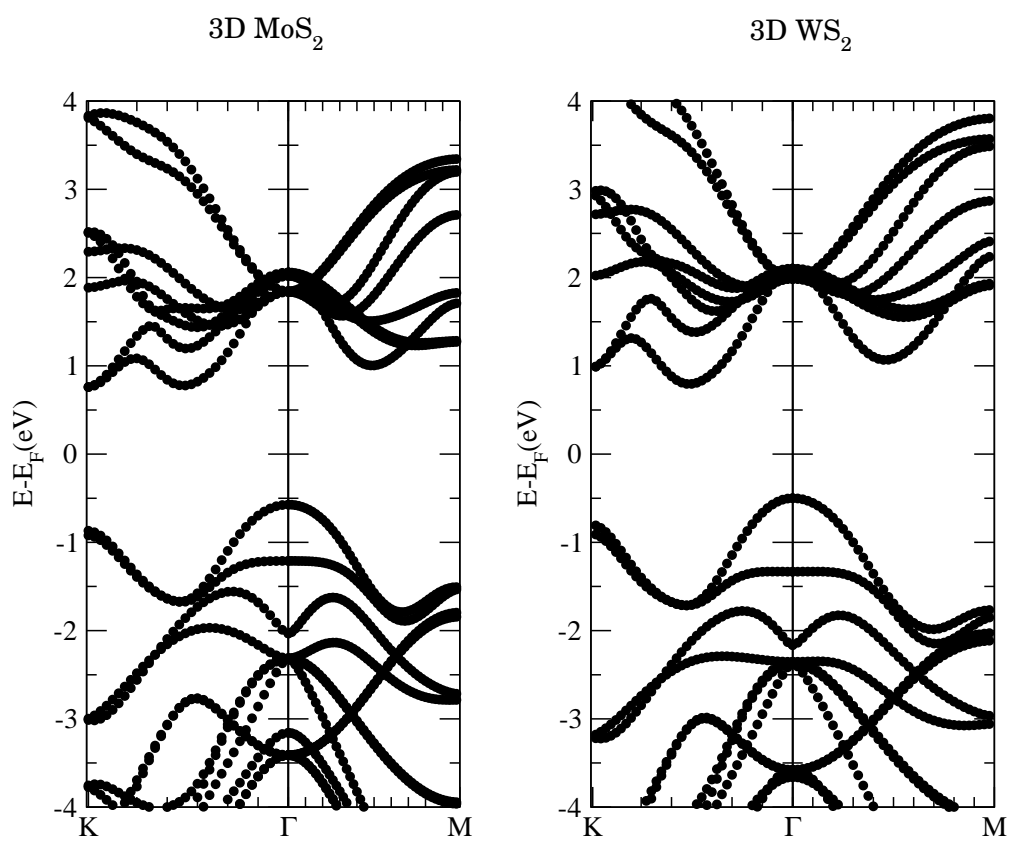


Fig. 5.2: Electronic band structure for bulk MoS₂ and WS₂

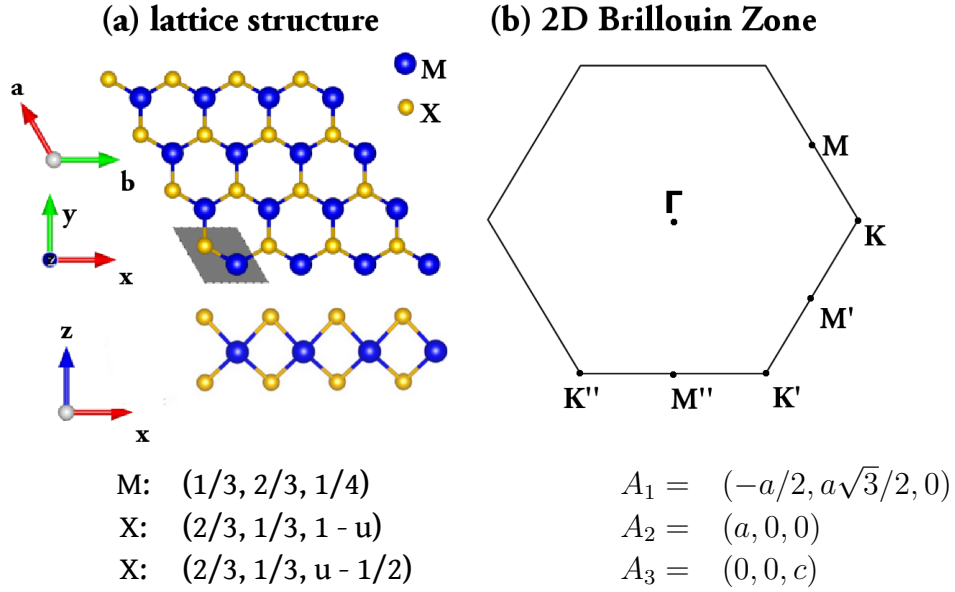


Fig. 5.3: Atom positions and unit cell vectors for the single layer MX_2 with (a) a top and side view of the unit cell and (b) the respective BZ

This dependence is also reflected in the values of the dielectric constant as shown in table 5.3. These values are almost halved, compared to the values of the respective bulk structures. As shown previously [110], the dielectric constant also depends on the vacuum(space in the z-direction, between two consequent monolayers, used in the calculation). The dielectric constant for in-plane polarization decreases with a slower rate than the dielectric constant for out-of-plane polarization. The effect of vacuum on the dielectric constant makes it difficult to compare results of different studies [111], [112]. In this work vacuum=12Å.

| Structure | a | u | X-X dist | volume | E_g (eV) | ϵ_{\perp} | ϵ_{\parallel} | ϵ_{eff} |
|-------------------|------|-------|----------|--------|------------|--------------------|------------------------|------------------|
| MoS ₂ | 3.20 | 0.635 | 3.15 | 133.56 | 1.69 | 6.1 | 3.6 | 4.3 |
| WS ₂ | 3.19 | 0.630 | 3.18 | 134.13 | 1.85 | 5.3 | 3.4 | 4.2 |
| MoSe ₂ | 3.30 | 0.631 | 3.35 | 145.13 | 1.51 | 7.0 | 4.1 | 5.4 |
| WSe ₂ | 3.31 | 0.628 | 3.39 | 146.06 | 1.63 | 6.0 | 3.8 | 4.8 |
| MoTe ₂ | 3.56 | 0.628 | 3.59 | 170.68 | 1.07 | 9.1 | 4.8 | 6.6 |
| WTe ₂ | 3.56 | 0.629 | 3.62 | 171.05 | 1.06 | 8.2 | 4.6 | 6.1 |

Table 5.3: MX_2 single layer lattice parameters, band gap and also dielectric constant for in-plane and out-of-plane polarization and the respective effective value

The tuning of the electronic properties of the TMDs structures is interesting for

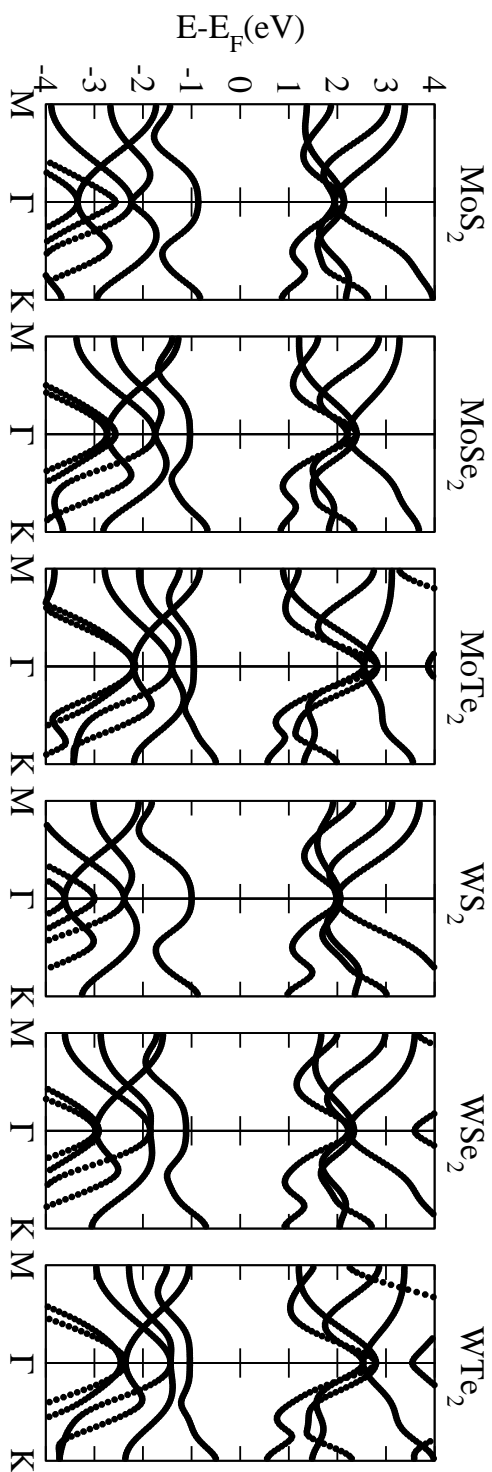


Fig. 5.4: TMDs band structure along the M-T-K path in the Brillouin Zone

electronic and optoelectronic applications. There have been various attempts either by using alloys of the TMDs [113] or with strain [114], [102], [106], [115], [116] achieving a switching of each material from semiconducting to metallic. This tuning is quite useful when trying to create hetero-structures, exploiting the quantitative differences of these six materials and also graphene, hexagonal Boron Nitride (BN) and fluorographene, using them as 'Lego-blocks' [117]. An attempt [118] has also been made in understanding the behavior of the dielectric constant under strain for in-plane polarization.

Materials with this type of anisotropy can be considered as *transverse isotropic* [119] materials since one direction (z-axis) differs from the other two. If \mathbf{d} (0,0,1) is the unit vector in the direction of the distinction then the dielectric tensor for each material, which connects the dielectric displacement \mathbf{D} with the electric field \mathbf{E} as shown in eq. 5.1, can be written in the form of eq. 5.2

$$D_i = \varepsilon_0 \cdot \varepsilon_{ik} E_k \quad (5.1)$$

where ε_0 is the permittivity of free space and

$$\varepsilon_{ik} = \varepsilon_{\perp} \cdot \delta_{ik} + (\varepsilon_{\parallel} - \varepsilon_{\perp}) \cdot d_i \cdot d_k \quad (5.2)$$

where ε_{\parallel} is the dielectric constant for \mathbf{E} applied along the c axis direction ($\mathbf{E} \parallel c$) and ε_{\perp} is the dielectric constant for perpendicular to the c axis excitation ($\mathbf{E} \perp c$). The value of the constant for out-of-plane polarization and for in-plane polarization as well as the effective dielectric constant as given by the equation $\varepsilon = \sqrt{\varepsilon_{\perp} \cdot \varepsilon_{\parallel}}$ [95] are shown in table 5.1.

The aim of this work is to expand the calculations, with strains, that up to now, as far as we know, haven't been studied yet. We offer a new point of view for the electronic properties of the materials under strain, by studying the shifting of the positions of the CBmin and VBmax. Since these materials under strain become fully anisotropic we also study and attempt to qualitatively explain the behavior of the dielectric constant not only for in-plane polarization but also for out-of-plane polarization, making it possible to estimate an effective value for the dielectric constant.

5.2 Methodology

In this work we use the Density Functional Theory (DFT) through the open source, Grid-based Augmented-Wave (GPAW) implementation, [120],[121] which uses real space grid for electron densities and wave functions. We implement the GGA-PBE exchange-correlation functional [122]. The atomic relaxation is done with the conjugate gradient approximation and the dielectric constant is calculated through the linear response

theory [123]. Electron-electron interactions are taken into account using the random phase approximation (RPA). For the in-plane polarization the wave-vector of the incident light is taken to be parallel to the MX_2 layer ($E \perp c$) and for the out-of-plane polarization the wave-vector is perpendicular to the MX_2 layer ($E \parallel c$).

5.3 Results and Discussion

5.3.1 Strain definitions

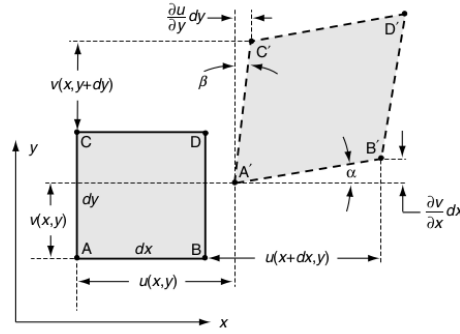


Fig. 5.5: 2D representation of strain deformation[124]

Normal strain in the x direction is defined as

$$\varepsilon_x = \frac{A'B' - AB}{AB} \quad (5.3)$$

According to figure 5.5 $A'B' = \sqrt{(dx + \frac{\partial u}{\partial x} dx)^2 + (\frac{\partial v}{\partial x} dx)^2} \approx (1 + \frac{\partial u}{\partial x}) dx$. We also know that $AB = dx$ so with that and by following the small deformation theory, we can see that

$$\varepsilon_x = \frac{\partial u}{\partial x} \quad (5.4)$$

in the same way we can see that

$$\varepsilon_y = \frac{\partial v}{\partial y} \quad (5.5)$$

Apart from normal strain we can also have shear strain. Shear strain is defined as the change in the angle between the two orthogonal directions. Keep in mind that engineering shear strain is different from pure shear strain. Engineering shear strain is the total measure of the shear strain eg. $\gamma_{xy} = \varepsilon_{xy} + \varepsilon_{yx} = 2 \cdot \varepsilon_{xy}$ so γ_{xy} is the total shear strain in the x-y plane

For example, in the two dimensional case, as shown in figure 5.5 the shear strain in the xy direction is defined as $\gamma_{xy} = \frac{\pi}{2} - C'\hat{A}'B' = \alpha + \beta$. For small deformations, $\alpha \approx \tan \alpha$ and $\beta \approx \tan \beta$, so shear strain can be written:

$$\gamma_{xy} = \frac{\frac{\partial v}{\partial x} dx}{dx + \frac{\partial u}{\partial x} dx} + \frac{\frac{\partial u}{\partial y} dy}{dy + \frac{\partial v}{\partial y} dy} = \frac{\partial u}{\partial y} + \frac{\partial v}{\partial x} \quad (5.6)$$

By interchanging x and y and v and u , we can see that $\gamma_{xy} = \gamma_{yx}$. Having in mind the above, the general deformation matrix of engineering strain is defined as:

$$S = \begin{bmatrix} \varepsilon_{xx} & \gamma_{xy} & \gamma_{xz} \\ \gamma_{xy} & \varepsilon_{yy} & \gamma_{yz} \\ \gamma_{xz} & \gamma_{zy} & \varepsilon_{zz} \end{bmatrix} \quad (5.7)$$

Focusing in our structures, if the initial vector matrix is

$$R = \begin{bmatrix} a_{1x_0} & a_{2x_0} & a_{3x_0} \\ a_{1y_0} & a_{2y_0} & a_{3y_0} \\ a_{1z_0} & a_{2z_0} & a_{3z_0} \end{bmatrix} \quad (5.8)$$

then the final vector matrix is going to be given by the equation $R' = (I + e \cdot S) \cdot R$, where e is the strain. Fig. 5.6 shows the effect each strain has on the unit cell of MX_2 .

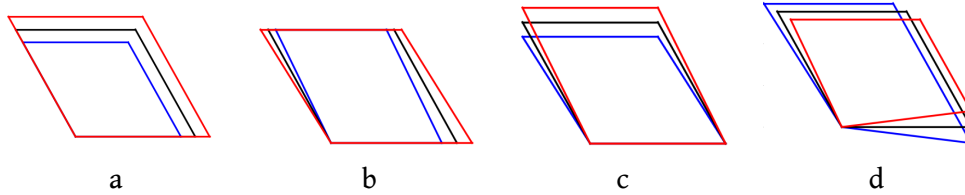


Fig. 5.6: Effect of a) isotropic, b) uniaxial x, c) uniaxial y and d) shear xy strain on the unit cell of MX_2 . With black we denote the relaxed structure, with red the expanded and with blue the compressed structure.

5.3.2 Structural details of strained structures

The effect of strain in the TMDs is interesting both as a suspended material and a material positioned onto a substrate, as we already mentioned. The strains we apply in the six transition metal dichalcogenides are; isotropic strain (since the structure is 2D it can be considered bi-axial), uniaxial strain on x -axis, on y -axis and shear strain in the xy -direction. The strain applied ranges from 12% compressive to 12% tensile. Previous experiments[125] with MoS_2 reach values up to 11% out-of-plane isotropic

strain and others [126] prove that the material conveniently has high elasticity for the creation of hetero-structures with other less flexible materials, such as graphene. All the structure relaxations are performed with the Simplex Algorithm [127]. The energy dependence on strain can be seen in figure 5.7 as well as the behavior of u lattice parameter.

For the sake of brevity, we discuss the effect of strain on the structural properties only for MoS_2 . Apart from the change in the relative positions between the atoms in the z direction, indicated from the u parameter, it is important to consider the change in the shape of the unit cell and the effect it has on atoms in neighboring cells. In figure 5.7 we can see the angle $S\hat{M}oS$, the $S - S$ distance and the $Mo - S$ distance of the MoS_2 molecule in relation to strain. In the graphs, that distance is denoted as the $Mo_3 - S$ distance.

For isotropic strain, both the $S\hat{M}oS$ angle and the $S - S$ distance decrease with expansion, while the distance between the Mo atom and the 6 neighboring S atoms ($Mo_1 - S$, $Mo_2 - S$ and $Mo_3 - S$) increases. Uniaxial x strain has almost the same behavior with isotropic strain, apart from the Mo-S distance of one set of S atoms where instead of increase with expansion the distance decreases. Uniaxial y strain behaves the same for the $S\hat{M}oS$ angle and the $S - S$ distance, while the Mo-S distance for one set increase but for the other two the distance remains almost the same. Shear xy strain has a more complicated behavior with the expansion of the structure. The $S\hat{M}oS$ angle increases, the $S - S$ distance remains relatively the same, one set of Mo - S distances remains the same, one increases and the other decreases with expansion, which is expected if we take into consideration the effect of shear strain in the unit cell, as we mentioned before 5.6.

5.3.3 Effect of strain on electronic properties

As we already mentioned, there are some works done, concerning the tuning of the electronic properties with strain. Results of the calculations done in this work are shown in figure 5.8. We observe a similar qualitative behavior for all TMDs. While, the band gap decreases with both compressive and tensile strain, compressive strain has a less drastic effect on it. MS_2 structures achieve a metallic character for high values of tensile isotropic strain ($>10\%$), while MTe_2 structure reach these values only for compressive ($>8\%$) isotropic and uniaxial x strains.

For the MSe_2 structures, the band gap decreases with any type of strain, whereas the other structures have a gap increase with small compressive strain. For all MX_2 we have the same values for uniaxial x and uniaxial y tensile strain, for compressive shear xy with compressive uniaxial y and for compressive isotropic with uniaxial x strain, for

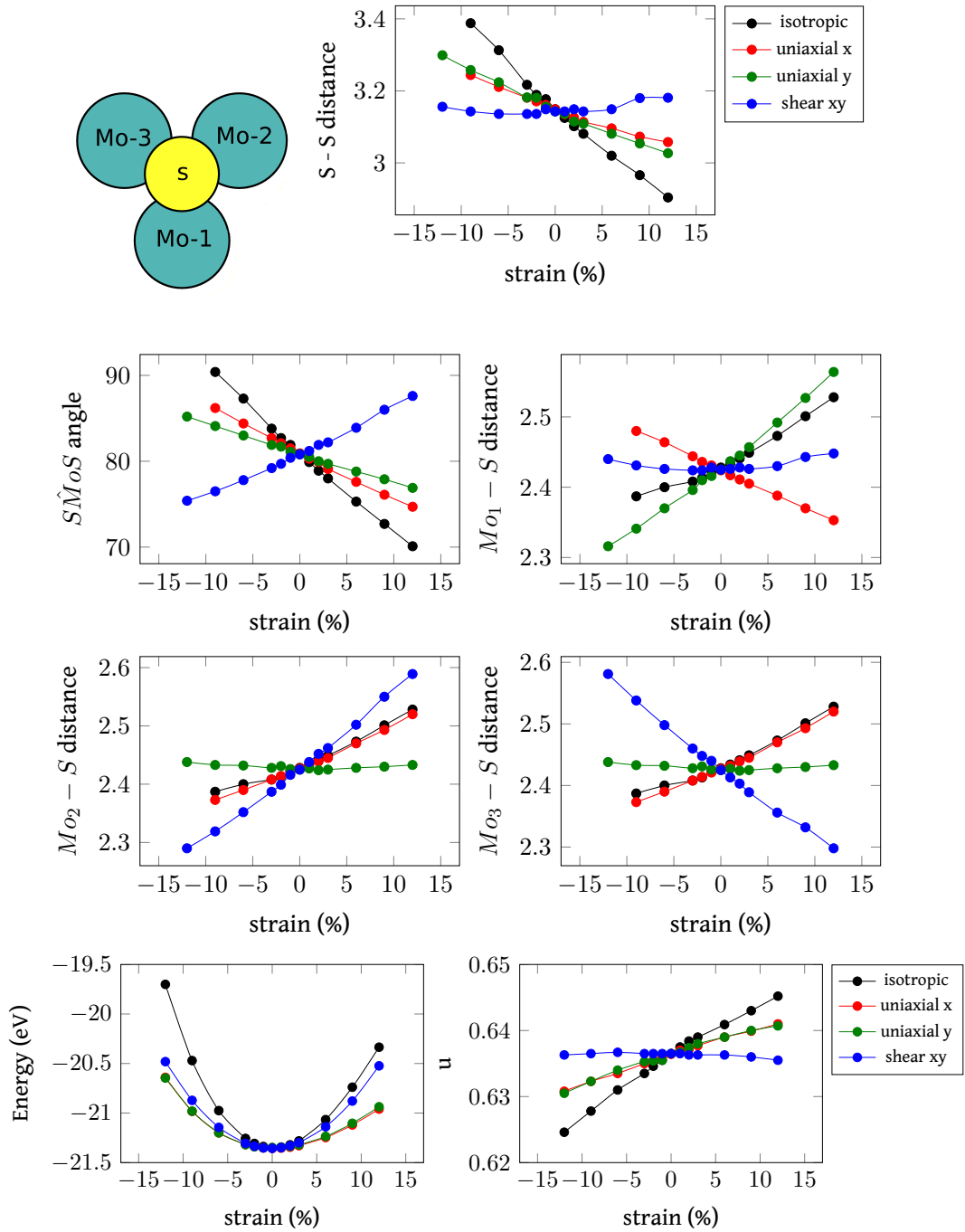


Fig. 5.7: MoS_2 structural details under strain

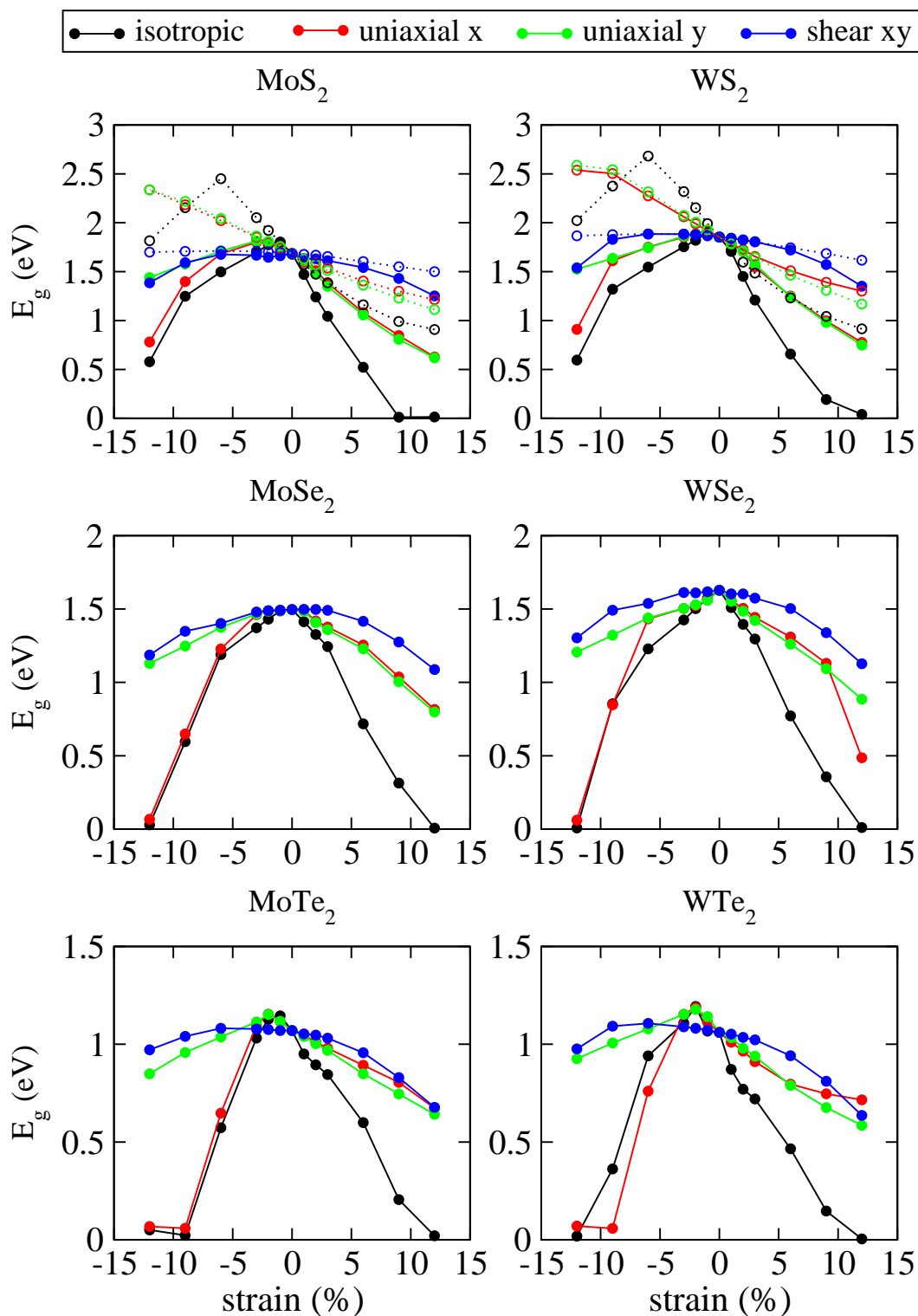


Fig. 5.8: Band gap, E_g , versus strain for all TMDs and all types of strain. Results from calculations are shown with black circles for isotropic strain, red for uniaxial x, green for uniaxial y and blue for shear xy. For MS₂ (top two plots) the direct gap at K-point of the BZ is also shown with open circles and dotted lines

which we must also note that we have a steeper decrease of E_g than with tensile strain. Shear xy strain's effect on the band gap is significantly smaller than all other types of strain. We also observe a similar behavior of the structures with the same chalcogen, while the transition metal doesn't seem to affect the band gap.

Strain also affects the positions of the CBmin and VBmax of each structure. We already mentioned that for 0% strain the structures are direct gap semiconductors, with both the CBmin and the VBmax positions at K-point of the Brillouin Zone. Focusing again on MoS₂, if we apply a small tensile strain, the position of the VBmax shifts from the K-point to the Γ -point, making the structure an indirect gap material. Since these shifts become more complicated with bigger values of tensile strain and with compressive strain, we present the diagrams shown in figure 5.9

For very small strains the band structures and, thus, the CBmin and VBmax positions, are usually the same for the $\Gamma - K - M - \Gamma$, $\Gamma - K' - M' - \Gamma$ and $\Gamma - K'' - M'' - \Gamma$ paths within the accuracy of DFT. However, for shear xy and large uniaxial strains the degeneracy of these paths is lifted. This is also suggested for K, K' and M, M' in previous calculations[115]. This effect is not present with isotropic strain, where the symmetry is retained.

In detail, for shear xy strain, we examine the Brillouin zone under strain. If the unit cell for an unstrained lattice has the form shown in eq.5.9,

$$\begin{cases} a1 = a_{1x} \cdot \hat{x} + a_{1y} \cdot \hat{y} + a_{1z} \cdot \hat{z} \\ a2 = a_{2x} \cdot \hat{x} + a_{2y} \cdot \hat{y} + a_{2z} \cdot \hat{z} \\ a3 = a_{3x} \cdot \hat{x} + a_{3y} \cdot \hat{y} + a_{3z} \cdot \hat{z} \end{cases} \quad (5.9)$$

then the general form of the unit cell under shear xy strain, taking into consideration the values for each $a_{i,n}$ (where $i=1,2,3$ and $n=x,y,z$) coefficient, is as shown in eq.5.10

$$\begin{cases} a1 = \frac{a}{2} \cdot (1 + s \cdot \sqrt{3}) \cdot \hat{x} + \frac{a}{2} \cdot (\sqrt{3} + s) \cdot \hat{y} \\ a2 = a \cdot \hat{x} + a \cdot s \cdot \hat{y} \\ a3 = c \cdot \hat{z} \end{cases} \quad (5.10)$$

where a is the lattice constant and s is the percentage of strain, then the unit vectors of the Brillouin zone are estimated from eq.5.11

$$\vec{b}_1 = 2 \cdot \pi \cdot \frac{\vec{a}_2 \times \vec{a}_3}{\vec{a}_1 \cdot (\vec{a}_2 \times \vec{a}_3)}, \quad \vec{b}_2 = 2 \cdot \pi \cdot \frac{\vec{a}_3 \times \vec{a}_1}{\vec{a}_2 \cdot (\vec{a}_3 \times \vec{a}_1)}, \quad \vec{b}_3 = 2 \cdot \pi \cdot \frac{\vec{a}_1 \times \vec{a}_2}{\vec{a}_3 \cdot (\vec{a}_1 \times \vec{a}_2)} \quad (5.11)$$

to be (shown in eq.5.12):

$$\begin{cases} \vec{b}_1 = \frac{4 \cdot \pi \cdot s}{a \cdot \sqrt{3} \cdot (s^2 - 1)} \cdot \hat{x} - \frac{4 \cdot \pi}{a \cdot \sqrt{3} \cdot (s^2 - 1)} \cdot \hat{y} \\ \vec{b}_2 = -\frac{2 \cdot \pi \cdot (\sqrt{3} + s)}{a \cdot \sqrt{3} \cdot (s^2 - 1)} \cdot \hat{x} + \frac{2 \cdot \pi \cdot (1 + s \cdot \sqrt{3})}{a \cdot \sqrt{3} \cdot (s^2 - 1)} \cdot \hat{y} \\ \vec{b}_3 = \frac{2 \cdot \pi}{c} \hat{z} \end{cases} \quad (5.12)$$

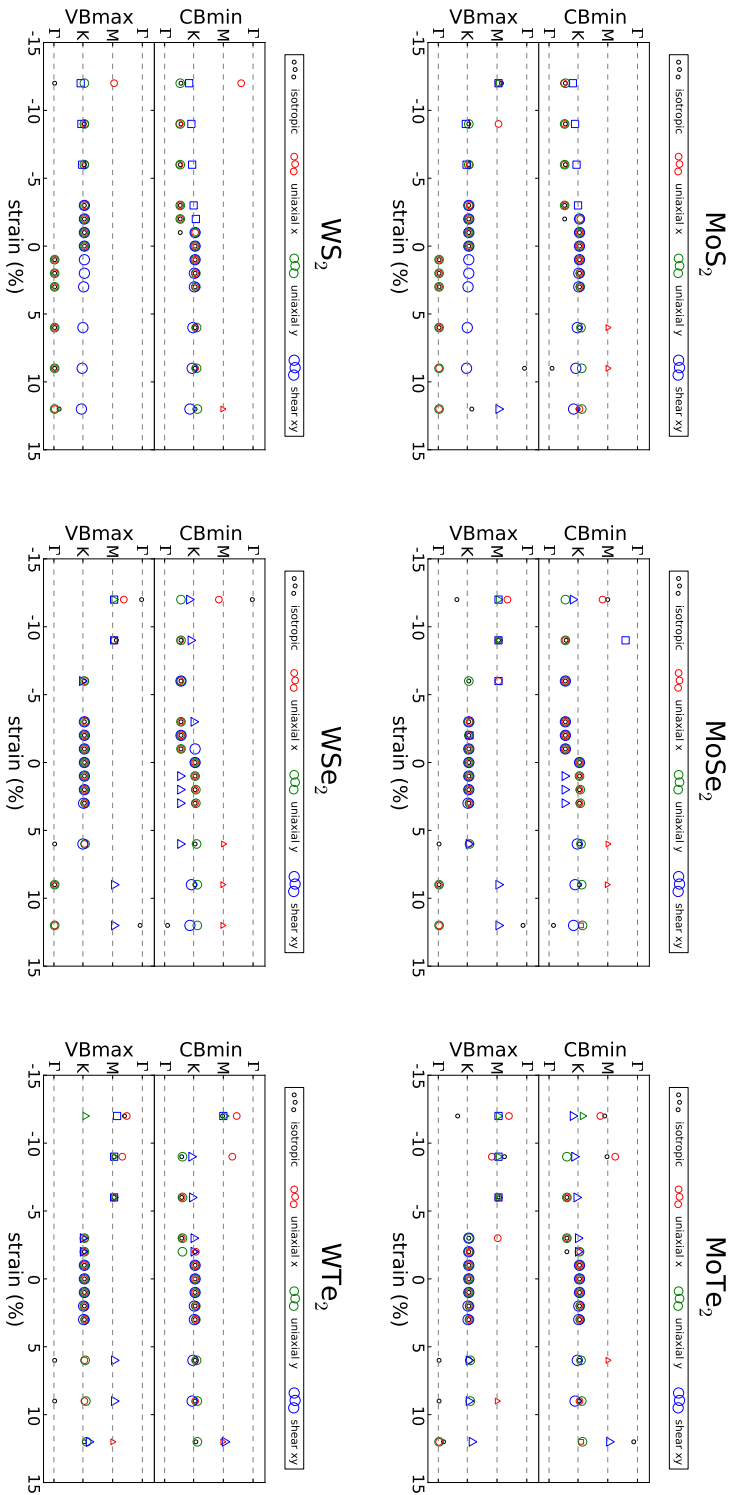


Fig. 5.9: CBmin-VBmax diagrams for all six TMDs structures. The black (very small) circles denote the CBmin and VBmax positions for isotropic strain, the red (small) for uniaxial-x, the green (large) for uniaxial-y and the blue (very large) for shear strain. The triangle and square symbols denote the CBmin and VBmax positions along the $\Gamma - K' - M' - \Gamma$ and $\Gamma - K'' - M'' - \Gamma$ path of the Brillouin Zone, respectively, and are marked when they differ from the ones along the $\Gamma - K - M - \Gamma$ path. The dashed lines indicate the positions of the high symmetry points of the BZ. The top area of each diagram shows the CBmin and the bottom the VBmax positions

The effect of shear xy strain on the shape of the Brillouin Zone can be observed in fig.5.10 We can see the effect of both large(15%) and small(%) for compressive and ten-

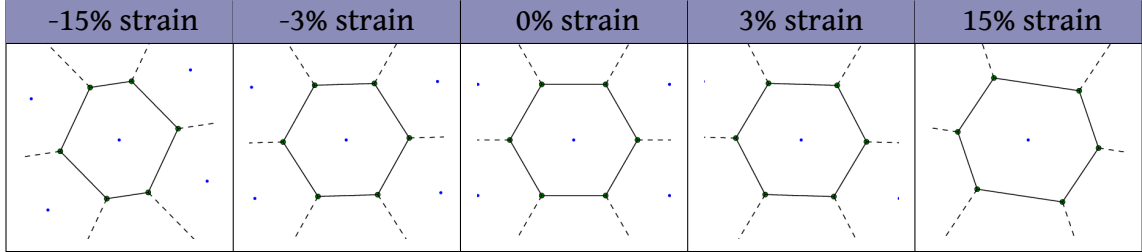


Fig. 5.10: Effect of shear strain in the shape of the BZ

sile strain, in comparison with the BZ of the unstrained structure. The brake in the symmetry is obvious. A detail image with the changes of the conduction and valence band with strain can be seen in fig.A.1 for MoS₂, fig.A.4 for WS₂, fig.A.2 for MoSe₂, fig.A.5 for WSe₂, fig.A.3 for MoTe₂ and fig.A.6 for WTe₂.

The points corresponding to the different CBmin and VBmax along the $\Gamma - K' - M' - \Gamma$ and $\Gamma - K'' - M'' - \Gamma$ paths are marked with triangles and squares, where K-M are replaced by K'-M' and K''-M'', respectively. Figs.5.8 and 5.9 contain all essential information for the electronic behavior of strained MX₂ structures. For instance, for WS₂ (bottom left plot of fig. 5.9), even very small compressive isotropic strains bring the CBmin from K to a point between the Γ and K. The VBmax remains at K (only for extreme strain it goes to Γ) so that the gap is indirect. Very small tensile isotropic strain shifts the VBmax to the Γ point and leave the CBmin at K, so that the gap is indirect. Thus, even small isotropic strain makes WS₂ monolayer an indirect gap semiconductor (at $\Gamma - K$) for tensile strain. The conclusions are very similar for uniaxial strains in the range of -10% to 10%, in agreement with recent experiments [128]

The positions of CBmin and VBmax seem to depend on the chalcogen part of the structure (diagrams in the same column of figure 5.9). Excluding the MSe₂ structures, all other TMDs remain direct gap semiconductors for small strains. For shear xy strain the position of VBmax remains at K-point, for any value of strain. Apart from the MS₂ structures, the VBmax doesn't shift from K-point for small values of any type of strain. Generally an erratic behavior of these positions is observed for larger values of compressive strain, in contrast to the smooth shifting of these positions for tensile strain.

5.3.4 Effect of Strain on dielectric constant

In regards to the dielectric constant, as we already mentioned, we have a similar qualitative behavior for all TMDs. Since the materials under strain become completely

anisotropic, all three diagonal elements of the dielectric tensor need to be included in our analysis.

Qualitatively, for out-of-plane polarization, we can see from the results (shown in the right panel of fig.5.11), that the each type of strain has a different effect on the dielectric constant. We can see that shear xy strain's effect on it is small, with a constant increase. For all three other types of strain the dielectric constant decreases with tensile and increases with compressive strain. We must also note that uniaxial x and uniaxial y strain have the same quantitative effect.

For in-plane polarization (either in the x or y direction), the effect of strain is more complex. Primarily, we observe a similar behavior for structures with the same chalcogen. Also we must note that with isotropic strain the structure retains the in-plane isotropy of the undeformed structure.

Specifically for in-plane polarization in the y-direction, uniaxial x strain displays a linear increase with the expansion of the structure that becomes more prominent as the chalcogen gets 'smaller'. All other types of strain result in the increase of the dielectric constant. As we can see in the graphs, as the chalcogen gets 'heavier' the rate with which the dielectric constant increases is faster, resulting in a wider range of values, especially under compressive strain.

For in-plane polarization in the x-direction the behavior of the dielectric constant is a reflection of the polarization in the y-direction.

Quantitatively, the effect of strain in a structure is described through the displacement vector $\mathbf{U}(\mathbf{x})$. Following [129], we can link the dielectric tensor ε with the strain tensor $u_{i,j}$ through eq. 5.13

$$\varepsilon_{ik} = \varepsilon_{ik}^0 + \delta\varepsilon_{ik} \quad (5.13)$$

where the general form of $\delta\varepsilon$ is shown in eq. 5.14, ε^0 is the dielectric tensor for the undeformed structure, ω_{lm} is the rotation tensor (which in our case is zero) and a_{iklm} and γ_{iklm} are fourth order electrostriction tensors which depend on the structure of the undeformed material.

$$\delta\varepsilon_{ik} = a_{iklm} \cdot u_{lm} + \gamma_{iklm} \cdot \omega_{lm} \quad (5.14)$$

A linear description of eq. 5.14 is usually used in thin films [130] by replacing $\delta\varepsilon$ in eq. 5.13 with $\Delta\varepsilon$ of eq. 5.15

$$\Delta\varepsilon = a_1 \cdot \Delta x_n / x_n + a_2 \cdot \Delta V / V, \quad n : x, y, z \quad (5.15)$$

where Δx_z is the film thickness and $\Delta V / V$ the volumetric strain (dilatation). The electrostriction [131] coefficients a_1 and a_2 are associated with material parameters.

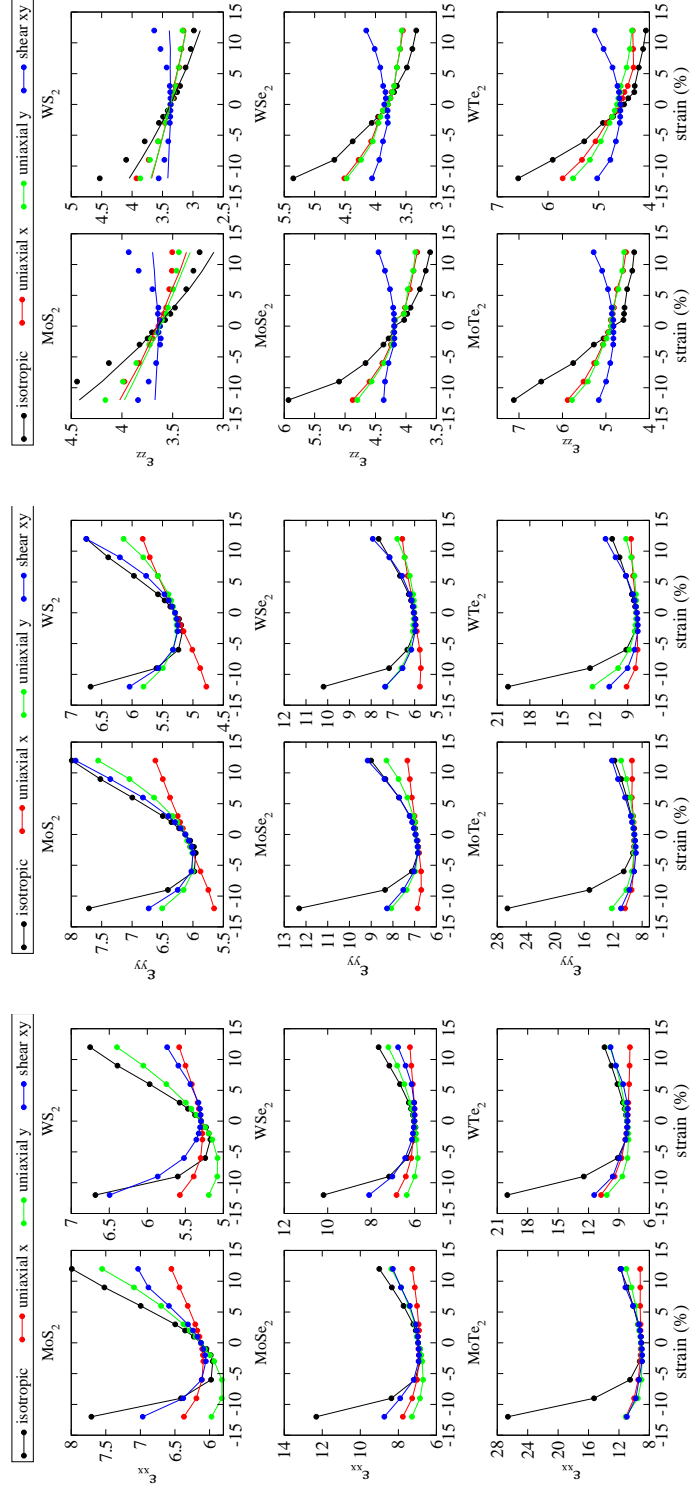


Fig. 5.11: In-plane ϵ_{xx} , ϵ_{yy} and out-of-plane ϵ_{zz} static relative permittivities of MX_2 structures as a function of strain

For an isotropic material they can be calculated through the dielectric constant of the undeformed structure (eqs. 5.16, 5.17).

$$a_1 = -\frac{2}{5} \cdot (\varepsilon - 1)^2 \quad (5.16)$$

$$a_2 = -\frac{1}{3} \cdot (\varepsilon - 1)(\varepsilon + 2) + \frac{2}{15} \cdot (\varepsilon - 1)^2 \quad (5.17)$$

where ε is the dielectric constant of the unstrained structure. Fitting this linear equation 5.13,5.15 to our data results in deviations <2% for small deformations and \simeq 8-10% for finite deformations, the latter can be considered high.

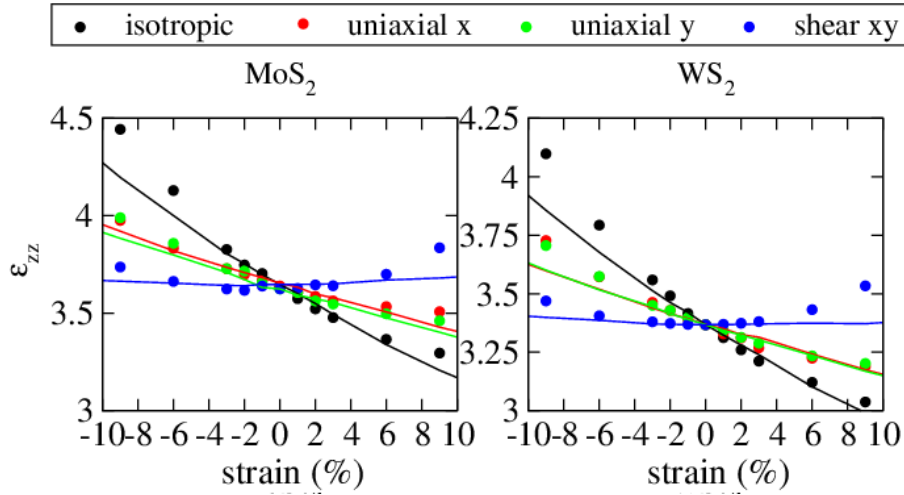


Fig. 5.12: Out-of-plane static relative permittivity for MS_2 as a function of all types of strain. Points are DFT results and continuous curves are theoretical predictions in the linear regime

Therefore, for a better description of the dielectric tensor and since the deformation applied to our structures cannot be considered small, higher order terms need to be included in the strain tensor. This entails the Green strain tensor implementation (rather than the Cauchy one) which includes quadratic terms, and can be applied both for small and finite deformations. Its general form in tensor notation can be seen in eq. 5.18

$$u_{ij} = \frac{1}{2} \cdot \left(\frac{\partial U_i}{\partial x_j} + \frac{\partial U_j}{\partial x_i} + \frac{\partial U_k}{\partial x_i} \cdot \frac{\partial U_k}{\partial x_j} \right) \quad (5.18)$$

With this method the deviation between the dielectric tensors (theory and calculation) for finite deformations is reduced to about 5%.

For a full description of the dielectric tensor a different approach is required. Eq.5.3.4 show a full description of the elements of the dielectric tensor (omitting the rotation term).

$$\begin{aligned}\varepsilon_{ik} = & \varepsilon_{ik}^0 + (r_1 \cdot \delta_{ik} \cdot \delta_{lm} + r_2 \cdot \delta_{il} \cdot \delta_{km} + r_3 \cdot \delta_{im} \cdot \delta_{kl} \\ & + r_4 \cdot \delta_{ik} \cdot d_l \cdot d_m + r_5 \cdot \delta_{il} \cdot d_k \cdot d_m + r_6 \cdot \delta_{im} \cdot d_k \cdot d_l + r_7 \cdot \delta_{kl} \cdot d_i \cdot d_m \\ & + r_8 \cdot \delta_{km} \cdot d_i \cdot d_l + r_9 \cdot \delta_{lm} \cdot d_i \cdot d_k + r_{10} \cdot d_i \cdot d_k \cdot d_l \cdot d_m) \cdot u_{lm}\end{aligned}$$

where \mathbf{d} is the direction of anisotropy of the unstrained structure ($\mathbf{d} = [0,0,1]$), $u_{i,j}$ is the strain tensor, $r_1 \dots r_{10}$ are scalar coefficients linked with material parameters and $\delta_{i,j}$ is Kronecker's delta.

The above equation (eq.5.3.4) can be simplified when we take under consideration the symmetries of the strain tensor ($u_{i,j} = u_{j,i}$) and the elements of the strain tensor equal to zero due to the initial unit cell of the structure ($u_{1,3} = u_{2,3} = u_{3,1} = u_{3,2} = 0$). With this the resulting equations for the elements of the dielectric tensor are shown in eq.5.19.

$$\begin{aligned}\delta\varepsilon_{1,1} &= r_1 \cdot (u_{1,1} + u_{2,2} + u_{3,3}) + (r_2 + r_3) \cdot u_{1,1} + r_4 \cdot u_{3,3} \\ \delta\varepsilon_{1,2} &= (r_2 + r_3) \cdot u_{2,1} \\ \delta\varepsilon_{1,3} &= 0 \\ \delta\varepsilon_{2,1} &= \delta\varepsilon_{1,2} \\ \delta\varepsilon_{2,2} &= r_1 \cdot (u_{1,1} + u_{2,2} + u_{3,3}) + (r_2 + r_3) \cdot u_{2,2} + r_4 \cdot u_{3,3} \\ \delta\varepsilon_{2,3} &= 0 \\ \delta\varepsilon_{3,1} &= 0 \\ \delta\varepsilon_{3,2} &= 0 \\ \delta\varepsilon_{3,3} &= (r_1 + r_9) \cdot (u_{1,1} + u_{2,2} + u_{3,3}) + (r_2 + r_3 + r_4 + r_5 + r_6 + r_7 + r_8 + r_{10}) \cdot u_{3,3}\end{aligned}\tag{5.19}$$

From this we see that the change in the in-plane terms of the dielectric constant has an extra term regarding the change with strain of the structure in the z- direction ($u_{3,3}$). By fitting these terms to our DFT results we obtain an *almost* fit for all eigenvalues of the dielectric constant. This fit is shown in fig.5.13. It is interesting to note that $\delta\varepsilon_{3,3}$ of eq.5.19 is equivalent with $\Delta\varepsilon$ for $n = z$ of equation 5.15.

5.4 Conclusions

We have studied the effects of the different types of strain on the electronic band structure and the dielectric constant of 2D semiconducting TMDs. At zero strain, electronic band gaps are direct for all MX_2 and while they generally decrease with strain and for heavier chalcogen X, we find rich variation of electronic properties depending

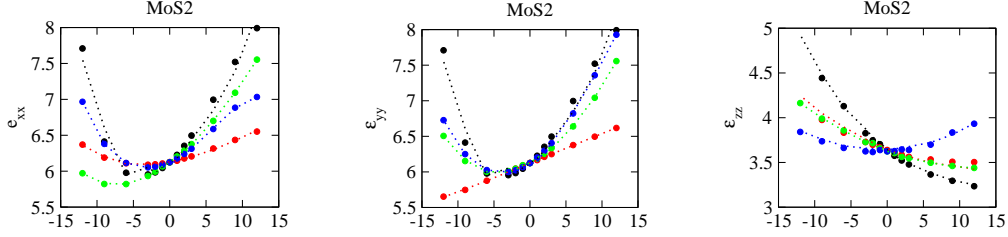


Fig. 5.13: In-plane ϵ_{xx} , ϵ_{yy} and out-of-plane ϵ_{zz} static permittivity of MoS₂ as a function of strain. Points are DFT results and dotted lines are the fitting to the theoretical predictions. Black color refers to isotropic strain, red to uniaxial x, green to uniaxial y and blue to shear xy strain

on X and the type of strain. For MS₂ the direct gap changes to indirect for isotropic and uniaxial, whereas for shear, these structures remain direct gap up to very large strains. MSe₂ remain direct gap semiconductors under tensile isotropic and uniaxial moderate strain (up to 5%) and become indirect in all other cases. MTe₂ remain direct for all types of moderate tensile and very small compressive strains. The effects of broken lattice symmetry for uniaxial and shear strain on the band structure were discussed. We also present results for the in-plane ϵ_{xx} , ϵ_{yy} and out-of-plane ϵ_{zz} diagonal elements of the static relative permittivity tensor. All three constants increase with heavier X and are strain dependent. The in-plane constants, which are equal in unstrained monolayers, generally increase with strain, exhibiting a minimum at small compressive strains. The out-of-plane constant under isotropic and uniaxial strain increases with compressive and decreases with tensile. Under shear strain, it exhibits a similar to the in-plane constants variation. These results are theoretically explained solely based on structural parameters and equilibrium dielectric constant values. Many of our predictions for band structure and dielectric constant are in agreement with available data or could be verified by experiment.

Summary and Perspective

Molecular Dynamics simulations with Tersoff and Brenner interatomic potentials describe the structural and vibrational properties adequately, in both the single phase systems (crystalline and amorphous carbon, free n-D) and the mixed phase systems studied (n-D - a-C and UNCD).

Interesting peaks are observed in the low frequency region of the vibrational spectrum, correlating the dynamical properties of the structure with the size of the nanocrystals and even the average grain size for the UNCD.

Investigation of the effect of Hydrogen (H) in the bulk modulus of amorphous carbon shows that the structure gets softer with the increase in the percentage of H. The vibrational spectrum of free n-D with H seems to display interesting features related to H along with the expected peaks of carbon. On-going work shows that H affects the structural and mechanical properties of the carbon nanostructures studied in this work and modifies vibrational spectra.

Density Functional Theory (DFT) calculations on the interaction of H with the exposed edges and corners of quasi-1D MoS₂ ribbons and quasi-0D MoS₂ flakes, verify the stability/activity of the Mo-edge. At the same time, they are consistent with the experimentally observed stability/activity of S-terminated edges. The investigation of the hybrid MoS₂/Graphene structure with DFT shows that the graphene substrate affects stability/reactivity of MoS₂ significantly. The lattice mismatch between the components of the hybrid MoS₂/Graphene systems results in strained MoS₂ layers. Even though we saw that there is no particular preference in the way the MoS₂ nanostructure is oriented onto the graphene substrate, the strain some of these heterostructures undergo is high. More work is needed to further clarify the exact role of the graphene substrate on H adsorption on MoS₂ nanostructures.

Finally, the effects of strain in the MoS₂ and other TMD monolayers were investi-

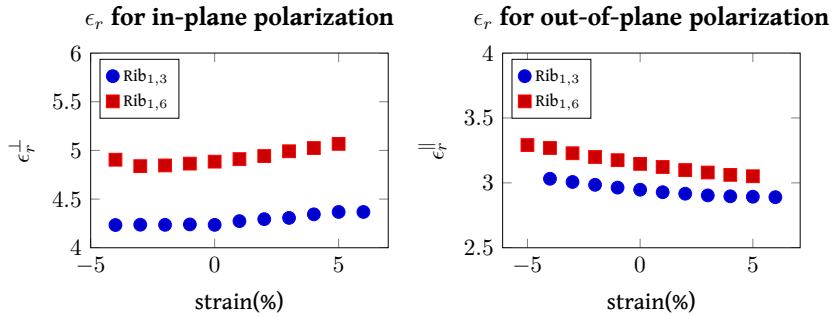


Fig. 6.1: Effect of uniaxial-x strain in the quasi-1D ribbons, Rib_{1,3} and Rib_{1,6}

gated. We saw that the electronic and dielectric properties are mainly affected from the chalcogen part of the TMDs. Broken lattice symmetry due to strain, results in interesting modifications of the electronic structure of the strained TMDs. The dielectric properties were investigated for all 6 semiconducting TMDs and under 4 different types of strain. Theoretical model explains the out-of-plane dielectric constant almost perfectly for small strains. Further in depth investigation should provide a theoretical model for all the components of the dielectric tensor.

Preliminary results on the effect of strain in the dielectric properties of MoS₂ nanoribbons show that the out-of-plane dielectric constant reduces as the ribbon uniaxially expands (fig.6.1), while the behavior of the in-plane component of the dielectric tensor is more complicated.

Appendix A

| <i>Dacapo</i> | <i>H</i> | <i>H₂</i> | ΔE |
|--------------------|--------------|----------------------|--------------|
| LDA - PerdewZunger | -12.1833 eV | -30.9062 eV | -6.5396 eV |
| GGA - PW91 | -12.5769 eV | -31.7951 eV | -6.6413 eV |
| LDA - VosWilNus | -12.1776 eV | -30.8996 eV | -6.5444 eV |
| VASP | H | H ₂ | ΔE |
| pot-LDA | -0.073826 eV | -6.740073 eV | -6.592421 eV |
| pot-GGA | -0.076616 eV | -6.846612 eV | -6.693380 eV |
| potpaw-LDA | -0.109574 eV | -6.799253 eV | -6.580105 eV |
| potpaw-GGA-PW91-F | -0.690468 eV | -6.916690 eV | -5.535754 eV |
| potpaw-GGA-PBE | -0.116508 eV | -6.871964 eV | -6.638948 eV |

Table 1.1: Hydrogen Results

| Potential | Mo (Mo-pv) | S (S-h) |
|---------------|-------------------|-------------------|
| VASP-PAW-LDA | -0.52eV (-0.42eV) | -0.16eV (-0.48eV) |
| VASP-PAW-PBE | -0.38eV (-0.41eV) | -0.17eV (-1.00eV) |
| VASP-PAW-PW91 | -0.40eV (-0.38eV) | -0.17eV (-3.97eV) |
| GPAW - PBE | -3.85eV | -0.94eV |

Table 1.2: Atomic energies for Mo and S atoms with various potentials and softwares. In the Mo-pv results the semi core p states are treated as valence and in the S-h potentials a very small core radius is used

| Sample | C01 | C02 | C03 | C04 | C05 | C06 | C07 | C08 | C09 | C10 | C11 | C12 |
|--------------------------------------|---------|---------|---------|---------|---------|---------|---------|---------|---------|---------|---------|---------|
| Input Data | | | | | | | | | | | | |
| N | 1000 | 1000 | 1000 | 1000 | 1000 | 1000 | 1000 | 1000 | 1000 | 1000 | 1000 | 1000 |
| a_{init} (Å) | 4.30 | 4.25 | 4.20 | 4.10 | 4.00 | 3.90 | 3.80 | 3.70 | 3.60 | 3.50 | 3.40 | 3.30 |
| ρ_{init} (gr/cm ³) | 2.01 | 2.08 | 2.15 | 2.31 | 2.49 | 2.69 | 2.91 | 3.15 | 3.42 | 3.72 | 4.06 | 4.44 |
| Output Data | | | | | | | | | | | | |
| a_{final} (Å) | 4.18 | 4.12 | 4.11 | 4.01 | 3.95 | 3.87 | 3.82 | 3.76 | 3.72 | 3.66 | 3.65 | 3.62 |
| ρ_{final} (gr/cm ³) | 2.18 | 2.28 | 2.30 | 2.47 | 2.59 | 2.75 | 2.86 | 3.00 | 3.10 | 3.25 | 3.28 | 3.36 |
| Temp. (K) | 300 | 300 | 300 | 300 | 300 | 300 | 300 | 300 | 300 | 300 | 300 | 300 |
| Sp1 (%) | 4.6 | 3.8 | 2.8 | 2.7 | 2.3 | 0.9 | 0.7 | 0.6 | 0.9 | 0.7 | 0.9 | 1.6 |
| Sp2 (%) | 88.8 | 88.0 | 87.8 | 85.4 | 81.2 | 76.7 | 69.3 | 59.5 | 48.9 | 33.4 | 23.3 | 15.5 |
| Sp3 (%) | 6.6 | 8.2 | 9.4 | 11.9 | 16.5 | 22.4 | 30.0 | 39.9 | 50.2 | 65.9 | 75.8 | 82.9 |
| R(A) | 1.46 | 1.46 | 1.45 | 1.45 | 1.46 | 1.47 | 1.47 | 1.49 | 1.50 | 1.52 | 1.53 | 1.54 |
| m.c.n. | 3.02 | 3.044 | 3.066 | 3.092 | 3.138 | 3.213 | 3.291 | 3.391 | 3.481 | 3.644 | 3.731 | 3.785 |
| Bulk modulus(GPa) | 167.37 | 185.71 | 190.55 | 204.12 | 226.87 | 258.14 | 260.87 | 287.04 | 321.21 | 336.47 | 333.16 | 366.21 |
| Total Energy (eV/atom) | -6.9457 | -6.9666 | -6.9573 | -6.9820 | -6.9839 | -6.9778 | -6.9865 | -6.9806 | -6.9233 | -6.9156 | -6.8727 | -6.8368 |

Table 1.3: Summary table for all the a-C Samples

| Samples | A5 | A6 | A7 | A8 | A9 | A10 | A11 | A12 | A12 | A12 |
|--------------------------------------|--------|--------|--------|--------|--------|--------|--------|--------|--------|--------|
| Input Data | | | | | | | | | | |
| d_{init} (nm) | 2.00 | 2.40 | 3.20 | 4.00 | 4.60 | 5.10 | 2.80 | | 3.60 | |
| ρ_{init} (gr/cm ³) | 3.54 | 3.54 | 3.54 | 3.54 | 3.54 | 3.54 | 3.54 | | 3.54 | |
| Nc | 730 | 1346 | 3122 | 5980 | 9082 | 12478 | 0 | 2052 | 0 | 4350 |
| Output(0K) | | | | | | | | | | |
| Nc | 730 | 1346 | 3122 | 5980 | 9082 | 12478 | 2052 | | 4350 | |
| R (A) | 1.555 | 1.550 | 1.545 | 1.545 | 1.545 | 1.545 | 1.545 | | 1.545 | |
| r(A) | 10.03 | 12.26 | 16.18 | 20.09 | 23.09 | 25.67 | 14.06 | | 18.07 | |
| d final (nm) | 2.01 | 2.45 | 3.24 | 4.02 | 4.62 | 5.13 | 5.00 | 2.81 | 2.72 | 3.57 |
| ρ_{final} (gr/cm ³) | 3.44 | 3.48 | 3.51 | 3.51 | 3.51 | 3.51 | 3.51 | | 3.51 | |
| Output(200K) | | | | | | | | | | |
| f simulation (cm ⁻¹) | 205.20 | 174.00 | 142.00 | 110.60 | 110.50 | 110.50 | 110.50 | 110.50 | 157.80 | 126.30 |
| f_{bib} (cm ⁻¹) | 200.08 | 163.69 | 124.06 | 99.90 | 86.91 | 78.17 | 80.33 | 142.69 | 147.60 | 112.36 |
| Dev1 (%) | 2.56 | 6.30 | 14.46 | 10.72 | 27.15 | 21.12 | 21.00 | 17.75 | 6.91 | 12.41 |
| f_{mean} (cm ⁻¹) | 226.97 | 185.69 | 140.74 | 113.32 | 98.59 | 88.68 | 91.13 | 161.87 | 167.45 | 127.46 |
| Dev2 (%) | 9.59 | 6.30 | 0.90 | 2.40 | 12.08 | 6.77 | 6.66 | 3.80 | 2.51 | 0.91 |
| f_{fit} (cm ⁻¹) | 178.04 | 144.88 | 109.80 | 88.41 | 76.92 | 69.19 | 71.10 | 126.29 | 130.64 | 99.44 |
| Dev3 (%) | 15.26 | 20.10 | 29.32 | 25.09 | 43.66 | 36.71 | 33.04 | 24.95 | 20.79 | 27.01 |

Table 1.4: Summary table for all spherical n-D samples. f1 uses 120000m/s as speed of sound in carbon. f2 uses as speed of sound derived mean value(13613m/s) and f3 uses the value obtained from a least square fit(10620m/s).

| Input Data | B09 | B18 | B20 | B21 | B22 | B23 | B24 | B25 | B29 | B30 | B31 |
|------------------------------|-----------|-----------|-----------|-----------|-----------|-----------|-----------|-----------|-----------|-----------|-----------|
| d_{mit} (nm) | 2.03 | 2.50 | 3.00 | 3.50 | 4.00 | 4.50 | 5.00 | 2.50 | 2.03 | 5.50 | 6.00 |
| Cell (nm) | 3.01 | 3.76 | 4.42 | 4.78 | 5.26 | 6.02 | 6.77 | 3.72 | 3.01 | | |
| P_{mit} (gr/cm^3) | 3.45/3.00 | 3.45/3.00 | 3.54/3.20 | 3.54/3.20 | 3.69/3.00 | 3.69/3.00 | 3.69/3.00 | 3.66/3.10 | 3.45/3.00 | 3.69/3.00 | 3.69/3.00 |
| QR (K/ps) | 140 | 140 | 140 | 140 | 140 | 140 | 140 | 140 | 140 | 140 | 140 |
| Temp (K) | 300 | 300 | 300 | 300 | 300 | 300 | 300 | 300 | 300 | 300 | 300 |
| Ntot | 4096 | 8000 | 13824 | 17576 | 21952 | 32768 | 46656 | 8000 | 4096 | 46656 | 54872 |
| $N_{c,mit}$ | 633 | 1231 | 2293 | 3602 | 5011 | 7163 | 9897 | 1291 | 633 | 13079 | 16960 |
| Output (0K) | | | | | | | | | | | |
| Nc | 547 | 1117 | 2653 | 4132 | 5009 | 7056 | 9943 | 1290 | 578 | 13197 | 16922 |
| Na | 3549 | 6883 | 11171 | 13444 | 16943 | 25712 | 36713 | 6710 | 3518 | 33459 | 37950 |
| $r(\text{\AA})$ | 9.25 | 11.74 | 15.57 | 17.99 | 19.32 | 21.71 | 24.26 | 12.27 | 9.37 | 26.58 | 28.87 |
| d_{final} (nm) | 1.85 | 2.35 | 3.11 | 3.60 | 3.86 | 4.34 | 4.85 | 2.45 | 1.87 | 5.32 | 5.77 |
| $1/d_{final}$ (nm^{-1}) | 0.54 | 0.43 | 0.32 | 0.28 | 0.26 | 0.23 | 0.21 | 0.41 | 0.53 | 0.19 | 0.17 |
| L_{base} (Å) | 29.88 | 37.50 | 44.46 | 48.04 | 52.24 | 59.66 | 67.18 | 37.30 | 29.88 | 66.88 | 70.44 |
| ρ_c (gr/cm^3) | 3.29 | 3.28 | 3.35 | 3.38 | 3.31 | 3.28 | 3.31 | 3.32 | 3.35 | 3.35 | 3.35 |
| ρ_a (gr/cm^3) | 3.03 | 2.99 | 3.09 | 3.10 | 3.01 | 3.02 | 3.01 | 3.03 | 3.02 | 3.03 | 3.04 |
| ρ_{final} (gr/cm^3) | 3.06 | 3.02 | 3.14 | 3.16 | 3.07 | 3.08 | 3.07 | 3.07 | 3.06 | 3.11 | 3.13 |
| B(0K)(GPa) | 292.93 | 308.69 | 309.59 | 320.51 | 304.11 | 302.41 | 295.83 | 298.64 | 296.99 | 311.74 | 0.00 |
| Output (300K) | | | | | | | | | | | |
| f_{sim} (cm^{-1}) | 162.40 | 139.39 | 122.30 | 110.63 | 102.26 | 90.16 | 76.65 | 138.02 | 145.75 | 77.00 | 76.00 |
| f_{bb} (cm^{-1}) | 216.93 | 170.88 | 128.89 | 111.55 | 103.89 | 92.44 | 82.72 | 163.50 | 214.21 | 75.51 | 69.50 |
| Dev1 (%) | 25.14 | 18.43 | 5.11 | 0.83 | 1.57 | 2.47 | 7.33 | 15.58 | 31.96 | 1.98 | 9.35 |
| f_{mean} (cm^{-1}) | 246.09 | 193.85 | 146.22 | 126.55 | 117.85 | 104.87 | 93.83 | 185.47 | 243.00 | 85.66 | 78.84 |
| Dev2 (%) | 34.01 | 28.09 | 16.36 | 12.58 | 13.23 | 14.02 | 18.31 | 25.58 | 40.02 | 10.10 | 3.61 |
| f_{fit} (cm^{-1}) | 192.00 | 151.24 | 114.08 | 98.73 | 91.95 | 81.82 | 73.21 | 144.70 | 189.59 | 66.83 | 61.51 |
| Dev3 (%) | 15.42 | 7.84 | 7.21 | 12.05 | 11.22 | 10.20 | 4.70 | 4.62 | 23.12 | 15.22 | 23.55 |
| B(300K) (GPa) | 253.484 | 287.414 | 178.411 | 372.173 | 327.833 | 237.861 | 113.801 | 325.264 | 285.616 | 339.899 | 313.599 |

Table 1.5: Summary table for all n-D-a-C samples.

| Samples | D02 | D03 | D04 | D05 | D06 | D08 | D11 | D12 | D14 | D15 | D19 |
|---------------------------------|---------|---------|---------|---------|---------|---------|---------|---------|---------|---------|---------|
| Input Data | | | | | | | | | | | |
| Cell (Å) | 75.00 | 80.00 | 85.00 | 90.00 | 95.00 | 90.00 | 75.00 | 70.00 | 74.00 | 76.00 | 84.00 |
| Ntot | 66975 | 81061 | 97534 | 117219 | 138443 | 117269 | 66553 | 53723 | 64003 | 69518 | 94435 |
| Output T = 0K | | | | | | | | | | | |
| Na | 66975 | 81061 | 97534 | 117219 | 138443 | 117269 | 66553 | 53723 | 64003 | 69518 | 94435 |
| d (nm) | 3.70 | 3.95 | 4.20 | 4.45 | 4.70 | 4.45 | 3.70 | 3.45 | 3.65 | 3.75 | 4.15 |
| N3 | 9972 | 10362 | | 13203 | 14845 | 13186 | 8950 | 7762 | 8442 | 8947 | 11903 |
| N3 (%) | 14.89 | 12.78 | 0.00 | 11.26 | 10.72 | 11.24 | 13.45 | 14.45 | 13.19 | 12.87 | 12.60 |
| L box (A) | 74.00 | 79.00 | 84.00 | 89.00 | 94.00 | 89.00 | 74.00 | 69.00 | 73.00 | 75.00 | 83.00 |
| Bulk modulus (Gpa) | 298.17 | 279.38 | 294.46 | 302.82 | 307.93 | 305.62 | 291.52 | 282.66 | 290.31 | 298.43 | 294.64 |
| □ total (gr/cm 3) | 3.30 | 3.28 | 3.28 | 3.32 | 3.32 | 3.32 | 3.27 | 3.26 | 3.28 | 3.29 | 3.29 |
| Etot (eV/atom) | -7.1812 | -7.1946 | -7.2018 | -7.2298 | -7.2376 | -7.2311 | -7.1889 | -7.1709 | -7.1917 | -7.1943 | -7.2139 |
| Epot-average (eV/atom) | -7.1820 | -7.1955 | -7.2027 | -7.2307 | -7.2384 | -7.2320 | -7.1897 | -7.1718 | -7.1925 | -7.1950 | -7.2147 |
| Output T = 300K | | | | | | | | | | | |
| f (#4 peak) (cm^{-1}) | | | | 123.40 | 114.64 | | | | | | |
| f (#3 peak) (cm^{-1}) | 146.93 | | 130.43 | 107.13 | 101.17 | | 150.25 | 161.73 | 149.65 | 146.96 | 134.92 |
| f (#2 peak) (cm^{-1}) | 98.51 | 130.32 | 115.54 | 91.98 | 83.66 | 117.27 | 109.72 | 128.35 | 109.30 | 98.53 | 89.99 |
| f (#1 peak) (cm^{-1}) | 59.76 | 61.84 | 60.86 | 75.79 | 55.36 | 88.73 | 62.44 | 68.55 | 55.49 | 67.60 | 56.30 |
| Average Peak freq (cm^{-1}) | 101.73 | 96.08 | 102.28 | 99.58 | 88.71 | 103.00 | 107.47 | 119.54 | 104.81 | 104.36 | 281.21 |
| f_{bib} (cm^{-1}) | 108.47 | 101.60 | 95.56 | 90.19 | 85.39 | 90.19 | 108.47 | 116.33 | 109.96 | 107.02 | 96.71 |
| Dev1 (%) | 6.21 | 5.44 | 7.03 | 10.41 | 3.88 | 14.21 | 0.92 | 2.76 | 4.68 | 2.49 | 190.78 |
| Etot (eV/atom) | -7.1053 | -7.1189 | -7.1258 | -7.1524 | -7.1619 | -7.1549 | -7.1132 | -7.0951 | -7.1139 | -7.1193 | -7.1374 |
| Epot-average (eV/atom) | -7.1433 | -7.1568 | -7.1638 | -7.1902 | -7.2003 | -7.1928 | -7.1512 | -7.1335 | -7.1528 | -7.1566 | -7.1756 |
| EnergyTheory (eV) | -7.1274 | -7.1375 | -7.1465 | -7.1545 | -7.1618 | -7.1545 | -7.1274 | -7.1160 | -7.1252 | -7.1295 | -7.1448 |
| Bulk modulus (Gpa) | 282.49 | 258.54 | 281.49 | 291.99 | 289.86 | 280.48 | 261.06 | 254.47 | 257.44 | 264.46 | 265.52 |

Table 1.6: Summary table for UNCD samples

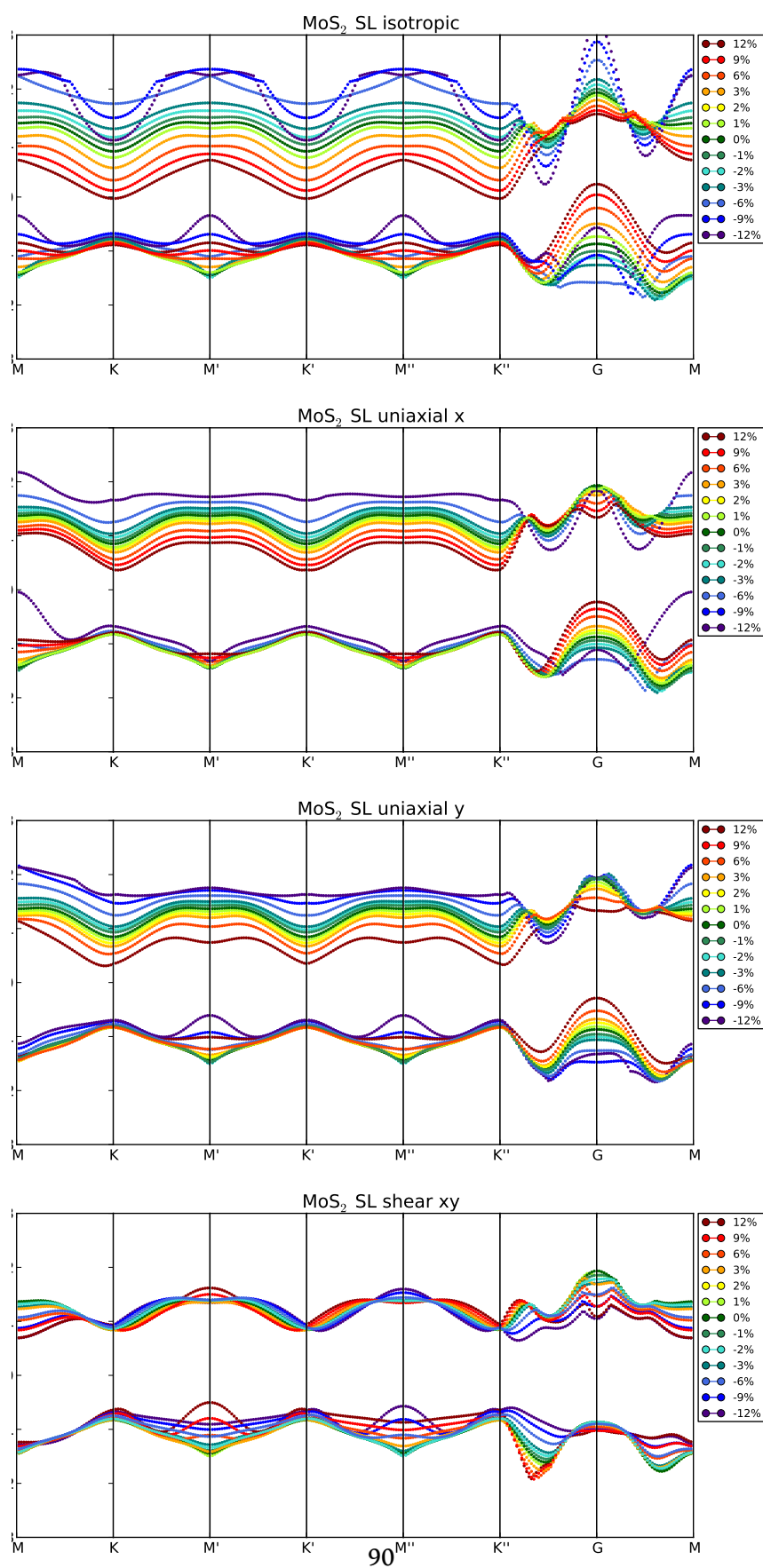


Fig. 1.1: Conduction and Valence bands under strain of the MoS₂ monolayer

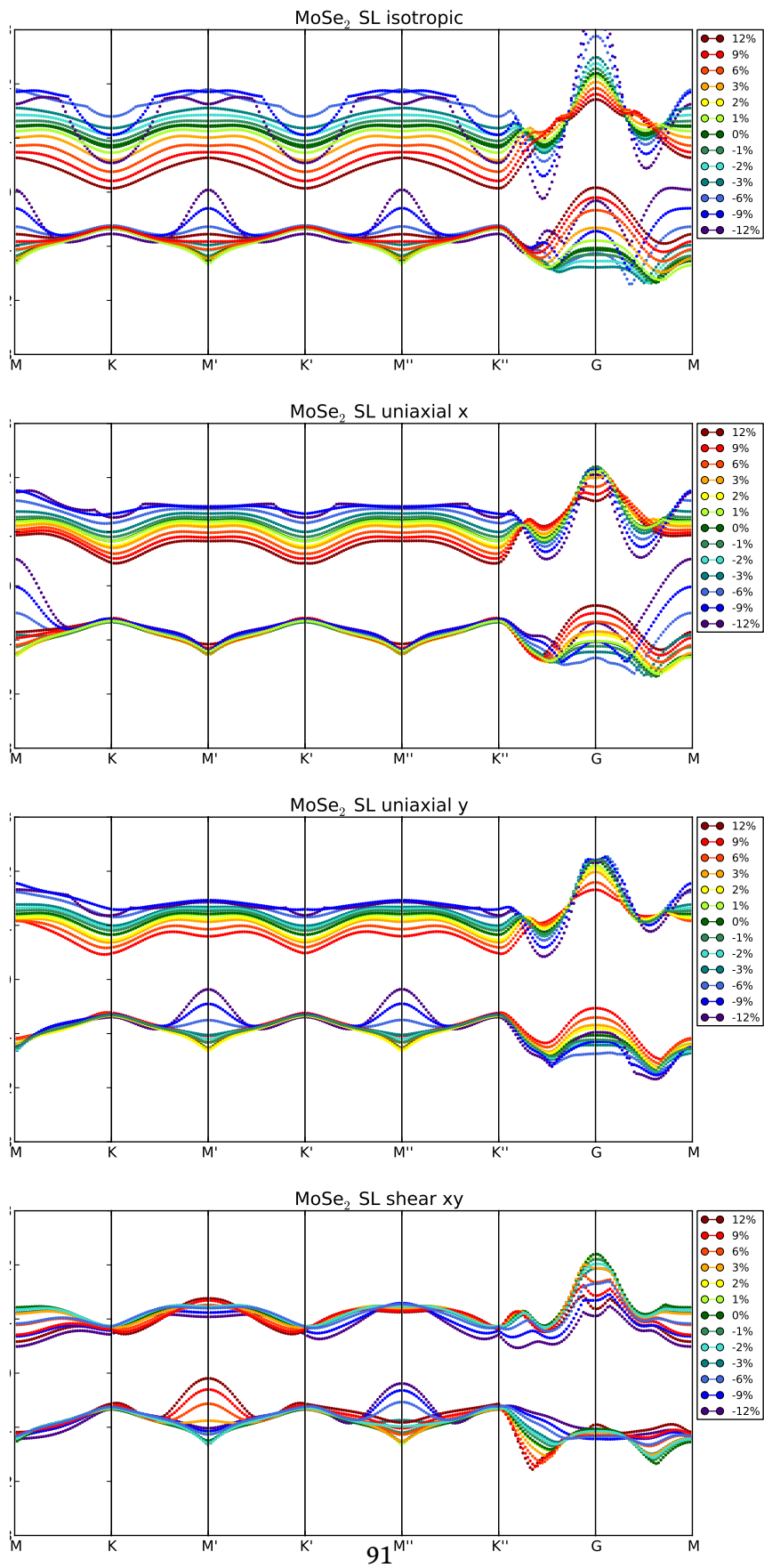


Fig. 1.2: Conduction and Valence bands under strain of the MoSe₂ monolayer

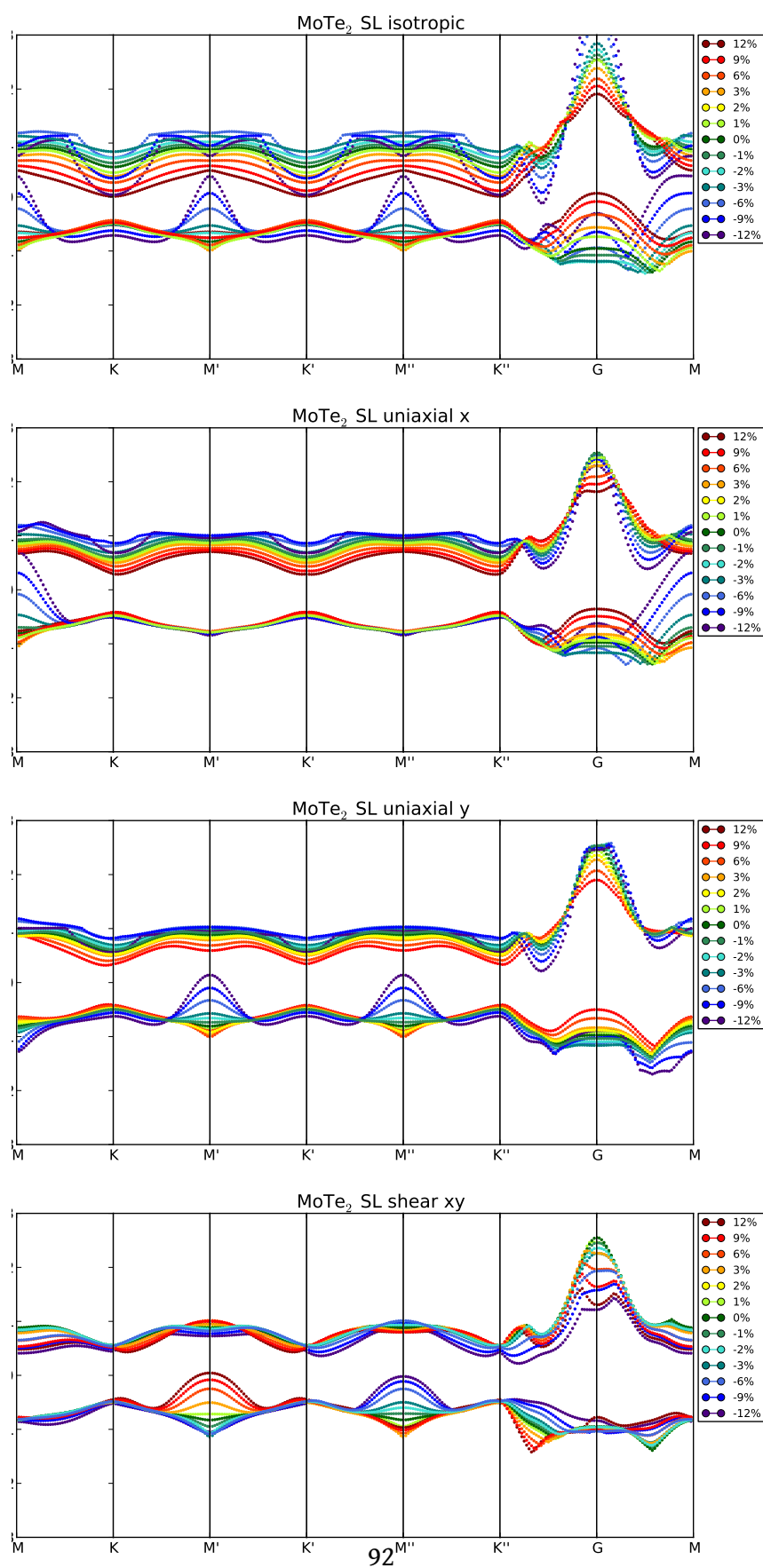


Fig. 1.3: Conduction and Valence bands under strain of the MoTe₂ monolayer

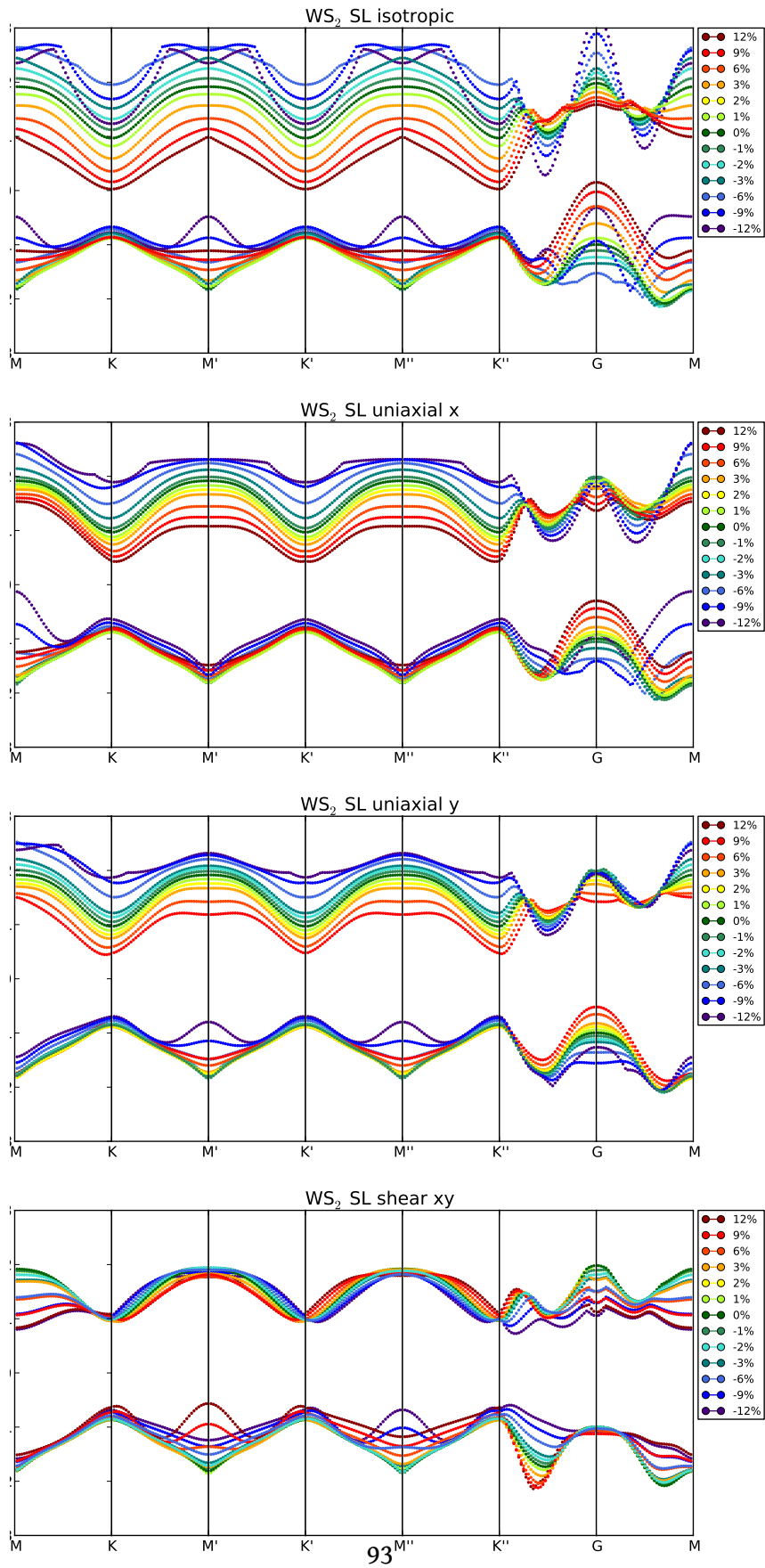


Fig. 1.4: Conduction and Valence bands under strain of the WS₂ monolayer

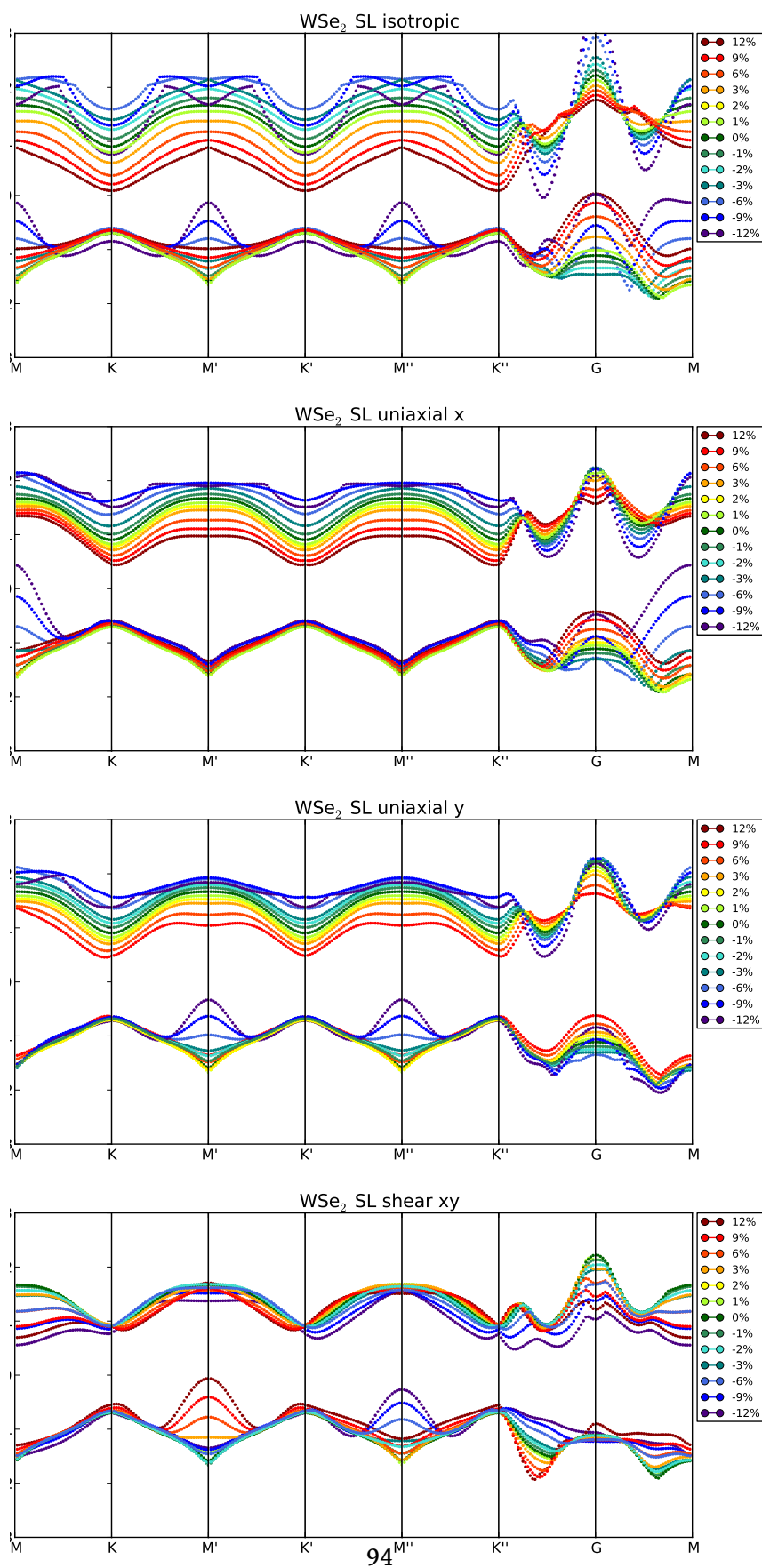


Fig. 1.5: Conduction and Valence bands under strain of the WSe_2 monolayer

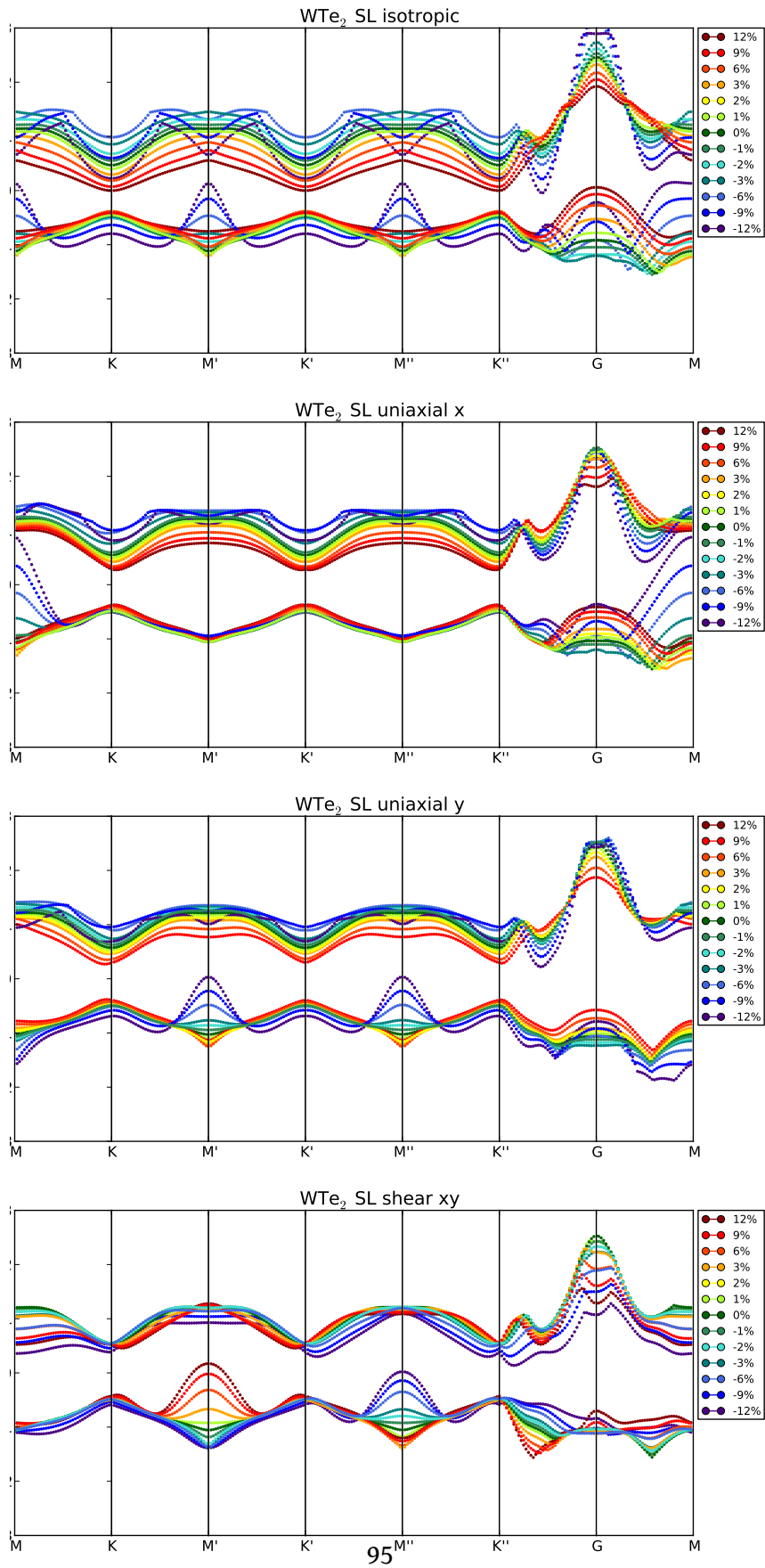


Fig. 1.6: Conduction and Valence bands under strain of the WTe_2 monolayer

| MoS ₂ - bulk | a (Å) | u | c (Å) | M-X (Å) | X-X | $X\dot{M}X$ | E_g (eV) | ϵ^\perp | ϵ^\parallel | E_g -SOC | split@K (meV) |
|--|--------|--------|---------|---------|--------|-------------|------------|------------------|----------------------|------------|---------------|
| GPAW - PBE | 3.198 | 0.635 | 13.717 | 2.428 | 3.155 | 81.0 | 1.34 KG | 12.3 | 7.2 | | |
| VASP - PBE | 3.1898 | 0.6215 | 14.745 | 2.4172 | 3.1312 | 80.73 | 1.4912 KG | - | | | 21.6/145.0 |
| VASP - LDA | 3.1238 | 0.644 | 12.0254 | 2.3839 | 3.1178 | 81.68 | 1.4715 KG | - | | 1.4775 KG | 24.5/148.9 |
| [99] exp | | | | | | | | 17.0 | | | |
| [142] exp | 3.1604 | | | | | 81.0 | | | | | |
| [98] exp | | | | | | | 1.23 | | | | |
| [97] exp | | | | | | | 1.29 | | | | |
| [155] | 3.1600 | | 12.294 | | | | | | | | |
| [146] SIESTA - PBE | | | | 2.41 | 3.17 | 82.41 | 1.06 KG | | | | |
| [103] [150] [111] SIESTA - LDA(o) | 3.13 | | | 2.39 | 3.12 | 81.74 | 0.75 | 12.8 | 8.9 | | |
| [111] SIESTA - PBE(o) | 3.23 | | | 2.45 | 3.18 | 80.84 | 1.05 | | | | |
| [149] | | | | | | | | 16.0 | 10.0 | | |
| [97] LDA | 3.1600 | | 12.294 | | | | | | | | 258 |
| [97] ARPES | | | | | | | | | | | 161±10 |
| MoS ₂ - SL | a (Å) | u | c (Å) | M-X (Å) | X-X | $X\dot{M}X$ | E_g (eV) | ϵ^\perp | ϵ^\parallel | E_g -SOC | split@K (meV) |
| GPAW - PBE | 3.2003 | 0.6352 | 13.717 | 2.428 | 3.149 | 80.9 | 1.6539 KK | 6.1 | 3.6 | | |
| VASP - PBE | 3.1894 | 0.6288 | - | 2.4173 | 3.1321 | 80.76 | 1.6860 KK | - | | 1.6999 KK | -/140.6 |
| VASP - LDA | 3.119 | 0.6306 | - | 2.3812 | 3.1164 | 81.74 | 1.8924 KK | - | | | |
| [146] SIESTA - PBE | | | | 2.41 | 3.17 | 82.41 | 1.70 KK | | | | |
| [90] SIESTA - LSDA | | | | | | | 1.80 | | | | |
| [150] [103] [111] SIESTA - LDA(o) | 3.13 | | | 2.39 | 3.13 | 81.73 | 1.89 | 4.8 | 3.0 | | |
| [118] [111] SIESTA - PBE(o) | 3.23 | | | 2.39 | 3.18 | 80.88 | 1.55 | 4.91 | | | |
| [112] VASP - G ₀ W ₀ | 3.18 | | | | 2.156 | | | 4.26 | | 2.82 KK | 164 |
| [112] VASP - HSE | 3.18 | | | | 2.156 | | | | | 2.05 KK | 193 |
| [112] VASP - PBE | 3.18 | | | | 2.156 | | | | | 1.60 KK | 146 |

Fig. 1.7

| MoSe ₂ - bulk | a (Å) | u | c (Å) | M-X (Å) | X-X | XMX | E _g (eV) | ε [⊥] | ε [∥] | E _g -SOC | split@K (meV) |
|--|--------|--------|---------|---------|--------|-------|---------------------|----------------|----------------|---------------------|---------------|
| MoSe ₂ - SL | a (Å) | u | c (Å) | M-X (Å) | X-X | XMX | E _g (eV) | ε [⊥] | ε [∥] | E _g -SOC | split@K (meV) |
| GPAW - PBE | 3.3018 | | 14.1687 | 2.544 | 3.370 | 83.0 | 1.2364 KL | 14.0 | 8.9910 | | 83/- |
| VASP - PBE | 3.3195 | | 15.500 | 2.4153 | 3.1422 | 82.07 | 1.4137 KL | | | 1.3625 KK | 27/182.8 |
| VASP - LDA | 3.2516 | | 13.1162 | 2.4964 | 3.2910 | 82.47 | 1.3471 KL | | | 1.3343 KK | 32/187.4 |
| [99] exp | | | | | | | | 18.0 | | | |
| [98] exp | | | | | | | | | | 1.09 | |
| [97] exp | | | | | | | | | | 1.10 | |
| [142] exp | 3.288 | | | 2.49 | 3.75 | | | | | | |
| [155] | 3.2990 | | 12.938 | | | | | | | | |
| [158] | 3.288 | | 12.931 | | | | | | | | |
| [103] SIESTA - LDA | 3.30 | | | | | | 0.80 | | | | |
| [111] SIESTA - LDA | | | | | | | | 13.3 | 10.2 | | |
| [149] | | | | | | | | 17.5 | 12.0 | | |
| [97] LDA | 3.299 | | 12.938 | | | | | | | | 294 |
| [97] ARPES | | | | | | | | | | | 175 |
| GPAW - PBE | 3.2020 | 0.6311 | 14.1687 | 2.54 | 3.35 | 82.5 | 1.5114 KK | 7.0 | 4.1154 | | |
| VASP - PBE | 3.3207 | | 15.5203 | 2.5414 | 3.3366 | 82.06 | 1.4531 KK | | | | |
| VASP - LDA | | | | | | | 1.3471 KG | | | | |
| [103] SIESTA - LDA | 3.29 | | | | | | 1.58 | | | | |
| [111] SIESTA - LDA | | | | | | | | 6.9 | 3.8 | | |
| [112] VASP - G ₀ W ₀ | 3.32 | | | | 2.167 | | | 4.74 | | 2.41 KK | 212 |
| [112] VASP - HSE | 3.32 | | | | 2.167 | | | | | 1.75 KK | 261 |
| [112] VASP - PBE | 3.32 | | | | 2.167 | | | | | 1.35 KK | 183 |

Fig. 1.8

| MoTe ₂ - bulk | a (Å) | u | c (Å) | M-X (Å) | X-X | $X\hat{M}X$ | E_g (eV) | ϵ^\perp | ϵ^\parallel | E_g -SOC | split@K (meV) |
|--------------------------|--------|--------|---------|---------|-------|-------------|------------|------------------|----------------------|------------|---------------|
| GPAW - PBE | 3.5939 | 0.6276 | 14.7582 | 2.752 | 3.614 | 82.1 | 0.8713 KL? | 19.2 | 13.047 | | |
| [155] | 3.5220 | | 13.968 | | | | | | | | |
| [99] exp | | | | | | | | 20.0 | | | |
| [97] exp | | | | | | | 1.00 | | | | |
| [142] exp | 3.517 | | | | | | | | | | |
| [140] | 3.519 | 0.621 | 13.97 | | | | | | | | |
| [103] SIESTA - LDA | 3.50 | | | | | | 0.66 | | | | |
| [111] SIESTA - LDA | | | | | | | | 16.9 | 13.0 | | |
| [149] | | | | | | | | 20.5 | 14.0 | | |
| [97] LDA | 3.522 | | 13.968 | | | | | | | | 331 |
| [97] ARPES | | | | | | | | | | | 238 |
| MoTe ₂ - SL | a (Å) | u | c (Å) | M-X (Å) | X-X | $X\hat{M}X$ | E_g (eV) | ϵ^\perp | ϵ^\parallel | E_g -SOC | split@K (meV) |
| GPAW - PBE | 3.5551 | 0.6283 | 14.7582 | 2.728 | 3.593 | 82.4 | 1.0657 KK | 9.1 | 4.8304 | | |
| [103] SIESTA - LDA | 3.49 | | | | | | 1.23 | | | | |
| [111] SIESTA - LDA | | | | | | | | 8.0 | 4.4 | | |
| [112] VASP - G_0W_0 | 3.55 | | | | | | | 5.76 | | 1.77 KK | 266 |
| [112] VASP - HSE | 3.55 | | | | | | | | | 1.30 KK | 344 |
| [112] VASP - PBE | 3.55 | | | | 2.181 | | | | | 0.95 KK | 216 |

Fig. 1.9

| WS ₂ - bulk | a (Å) | u | c (Å) | M-X (Å) | X-X | $X\hat{M}X$ | E_g (eV) | ϵ^\perp | ϵ^\parallel | E_g -SOC | split@K (meV) |
|------------------------|--------|--------|---------|---------|-------|-------------|------------|------------------|----------------------|------------|---------------|
| GPAW - PBE | 3.1968 | 0.6296 | 13.2361 | 2.438 | 3.896 | 81.6 | 1.2943 KL | 11.0 | 7.2038 | | 10.37/- |
| VASP - PBE | 3.1815 | | 12.013 | | | | 1.5135 KG | | | 1.4748 KL | 52/398.5 |
| VASP - LDA | | | | | | | 0.7919 LG | | | 0.8116 LG | 28/476.4 |
| [142] exp | 3.154 | | | | | | | | | | |
| [98] exp | | | | | | | 1.35 | | | | |
| [141] | 3.1530 | 0.6225 | 12.323 | | | | | | | | |
| [103] SIESTA - LDA | 3.14 | | | | | | 0.89 | | | | |
| [111] SIESTA - LDA | | | | | | | | 11.5 | 8.2 | | |
| WS ₂ - SL | a (Å) | u | c (Å) | M-X (Å) | X-X | $X\hat{M}X$ | E_g (eV) | ϵ^\perp | ϵ^\parallel | E_g -SOC | split@K (meV) |
| GPAW - PBE | 3.1938 | 0.6297 | 13.2361 | 2.44 | 3.18 | 81.5 | 1.8537 KK | 5.3 | 3.4 | | |
| VASP - PBE | | | | 2.42 | 3.14 | 81.0 | 1.9113 KL | | | 1.7198 KK | 395.8 |
| VASP - LDA | | | | 2.39 | 3.13 | 81.9 | 1.8767 KL | | | 1.6956 KK | 403.7 |
| [103] SIESTA - LDA | 3.14 | | | | | | 2.05 | | | | |
| [111] SIESTA - LDA | | | | | | | | 4.4 | 2.9 | | |
| [112] VASP - G_0W_0 | 3.19 | | | | | | | 4.13 | | 2.88 KK | 456 |
| [112] VASP - HSE | 3.19 | | | | | | | | | 1.87 KK | 521 |
| [112] VASP - PBE | 3.19 | | | | 2.157 | | | | | 1.56 KK | 425 |

Fig. 1.10

| WSe ₂ - bulk | a (Å) | u | c (Å) | M-X (Å) | X-X | XMX | E _g (eV) | ε [⊥] | ε [∥] | E _g -SOC | split@K (meV) |
|--|--------|--------|---------|---------|--------|-------|---------------------|----------------|----------------|---------------------|---------------|
| [142] exp | 3.286 | | | | | | | | | | |
| [98] exp | | | | | | | 1.20 | | | | |
| GPAW - PBE | 3.3083 | 0.6278 | 13.939 | 2.560 | 3.408 | 83.5 | 1.2087 | 12.25 | 8.5789 | | |
| VASP - PBE | 3.2541 | | 12.8024 | 2.5092 | 3.3266 | 83.04 | | | | | |
| VASP - LDA | 3.3214 | | 15.5196 | 2.5443 | 3.3443 | 82.18 | | | | | |
| [141] | 3.2820 | 0.6211 | 12.960 | | | | | | | | |
| [96] | 3.280 | | 12.950 | | | | | | | | |
| pdf | 3.282 | | 12.937 | | | | | | | | |
| [103] SIESTA - LDA | 3.31 | | | | | | 0.97 | | | | |
| [111] SIESTA - LDA | | | | | | | | 11.7 | 8.7 | | |
| WSe ₂ - SL | a (Å) | u | c (Å) | M-X (Å) | X-X | XMX | E _g (eV) | ε [⊥] | ε [∥] | E _g -SOC | split@K (meV) |
| GPAW - PBE | 3.3105 | 0.6284 | 13.9388 | 2.55 | 3.389 | 83.1 | 1.6280 KK | 6.0 | 3.7988 | | |
| [103] SIESTA - LDA | 3.31 | | | | | | 1.61 | | | | |
| [111] SIESTA - LDA | | | | | | | | 4.5 | 2.9 | | |
| [112] VASP - G ₀ W ₀ | 3.32 | | | | 2.168 | | | 4.63 | | 2.34 KL | 501 |
| [112] VASP - HSE | 3.32 | | | | 2.168 | | | | | 1.68 KK | 586 |
| [112] VASP - PBE | 3.32 | | | | 2.168 | | | | | 1.19 KK | 461 |

Fig. 1.11

| WTe ₂ - bulk | a (Å) | u | c (Å) | M-X (Å) | X-X | XMX | E _g (eV) | ε [⊥] | ε [∥] | E _g -SOC | split@K (meV) |
|-------------------------|--------|--------|---------|---------|-------|------|---------------------|----------------|----------------|---------------------|---------------|
| GPAW - PBE | 3.5897 | 0.6276 | 14.8853 | 3.643 | 4.328 | 82.6 | 0.8754 KL? | 16.7060 | 11.6695 | | |
| [140] | 3.600 | 0.621 | 14.18 | | | | | | | | |
| [103] SIESTA - LDA | 3.51 | | | | | | 0.81 | | | | |
| [111] SIESTA - LDA | | | | | | | | 15.2 | 11.2 | | |
| WTe ₂ - SL | a (Å) | u | c (Å) | M-X (Å) | X-X | XMX | E _g (eV) | ε [⊥] | ε [∥] | E _g -SOC | split@K (meV) |
| GPAW - PBE | 3.5564 | 0.6286 | 14.8853 | 2.736 | 3.616 | 82.7 | 1.0591 KK | 8.2 | 4.5755 | | |
| [103] SIESTA - LDA | 3.51 | | | | | | 1.18 | | | | |
| [111] SIESTA - LDA | | | | | | | | 5.7 | 3.3 | | |

Fig. 1.12

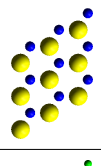
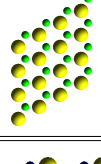
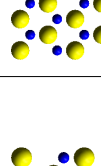
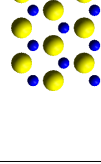
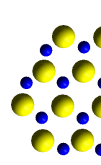
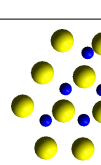
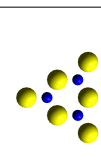
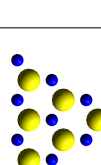
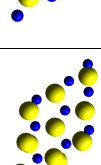
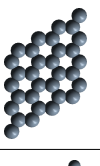
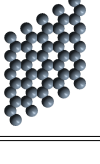
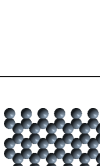
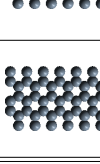
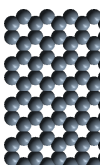

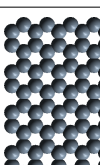
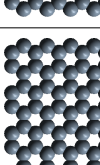
| MoS ₂ structures | 2D | | 1D | | | | 0D | | |
|---|---|---|--|---|---|---|---|---|---|
| | (MoS ₂) ₉ Mo ₉ S ₁₈ | (MoS ₂) ₁₆ Mo ₁₆ S ₃₂ | Rib _{2,3} Mo ₁₂ S ₂₈ | Rib _{3,3} Mo ₁₈ S ₄₂ | F36Hex Mo ₁₂ S ₂₄ | F30Hex Mo ₆ S ₂₄ | F26Tns Mo ₆ S ₂₀ | F22Tmo Mo ₁₀ S ₁₂ | F27Rho Mo ₉ S ₁₈ |
| Images |  |  |  |  |  |  |  |  |  |
| | E_{coh} eq.4.9 (eV/atom) | -7.78 | - | -7.38 | -7.38 | -7.03 | -5.54 | -6.31 | -7.50 |
| H on MoS ₂ ΔE_{ads} eq.4.11eV | p0 | 1.17 | p0 0.45 | | p0 | 0.41 | p0 0.37 | p8 | TBD |
| | | | | p1 | -0.25 | p5 | -0.12 | p9 | TBD |
| | | | | p3 | -0.14 | p6 | -1.36 | p10 | TBD |
| | | | | p2+p3 | 0.20 | p5+p6 | -1.42 | p11 | TBD |
| substrate | C ₃₂ | C ₅₀ | C ₇₂ | C ₉₆ | C ₉₆ | C ₉₆ | C ₉₆ | C ₉₆ | - |
| Images |  |  |  |  |  |  |  |  | |
| | MoS ₂ on Gr E_B (eV) eq. 4.10 | C ₃₂ Mo ₉ S ₁₈ -1.15 | C ₅₀ Mo ₁₆ S ₃₂ -3.65 | C ₇₂ Mo ₁₂ S ₂₈ 3.26 | C ₉₆ Mo ₁₂ S ₂₈ 3.70 | C ₉₆ Mo ₁₂ S ₂₄ -1.26 | C ₉₆ Mo ₆ S ₂₄ | C ₉₆ Mo ₆ S ₂₀ -1.09 | C ₉₆ Mo ₁₀ S ₁₂ -0.08 |
| H on Gr/MoS ₂ ΔE_{ads} (eV) eq.4.11 | | | p1+p2 -0.17 | | p5 | -0.09 | p8 | TBD | |
| | | | p2 -0.31 | | p6 | -1.34 | p9 | TBD | |
| | | | p3 -0.60 | | | | | p10 | TBD |
| | | | p4 -0.89 | | | | | p11 | TBD |

Table 1.7: Summary table for all structures. Position $p0$ of H refers to the site where H is positioned on top of a Sulfur atom in the center of the basal plane of each structure, $p1$ - $p4$ are the positions of H in the quasi-1D ribbons and $p5$ - $p6$ are the positions of H in the Hexagonal flake (fig. 4.9) and $p8$ - $p11$ the positions in the triangular flakes.

Bibliography

- [1] A. C. Dillon, K. M. Jones, T. A. Bekkedahl, C. H. Kiang, D. S. Bethune, M. J. Heben *Storage of hydrogen in single-wall nanotubes* Nature 386, 377 (1997) [↗](#) 2
- [2] S. Orimo, T. Matsushima, H. Fujii, T. Fukunaga, G. Majer *Hydrogen desorption property of mechanically prepared nanostructured graphite* J. Appl. Phys. 90, 1545 (2001) [↗](#) 3
- [3] A. Chambers, C. Park, R.T.K. Baker, N.M. Rodriguez *Hydrogen storage in graphite nanofibers* J. Phys. Chem. B 102, 4253 (1998) [↗](#) 3
- [4] H. Kajiura, K. Kadono, S. Tsutsui, Y. Murakami *Repeatable hydrogen adsorption using nanostructured graphite at room temperature* Appl. Phys. Lett. 82, 1929 (2003) [↗](#) 3
- [5] T. Kiyobayashi, K. Komiyama, N. Takeichi, H. Tanaka, H. Senoh, H.T. Takeshita, N. Kuriyama *Hydrogenation of nanostructured graphite by mechanical grinding under hydrogen atmosphere* Mat. Sci. Eng. B-Solid 108, 134 (2004) [↗](#) 3
- [6] Y.F. Zhao, Y.H. Kim, A.C. Dillon, M.J. Heben, S.B. Zhang *Hydrogen storage in novel organometallic buckyballs* Phys. Rev. Lett. 94,155504 (2005) [↗](#) 3
- [7] P.A. Berseth, A.G. Harter, R. Zidan, A. Blomqvist, C.M. Araujo, R.H. Scheicher, R. Ahuja, P. Jena *Carbon nanomaterials as catalysts for hydrogen uptake and release in NaAlH* Nano Lett., 9 (4), pp 1501–1505 (2009) [↗](#) 3
- [8] Markus J. Buehler *Atomistic Modeling of Materials Failure* Springer US, 2008 [↗](#) 7
- [9] James Morris, Dave Turner, and Kai-Ming Ho *AMES Lab Classical Molecular Dynamics simulation* [↗](#) 8
- [10] S. Plimpton, *Fast Parallel Algorithms for Short-Range Molecular Dynamics* J Comp Phys, 117, 1-19 (1995) [↗](#) 8, 41

BIBLIOGRAPHY

- [11] J. Tersoff *Empirical Interatomic Potential for Carbon, with Applications to Amorphous Carbon* Phys. Rev. Lett. 61, 2879–2882 (1988) [↗](#) 8, 9, 18, 19
- [12] Donald W. Brenner *Empirical potential for hydrocarbons for use in simulating the chemical vapor deposition of diamond films* Phys. Rev. B 42, 9458 (1990) [↗](#) 10
- [13] D. W Brenner, O. A. Shenderova, J. A. Harrison, S. J. Stuart, B. Ni and S. B. Sinnott *A second-generation reactive empirical bond order (REBO) potential energy expression for hydrocarbons* Journal of Physics: Condensed Matter, 14, 4, 783, (2002) [↗](#) 10, 39
- [14] D. S. Sholl & J. A. Steckel *Density Functional Theory: A Practical Introduction* Published by John Wiley & Sons, Inc., Hoboken, New Jersey 12
- [15] P. Hohenberg and W. Kohn *Inhomogeneous Electron Gas* Phys. Rev. B 136, 864 (1964) [↗](#) 12
- [16] W. Kohn and L. J. Sham *Self-Consistent Equations Including Exchange and Correlation Effects* Phys. Rev. 140, A1133 (1965) [↗](#) 12
- [17] J. P. Perdew and A. Zunger *Self-interaction correction to density-functional approximations for many-electron systems* Phys. Rev. B, 23:5048, 1981 [↗](#) 13, 48
- [18] J. P. Perdew, K. Burke, and M. Ernzerhof *Generalized gradient approximation made simple* Phys. Rev. Lett., 77:3865, 1996 ERRATUM:Phys. Rev. Lett., 78:1396, 1997 [↗](#) 13, 48
- [19] Karlheinz Schwarz *Selected Topics in Applications of Quantum Mechanics* [↗](#) 14
- [20] I.N. Remediakis, M. G. Fyta C. Mathioudakis, G. Kopidakis and P. C. Kelires *Structure, Elastic Properties and Strength of Amorphous and Nanocomposite Carbon Diamond and Related Materials*, 16, 1835 (2007) [↗](#) 16
- [21] M. G. Fyta, I. N. Remediakis, and P. C. Kelires *Energetics and stability of nanostructured amorphous carbon* Phys. Rev. B 67, 035423 (2003) [↗](#) 16
- [22] J. Schwan, S. Ulrich, V. Batori, H. Ehrhardt and S. R. P. Silva *Raman spectroscopy on amorphous carbon films* Journal of Applied Physics, 80, 440-447 (1996) [↗](#) 16
- [23] J. Robertson *Diamond-like amorphous carbon* Materials Science and Engineering (R) 37 (2002) [↗](#) 16, 26
- [24] C. Mathioudakis, G. Kopidakis, P. Patsalas, P.C. Kelires *Disorder and optical properties of amorphous carbon* Diamond and Related Materials, 16, 1788 (2007) [↗](#) 16

- [25] S. Osswald, V. N. Mochalin, M. Havel, G. Yushin and Y. Gogotsi *Phonon confinement effects in the Raman spectrum of nanodiamond* Phys. Rev. B 80, 075419 (2009) [↗](#) 17, 36
- [26] Bringma, E. Oran, “The Fast Fourier Transform” [↗](#) 18
- [27] G Kopidakis, C Z Wang, C M Soukoulis and K M Ho *A tight-binding molecular dynamics study of phonon anharmonic effects in diamond and graphite* J. Phys.: Condens. Matter 9, 7071–7080 (1997) [↗](#) 18, 20, 21
- [28] Glen A. Slack and S. F. Bartram *Thermal expansion of some diamond-like crystals* J. Appl. Phys. 46, 89 (1975) [↗](#) 21
- [29] P. K. Schelling and P. Keblinski *Thermal expansion of carbon structures* Phys. Rev. B 68, 035425 (2003) [↗](#) 21
- [30] En-Ping Huang, Eugene Huang, Shu-Cheng Yu, Yen-Hua Chen, Jiann-Shing Lee, Jiann-Neng Fang *High-temperature and pressure Raman spectroscopy of diamond* [↗](#) 21
- [31] Irina Rosenblum, Joan Adler, Simon Brandon *Calculation of thermal properties of diamond from simulated phonon spectra* Computational Materials Science, 12, 9–25 (1998) [↗](#) 19
- [32] C-Diamond: Mechanical Properties, Elastic Constants, Lattice Vibrations [↗](#) 19
- [33] J. C. Angus and C. C. Hayman, *Low-pressure, metastable growth of diamond and “diamondlike” phases* Science, Vol. 241 no. 4868 pp. 913-921 (1988) [↗](#) 20
- [34] Sergey V. Kidalov and Fedor M. Shakhov *Thermal Conductivity of Diamond Composites* Materials, 2, 2467-2495 (2009) [↗](#) 20
- [35] The Engineering Toolbox - Linear Expansion Coefficients [↗](#) 20
- [36] C. Mathioudakis, G. Kopidakis, P. C. Kelires, C. Z. Wang, and K. M. Ho *Physical trends in amorphous carbon: A tight-binding molecular-dynamics study* Phys. Rev. B 70 (2004) [↗](#) 22, 24, 25
- [37] Voyiadjis, G.Z. and Bank, L.C. and Jacobs, L.J. *Mechanics of Materials and Structures* Studies in Applied Mechanics, Elsevier Science, (2013) [↗](#) 24
- [38] A. C. Ferrari and J. Robertson *Interpretation of Raman spectra of disordered and amorphous carbon* Phys. Rev. B 61, 14095–14107 (2000) [↗](#) 25, 26

- [39] X. T. Zhou, Q. Li, F. Y. Meng, I. Bello, C. S. Lee, S. T. Lee and Y. Lifshitz *Manipulation of the equilibrium between diamond growth and renucleation to form a nanodiamond/amorphous carbon composite* Appl. Phys. Lett. **80**, 3307 (2002) [↗](#) 29, 30
- [40] G. Vantarakis, C. Mathioudakis, G. Kopidakis, C. Z. Wang, K. M. Ho, and P. C. Kelires *Interfacial disorder and optoelectronic properties of diamond nanocrystals* Phys. Rev. B **80**, 045307 (2009) [↗](#) 30
- [41] The Engineering Toolbox - Sound Velocity in Solids [↗](#) 31
- [42] Eklund et al. J.M. Holden, R.A. Jishi *Vibration modes of carbon nanotubes; Spectroscopy and theory* Carbon, **33**, no 7, pp 959-972, (1995) [↗](#)
- [43] D. M. Gruen *Nanocrystalline Diamond Films* [↗](#) 38
- [44] CAMP Open Software Project (CamposASE) [↗](#) 38
- [45] S. P. Adiga, V. P. Adiga, R. W. Carpick and D. W. Brenner *Vibrational Properties and Specific Heat of Ultrananocrystalline Diamond: Molecular Dynamics Simulations* J. Phys. Chem. C **115**, 21691-21699 (2011) [↗](#) 38, 39
- [46] Ioannis N. Remediakis, Georgios Kopidakis, Pantelis C. Kelires *Softening of ultrananocrystalline diamond at low grain sizes* Acta Materialia **56**, 5340-5344 (2008) [↗](#) 38, 39
- [47] G. E. Froudakis *Hydrogen interaction with carbon nanotubes: A review of ab initio studies* Phys. Conds. Mat **14** R453 (2002) 41
- [48] G. Kopidakis, C. Z. Wang, C. M. Soukoulis, and K. M. Ho *Hydrogen-induced structural changes in tetrahedral amorphous carbon* Phys. Rev. B **58**, 14106 (1998) [↗](#) 42
- [49] J. D. Benck, T. R. Hellstern, J. Kibsgaard, P. Chakthranont and T. F. Jaramillo *Catalyzing the Hydrogen Evolution Reaction (HER) with Molybdenum Sulfide Nanomaterials* ACS Catal. **2014**, **4**, 3957-3971 [↗](#) 46
- [50] Y. Li, H. Wang, L. Xie, Y. Liang, G. Hong and H. Dai *MoS₂ Nanoparticles Grown on Graphene: An Advanced Catalyst for the Hydrogen Evolution Reaction* J. Am. Chem. Soc., **2011**, **133** (19), pp 7296-7299 [↗](#) 46, 50
- [51] Z.X. Guo, C. Shang, K.F. Aguey-Zinsou *Materials challenges for hydrogen storage* Journal of the European Ceramic Society **28** (2008) 1467-1473 [↗](#) 47
- [52] J. K. Nørskov, T. Bligaard, A. Logadottir, J. R. Kitchin, J. G. Chen, S. Pandelov and U. Stimming *Comment on 'Trends in the Exchange Current for Hydrogen Evolution* Journal

- of The Electrochemical Society, 152 (3) J23 - J26 (2005) [↗](#) Response to "Comment on 'Trends in the Exchange Current for Hydrogen Evolution' J.Electrochem.Soc., 152, J23(2005)" J. K. Nørskov, T. Bligaard, A. Logadottir, J. R. Kitchin, J. G. Chen, S. Pandelov and U. Stimming J. Electrochem. Soc. 2005 volume 153, issue 12, L33 [↗](#) 47, 60
- [53] B. Seo, G. Y. Jung, Y. J. Sa, H. Y. Jeong, J. Y. Cheon, J. H. Lee, H. Y. Kim, J. C. Kim, H. S. Shin, S. K. Kwak, and S. H. Joo *Monolayer-Precision Synthesis of Molybdenum Sulfide Nanoparticles and Their Nanoscale Size Effects in the Hydrogen Evolution Reaction* ACS Nano 20 Mar 2015 [↗](#) 47, 60
- [54] M. Pandey, A. Vojvodic, K. S. Thygesen and K. W. Jacobsen *Two-dimensional Metal Dichalcogenides and Oxides for Hydrogen Evolution: A Computational Screening Approach* J. Phys. Chem. Lett. (Just Accepted) 14 April 2015 [↗](#) 47
- [55] M. V. Bollinger, K. W. Jacobsen, and J. K. Nørskov *Atomic and electronic structure of MoS₂ nanoparticles* Phys. Rev. B 67, 085410 (2003) [↗](#) 47, 49, 54, 56
- [56] Mark A. Lukowski, Andrew S. Daniel, Fei Meng, Audrey Forticaux, Linsen Li, and Song Jin *Enhanced Hydrogen Evolution Catalysis from Chemically Exfoliated Metallic MoS₂ Nanosheets* J. Am. Chem. Soc., 135 (28), pp 10274–10277 (2013) [↗](#) 47
- [57] Damien Voiry, Maryam Salehi, Rafael Silva, Takeshi Fujita, Mingwei Chen, Tewodros Asefa, Vivek B. Shenoy, Goki Eda, and Manish Chhowalla *Conducting MoS₂ Nanosheets as Catalysts for Hydrogen Evolution Reaction* Nano Lett., 13 (12), pp 6222–6227 (2013) [↗](#) 47
- [58] G. Kresse and J. Hafner *Ab initio molecular dynamics for liquid metals* Phys. Rev. B, 47:558, 1993 48
- [59] G. Kresse and J. Hafner *Ab initio molecular-dynamics simulation of the liquid-metal-amorphous-semiconductor transition in germanium* Phys. Rev. B, 49:14251, 1994
- [60] G. Kresse and J. Furthmüller *Efficiency of ab-initio total energy calculations for metals and semiconductors using a plane-wave basis set* Comput. Mat. Sci., 6:15, 1996
- [61] G. Kresse and J. Furthmüller *Efficient iterative schemes for ab initio total-energy calculations using a plane-wave basis set* Phys. Rev. B, 54:11169, 1996 48
- [62] P. E. Blochl *Projector augmented-wave method* Phys. Rev. B, 50:17953, 1994 48
- [63] G. Kresse and D. Joubert *From ultrasoft pseudopotentials to the projector augmented-wave method* Phys. Rev. B, 59:1758, 1999 48

- [64] Peter E. Blöchl, O. Jepsen, and O. K. Andersen *Improved tetrahedron method for Brillouin-zone integration* Phys. Rev. B 49, 16223 – Published 15 June 1994 [↗](#) 48
- [65] Xiaofei Liu, Tao Xu, Xing Wu, Zhuhua Zhang, Jin Yu, Hao Qiu, Jin-Hua Hong, Chuan-Hong Jin, Ji-Xue Li, Xin-Ran Wang, Li-Tao Sun & Wanlin Guo *Top-down fabrication of sub-nanometre semiconducting nanoribbons derived from molybdenum disulfide sheets* Nature Communications, 4, 1776 (2013) [↗](#) 49
- [66] B. Sachs, L. Britnell, T.O. Wehling, A. Eckmann, R. Jalil, B.D. Belle, J. Lichtenstein, M.I. Katsnelson, K.S. Novoselov *Doping Mechanisms in Graphene-MoS₂ Hybrids* [↗](#) 50, 52
- [67] Charlie Tsai, Frank Abild-Pedersen, and Jens K. Nørskov *Tuning the MoS₂ Edge-Site Activity for Hydrogen Evolution via Support Interactions* Nano Lett., 14 (3), pp 1381–1387 (2014) [↗](#) 50
- [68] Yandong Ma, Ying Dai, Meng Guo, Chengwang Niu and Baibiao Huang *Graphene adhesion on MoS₂ monolayer: An ab initio study* Nanoscale, 3, 3883–3887, (2011) [↗](#) 50, 52
- [69] S. H. Choi, Y. N. Ko, J.-K. Lee, and Y. C. Kang *3D MoS₂-Graphene Microspheres Consisting of Multiple Nanospheres with Superior Sodium Ion Storage Properties* Adv. Funct. Mater., 25: 1780–1788 (2015) [↗](#) 50
- [70] Z. Tan, H. Tian, T. Feng, L. Zhao, D. Xie, Y. Yang, L. Xiao, J. Wang, T.-L. Ren and J. Xu *A small-signal generator based on a multi-layer graphene/molybdenum disulfide heterojunction* Applied Physics Letters 103, 263506 (2013) [↗](#) 50
- [71] Marco Bernardi, Maurizia Palummo, and Jeffrey C. Grossman *Extraordinary Sunlight Absorption and One Nanometer Thick Photovoltaics Using Two-Dimensional Monolayer Materials* Nano Lett., 2013, 13 (8), pp 3664–3670 [↗](#) 50
- [72] Y. Shi, W. Zhou, A.-Y. Lu, W. Fang, Y.-H. Lee, A. L. Hsu, S. M. Kim, K. K. Kim, H. Y. Yang, L.-J. Li, J.-C. Idrobo, and J. Kong *van der Waals Epitaxy of MoS₂ Layers Using Graphene As Growth Templates* Nano Lett., 12 (6), pp 2784–2791 (2012) [↗](#) 50
- [73] Xiaosi Zhou, Li-Jun Wan and Yu-Guo Guo *Synthesis of MoS₂ nanosheet-graphene nanosheet hybrid materials for stable lithium storage* Chem. Commun., 2013, 49, 1838 [↗](#) 50
- [74] S. Bertolazzi, D. Krasnozhan, and A. Kis *Nonvolatile Memory Cells Based on MoS₂/Graphene Heterostructures* ACS Nano, 2013, 7 (4), pp 3246–3252 [↗](#) 50

- [75] Fan Yang, Dehui Deng, Xiulian Pan, Qiang Fu and Xinhe Bao *Understanding nano effects in catalysis* National Science Review (2015): nww024 [↗](#) 50
- [76] R. M. Yunus, H. Endo, M. Tsuji and H. Ago *Vertical Heterostructure of MoS₂ and Graphene Nanoribbons by Two Step Chemical Vapor Deposition for High Gain Photodetectors* Phys. Chem. Chem. Phys., 17, 25210-25215 (2015) [↗](#) 50, 52
- [77] Hannu-Pekka Komsa and Arkady V. Krasheninnikov *Electronic structures and optical properties of realistic transition metal dichalcogenide heterostructures from first principles* Phys. Rev. B 88, 085318 – Published 23 August 2013 [↗](#) 52
- [78] Daphne Davelou, Georgios Kopidakis, George Kioseoglou, Ioannis N. Remediakis *MoS₂ nanostructures: Semiconductors with metallic edges* D. Davelou et al. / Solid State Communications [↗](#) 52
- [79] H. R. Gutiérrez, N. Perea-López, A. L. Elías, A. Berkdemir, B. Wang, R. Lv, F. López-Urías, V. H. Crespi, H. Terrones, and M. Terrones *Extraordinary Room-Temperature Photoluminescence in Triangular WS₂ Monolayers* Nano Lett., 2013, 13 (8), pp 3447–3454 [↗](#) 54, 65
- [80] Y. Yan, B. Y. Xia, Z. Xu and X. Wang *Recent Development of Molybdenum Sulfides as Advanced Electrocatalysts for Hydrogen Evolution Reaction* [↗](#) 54
- [81] Jakob Kibsgaard, Jeppe V. Lauritsen, Erik Lægsgaard, Bjerne S. Clausen, Henrik Topsøe, and F. Besenbacher *Cluster-Support Interactions and Morphology of MoS₂ Nanoclusters in a Graphite-Supported Hydrotreating Model Catalyst* J. Am. Chem. Soc. 2006, 128, 13950-13958 [↗](#) 54
- [82] Y. Huang, J. Wu, X. Xu, Y. Ho, G. Ni, Q. Zou, G. Kok, W. Koon, W. Z, A. H. Castro Neto, G. Eda, C. Shen and B. Özyilmaz, *An innovative way of etching MoS₂: Characterization and mechanistic investigation* Nano Research, Vol 6, Issue 3, pp 200-207 (2013) [↗](#) 54
- [83] K. S. Novoselov, A. K. Geim, S. V. Morozov, D. Jiang, Y. Zhang, S. V. Dubonos, I. V. Grigorieva, A. A. Firsov *Electric Field Effects in Atomically Thin Carbon Films* Science 306 (5696): 666-669 (2004) [↗](#) 63
- [84] Changgu Lee, Hugen Yan, Louis E. Brus, Tony F. Heinz, James Hone and Sunmin Ryu *Anomalous Lattice Vibrations of Single- and Few-Layer MoS₂* ACS Nano, 2010, 4 (5), pp 2695–2700 [↗](#) 63
- [85] Kin Fai Mak, Changgu Lee, James Hone, Jie Shan, and Tony F. Heinz *Atomically Thin MoS₂ : A New Direct-Gap Semiconductor* Phys. Rev. Lett. 105, 136806 (2010) [↗](#) 63, 65

- [86] Andrea Splendiani, Liang Sun, Yuanbo Zhang, Tianshu Li, Jonghwan Kim, Chi-Yung Chim, Giulia Galli, and Feng Wang *Emerging Photoluminescence in Monolayer MoS₂* Nano Lett. 10, 1271–1275 (2010) [↗](#) 63, 65
- [87] Emilio Scalise, Michel Houssa, Geoffrey Pourtois, Valery Afanas'ev, Andre Stesmans *Strain-induced semiconductor to metal transition in the two-dimensional honeycomb structure of MoS₂* Nano Research, Vol. 5, Issue 1, pp 43-48, (2012) [↗](#) 63, 65
- [88] Eugene S. Kadantsev, Pawel Hawrylak *Electronic structure of a single MoS₂ monolayer* Solid State Communications, 152, 909–913 (2012) [↗](#) 64
- [89] G. Kioseoglou, A. T. Hanbicki, M. Currie, A. L. Friedman, D. Gunlycke and B. T. Jonker *Valley polarization and intervalley scattering in monolayer MoS₂* Appl. Phys. Lett. 101, 221907 (2012) [↗](#) 64
- [90] A. R. Botello-Méndez, F. López-Urías, M. Terrones and H. Terrones *Metallic and ferromagnetic edges in molybdenum disulfide nanoribbons* Nanotechnology, 20, 325703 (2009) [↗](#) 64, 96
- [91] Antonis N. Andriotis & Madhu Menon *Tunable magnetic properties of transition metal doped MoS₂* Phys. Rev. B 90, 125304 (2014) [↗](#) 64
- [92] A. Klein, S. Tiefenbacher, V. Eyert, C. Pettenkofer, and W. Jaegermann *Electronic band structure of single-crystal and single-layer WS₂: Influence of interlayer van der Waals interactions* Phys. Rev. B 64, 205416 (2001) [↗](#) 64
- [93] Ziliang Ye, Ting Cao, Kevin O'Brien, Hanyu Zhu, Xiaobo Yin, Yuan Wang, Steven G. Louie & Xiang Zhang *Probing excitonic dark states in single-layer tungsten disulfide* Nature 513, 214–218 (11 September 2014) [↗](#) 64
- [94] Tawinan Cheiwchanamngij and Walter R. L. Lambrecht *Quasiparticle band structure calculation of monolayer, bilayer, and bulk MoS₂* Phys. Rev. B, 85, 205302 (2012) [↗](#) 64, 65
- [95] P. A. Lee *Optical and Electronic Properties* Physics and Chemistry of materials with Layered Structures vol. 4 64, 69
- [96] R. Coehoorn, C. Haas, J. Dijkstra, C. J. F. Flipse, R. A. de Groot, and A. Wold *Electronic structure of MoSe₂, MoS₂, and WSe₂. I. Band-structure calculations and photoelectron spectroscopy* Phys. Rev. B 35, 6195 (1987) [↗](#) 64, 99
- [97] Th. Böker, R. Severin, A. Müller, C. Janowitz, R. Manzke, D. Voß, P. Krüger, A. Mazur, and J. Pollmann *Band structure of MoS₂, MoSe₂, and □-MoTe₂: Angle-resolved*

- photoelectron spectroscopy and ab initio calculations* Phys. Rev. B 64, 235305 (2001) [↗](#) 65, 96, 97, 98
- [98] K. K. Kam , B. A. Parkinson *Detailed photocurrent spectroscopy of the semiconducting group VIB transition metal dichalcogenides* J. Phys. Chem., 1982, 86 (4), pp 463–467 [↗](#) 65, 96, 97, 98, 99
- [99] R Beal and H P Hughes *Kramers-Kronig analysis of the reflectivity spectra of 2H-MoS₂, 2H-MoSe₂ and 2H-MoTe₂* J. Phys. C: Solid State Phys. 12 881 (1979) [↗](#) 65, 96, 97, 98
- [100] A R Beal, W Y Liang and H P Hughes *Kramers-Kronig analysis of the reflectivity spectra of 3R-WS₂ and 2H-WSe₂* J. Phys. C: Solid State Phys. 9 2449 (1976) [↗](#) 65
- [101] J. N. Coleman, M. Lotya, A. O'Neill, S. D. Bergin, P. J. King, U. Khan, K. Young, A. Gaucher, S. De, R. J. Smith, I. V. Shvets, S. K. Arora, G. Stanton, H.-Y. Kim, K. Lee, G. T. Kim, G. S. Duesberg, T. Hallam, J. J. Boland, J. J. Wang, J. F. Donegan, J. C. Grunlan, G. Moriarty, A. Shmeliov, R. J. Nicholls, J. M. Perkins, E. M. Grieveson, K. Theuwissen, D. W. McComb, P. D. Nellist, V. Nicolosi *Two-Dimensional Nanosheets Produced by Liquid Exfoliation of Layered Materials* Science, 331, 568 (2011) [↗](#) 65
- [102] Won Seok Yun, S. W. Han, Soon Cheol Hong, In Gee Kim, and J. D. Lee *Thickness and strain effects on electronic structures of transition metal dichalcogenides: 2H-M X 2 semiconductors (M = Mo, W; X = S, Se, Te)* Phys.Rev. B 85, 033305 (2012) [↗](#) 65, 69
- [103] A. Kumar and P.K. Ahluwalia *Electronic structure of transition metal dichalcogenides monolayers 1H-MX₂ (M = Mo, W; X = S, Se, Te) from ab-initio theory: new direct band gap semiconductors* Eur. Phys. J. B (2012) 85: 186 [↗](#) 65, 96, 97, 98, 99
- [104] Tianshu Li *Ideal strength and phonon instability in single-layer MoS₂* Phys. Rev. B 85, 235407 (2012) [↗](#) 65
- [105] Diana Y. Qiu, Felipe H. da Jornada, and Steven G. Louie *Optical Spectrum of MoS₂ : Many-Body Effects and Diversity of Exciton States* Phys. Rev. Lett. 111, 216805 (2013) [↗](#) 65
- [106] Yunguo Li, Yan-ling Li, Carlos Moyses Araujo, Wei Luo and Rajeev Ahujaa *Single-layer MoS₂ as efficient photocatalyst* Catal. Sci. Technol., 3, 2214-2220 (2013) [↗](#) 65, 69
- [107] C. Ataca and S. Ciraci *Dissociation of H₂ O at the vacancies of single-layer MoS₂* Phys. Rev. B 85, 195410 (2012) [↗](#) 65
- [108] C. Ataca and S. Ciraci *Functionalization of Single-Layer MoS₂ Honeycomb Structures* J. Phys. Chem. C 115, 13303–13311 (2011) [↗](#) 65

- [109] M. Salmani-Jelodar *Single layer MoS₂ band structure and transport* Semiconductor Device Research Symposium (ISDRS), 2011 [↗](#) 65
- [110] Falco Hüser, Thomas Olsen, and Kristian S. Thygesen *How dielectric screening in two-dimensional crystals affects the convergence of excited-state calculations: Monolayer MoS₂* Phys. Rev. B 88, 245309 (2013) [↗](#) 67
- [111] Ashok Kumar, P.K. Ahluwalia *Tunable dielectric response of transition metals dichalcogenides MX₂ (M=Mo, W; X=S, Se, Te): Effect of quantum confinement* Physica B 407 (2012) 4627–4634 [↗](#) 67, 96, 97, 98, 99
- [112] Ashwin Ramasubramaniam *Large excitonic effects in monolayers of molybdenum and tungsten dichalcogenides* Phys. Rev. B, 86, 115409 (2012) [↗](#) 67, 96, 97, 98, 99
- [113] Jinyang Xi, Tianqi Zhao, Dong Wang, and Zhigang Shuai *Tunable Electronic Properties of Two-Dimensional Transition Metal Dichalcogenide Alloys: A First-Principles Prediction* J. Phys. Chem. Lett., 2014, 5 (2), pp 285–291 [↗](#) 69
- [114] Lu,P. and Wu,X. and Guo,W. and Zeng,X. C. "Strain-dependent electronic and magnetic properties of MoS₂ monolayer, bilayer, nanoribbons and nanotubes", Phys. Chem. Chem. Phys., 14,13035-13040, (2012) [↗](#) 69
- [115] Priya Johari and Vivek B. Shenoy *Tuning the Electronic Properties of Semiconducting Transition Metal Dichalcogenides by Applying Mechanical Strains* ACS Nano, 2012, 6 (6), pp 5449–5456 [↗](#) 69, 75
- [116] Qu Yue, Jun Kang, Zhengzheng Shao, Xueao Zhang, Shengli Chang, Guang Wang, Shiqiao Qin, Jingbo Li *Mechanical and electronic properties of monolayer MoS₂ under elastic strain* Physics Letters A 376 (2012) 1166–1170 [↗](#) 69
- [117] A. K. Geim & I. V. Grigorieva *Van der Waals heterostructures* Nature 499, 419–425 (25 July 2013) [↗](#) 69
- [118] Ashok Kumar, P.K. Ahluwalia *Mechanical strain dependent electronic and dielectric properties of two-dimensional honeycomb structures of MoX₂ (X= S, Se, Te)* Physica B 419 (2013) 66–75 [↗](#) 69, 96
- [119] Y.M. Shkel and D.J. Klingenberg *A continuum approach to electrorheology* Journal of Rheology 43, 1307 (1999) [↗](#) 69
- [120] J. J. Mortensen, L. B. Hansen , and K. W. Jacobsen *Real-space grid implementation of the projector augmented wave method* Physical Review B, Vol. 71, 035109, 2005 [↗](#) 69

-
- [121] J. Enkovaara, C. Rostgaard, J. J. Mortensen et al. *Electronic structure calculations with GPAW: a real-space implementation of the projector augmented-wave method* 2010 J. Phys.: Condens. Matter 22 253202 [↗](#) 69
- [122] John P. Perdew, Kieron Burke, and Matthias Ernzerhof *Generalized Gradient Approximation Made Simple* Phys. Rev. Lett. 77, 3865 (1996) [↗](#) 69
- [123] Jun Yan, Jens. J. Mortensen, Karsten W. Jacobsen, and Kristian S. Thygesen *Linear density response function in the projector augmented wave method: Applications to solids, surfaces, and interfaces* Phys. Rev. B 83, 245122 (2011) [↗](#) 70
- [124] Martin H. Sadd *Elasticity Theory Applications and Numerics* 70
- [125] Simone Bertolazzi, Jacopo Brivio and Andras Kis *Stretching and Breaking of Ultrathin MoS₂* ACS Nano, 2011, 5 (12), pp 9703–9709 [↗](#) 71
- [126] Andres Castellanos-Gomez, Menno Poot¹, Gary A Steele, Herre SJ van der Zant, Nicolás Agrait and Gabino Rubio-Bollinger *Mechanical properties of freely suspended semiconducting graphene-like layers based on MoS₂* Nanoscale Research Letters 2012, 7:233 [↗](#) 72
- [127] Simplex Algorithm [↗](#) 72
- [128] Y. Wang, C. Cong, W. Yang, J. Shang, N. Peimyoo, Y. Chen, J. Kang, J. Wang, W. Huang, T. Yu *Strain-induced direct-indirect bandgap transition and phonon modulation in monolayer WS₂* Nano Research, 8, 8, 1998-0124, (2015) [↗](#) 77
- [129] L D Landau, J. S. Bell, M. J. Kearsley, L. P. Pitaevskii, E.M. Lifshitz, J. B. Sykes *Electrodynamics of Continuous Media* Volume 8, 2nd ed., Elsevier, 1984 78
- [130] H. Young Lee, Y. Peng and Y. M. Shkel *Strain-dielectric response of dielectrics as foundation for electrostriction stresses* Journal of Applied Physics 98, 074104 (2005) [↗](#) 78
- [131] Stratton Julius Adams *Electromagnetic Theory* McGraw-Hill, New York, 1941 78
- [132] Hendrik J. Monkhorst and James D. Pack *Special points for Brillouin-zone integrations* Phys. Rev. B 13, 5188 - Published 15 June 1976 [↗](#)
- [133] Charlie Tsai, Karen Chan, Jens K. Nørskov, Frank Abild-Pedersen *Theoretical insights into the hydrogen evolution activity of layered transition metal dichalcogenides* Surf. Sci. (2015) [↗](#)
- [134] U. Stephan and M. Haase *A molecular dynamics study and the electronic properties of amorphous carbon using the Tersoff potential* [↗](#)

BIBLIOGRAPHY

- [135] F. Liu, Q.H. Tang, B.S. Shang and T.C. Wang *Simple optimized Brenner potential for thermodynamic properties of diamond* Philosophical Magazine 2011, 1–16, iFirst [↗](#)
- [136] Z.D. Sha, P.S. Branicio, V. Sorkin, Q.X. Pei, Y.W. Zhang *Effects of grain size and temperature on mechanical and failure properties of ultrananocrystalline diamond* [↗](#)
- [137] Maria G. Fyta *Theoretical investigation of the stability and mechanical properties of nanostructured amorphous carbon* Doctoral Dissertation [↗](#)
- [138] Lucien Saviot, Caleb H. Netting, Daniel B. Murray, Stéphane Rols, Alain Mermet, Anne-Laure Papa, Catherine Pighini, Daniel Aymes and Nadine Millot *Inelastic neutron scattering due to acoustic vibrations confined in nanoparticles: Theory and experiment* Phys. Rev. B 78, 245426 (2008) [↗](#)
- [139] Amin Azizi, Sarah Eichfeld, Gayle Geschwind, Kehao Zhang, Bin Jiang, Debangshu Mukherjee, Lorraine Hossain, Aleksander F. Piasecki, Bernd Kabius, Joshua A. Robinson, and Nasim Alem *Freestanding van der Waals Heterostructures of Graphene and Transition Metal Dichalcogenides* ACS Nano, 9 (5), pp 4882–4890 (2015) [↗](#)
- [140] W. G. Dawson and D. W. Bullett *Electronic structure and crystallography of MoTe₂ and WTe₂* J. Phys. C: Solid State Phys. 20 (1987) [↗](#) 98, 99
- [141] W.J. Schutte, J.L. De Boer, F. Jellinek *Crystal structures of tungsten disulfide and diselenide* Journal of Solid State Chemistry, Vol 70, Issue 2, 207–209 (1987) [↗](#) 98, 99
- [142] J.A. Wilson & A.D. Yoffe *The transition metal dichalcogenides discussion and interpretation of the observed optical, electrical and structural properties* Advances in Physics, 18:73, 193–335, (1969) [↗](#) 96, 97, 98, 99
- [143] Elton J. G. Santos and Efthimios Kaxiras *Electrically Driven Tuning of the Dielectric Constant in MoS₂ Layers* ACS Nano, 2013, 7 (12), pp 10741–10746 [↗](#)
- [144] Kin Fai Mak, Changgu Lee, James Hone, Jie Shan, and Tony F. Heinz *Atomically Thin MoS₂ : A New Direct-Gap Semiconductor* Phys. Rev. Lett. 105, 136806 (2010) [↗](#)
- [145] David R. Penn *Wave-Number-Dependent Dielectric Function of Semiconductors* Phys. Rev. 128, 2093 – Published 1 December 1962 [↗](#)
- [146] H. S. S. Ramakrishna Matte, A. Gomathi, Arun K. Manna, Dattatray J. Late, Ranjan Datta, Swapan K. Pati, and C. N. R. Rao *MoS₂ and WS₂ Analogues of Graphene* Angew. Chem. Int. Ed. 2010, 49, 4059 –4062 [↗](#) 96

- [147] K. Zeppenfeld *Electron energy losses and optical anisotropy of MoS₂ single crystals* Optics Communications, Vol 1, Issue 8, March 1970, Pages 377-378 [↗](#)
- [148] Eugene Wai Keong Koh, Cheng Hsin Chiu, Yao Kun Lim, Yong-Wei Zhang, Hui Pan *Hydrogen adsorption on and diffusion through MoS₂ monolayer: First-principles study* [↗](#)
- [149] Ali Hussain Reshak and Sushil Auluck *Band structure and optical response of 2H-MoX₂ compounds (X = S, Se, and Te)* Phys. Rev. B 71, 155114 (2005) [↗](#) 96, 97, 98
- [150] Ashok Kumar, P.K. Ahluwalia *A first principle Comparative study of electronic and optical properties of 1H-MoS₂ and 2H-MoS₂* Materials Chemistry and Physics 135 (2012) 755e761 [↗](#) 96
- [151] Ashok Kumar, P.K. Ahluwalia *Electronic transport and dielectric properties of low-dimensional structures of layered transition metal dichalcogenides* Journal of Alloys and Compounds 587 (2014) 459-467 [↗](#)
- [152] Qing Hua Wang, Kouros Kalantar-Zadeh, Andras Kis, Jonathan N. Coleman & Michael S. Strano *Electronics and optoelectronics of two-dimensional transition metal dichalcogenides* Nature Nanotechnology 7, 699-712 (2012) [↗](#)
- [153] Hongliang Shi, Hui Pan, Yong-Wei Zhang and Boris I. Yakobson *Quasiparticle band structures and optical properties of strained monolayer MoS₂ and WS₂* Phys.Rev. B 87, 155304 (2013) [↗](#)
- [154] Hong Jiang *Electronic Band Structures of Molybdenum and Tungsten Dichalcogenides by the GW Approach* J. Phys. Chem. C, 2012, 116 (14), pp 7664-7671 [↗](#)
- [155] *Gmelin Handbook of Inorganic and Organometallic Chemistry* Springer-Verlag, Berlin, 1995, Chap. Mo Suppl. Vol. B 7,8,9, p. 16 96, 97, 98
- [156] S. W. Han, Hyuksang Kwon, Seong Keun Kim, Sunmin Ryu, Won Seok Yun, D. H. Kim, J. H. Hwang, J.-S. Kang, J. Baik, H. J. Shin, and S. C. Hong *Band-gap transition induced by interlayer van der Waals interaction in MoS₂* Phys. Rev. B 84, 045409 (2011) [↗](#)
- [157] M. Salmani-Jelodar, Tan Yaohua, G. Klimeck *Single layer MoS₂ band structure and transport* IEEE, Semiconductor Device Research Symposium (ISDRS), 2011 International [↗](#) 65
- [158] P. B. James and M. T. Lavik *The crystal structure of MoSe₂* Acta Cryst. (1963). 16, 1183 [↗](#) 97

BIBLIOGRAPHY

- [159] Aleksandra Vojvodic, Berit Hinnemann and Jens K. Nørskov *Magnetic edge states in MoS₂ characterized using density-functional theory* [↗](#)
- [160] Z. Y. Zhu, Y. C. Cheng, and U. Schwingenschlogl *Giant spin-orbit-induced spin splitting in two-dimensional transition-metal dichalcogenide semiconductors* *Phys. Rev. B* 84, 153402 (2011) [↗](#)
- [161] S. Lebègue and O. Eriksson *Electronic structure of two-dimensional crystals from ab initio theory* *Phys. Rev. B* 79, 115409 (2009) [↗](#)
- [162] M. Lovell, M. Khonsari, R. Marangoni *A finite element analysis of the frictional forces between a cylindrical bearing element and MoS₂ coated and uncoated surfaces*. *Wear* 1996, 194:60-70 [↗](#)
- [163] Yafei Li, Zhen Zhou, Shengbai Zhang and Zhongfang Chen *MoS₂ Nanoribbons: High Stability and Unusual Electronic and Magnetic Properties* *J. Am. Chem. Soc.* 130, 16739–16744 (2008) [↗](#)
- [164] Liangzhi Kou, Chun Tang, Yi Zhang, Thomas Heine, Changfeng Chen, and Thomas Frauenheim *Tuning Magnetism and Electronic Phase Transitions by Strain and Electric Field in Zigzag MoS₂ Nanoribbons* *J. Phys. Chem. Lett.* 3, 2934-2941 (2012) [↗](#)
- [165] Zhen Wang, Lin Ma, Weixiang Chen, Guochuang Huang, Dongyun Chen, Lanbang Wang and Jim Yang Lee *Facile synthesis of MoS₂/Graphene composites: effects of different cationic surfactants on microstructures and electrochemical properties of reversible lithium storage* [↗](#)
- [166] K. S. Novoselov, D. Jiang, F. Schedin, T. J. Booth, V. V. Khotkevich, S. V. Morozov, and A. K. Geim *Two-dimensional atomic crystals* *PNAS* [↗](#) vol. 102 no. 30 10451–10453 (2005) [↗](#)